CO EMISSION FROM THE INNER DISK AROUND INTERMEDIATE-MASS STARS

A Dissertation

Presented to the Faculty of the Graduate School

of Cornell University

in Partial Fulfillment of the Requirements for the Degree of

Doctor of Philosophy

by

Marc George Berthoud

January 2008

CO EMISSION FROM THE INNER DISK AROUND INTERMEDIATE-MASS STARS

Marc George Berthoud, Ph.D.

Cornell University 2008

To investigate the interaction between young stars and their circumstellar material we conducted a spectral survey of Herbig Ae/Be stars in the K-band. Non-photospheric Brγ emission is observed in the spectra from most stars, indicating a similar Brγ flux as the cooler intermediate mass T-Tauri stars. We find that the emission is probably caused by winds or by hot disk gas. To study different methods to estimate accretion luminosity we compared our Brγ fluxes with other accretion indicators. The mismatch between the estimated accretion luminosities suggests that using Brγ could overestimate the L_{acc} by several orders of magnitude.

We also observed CO overtone emission, but in a few objects only, perhaps because hot, dense gas is not common around these stars. We obtained high resolution spectra of the objects with observable CO overtone emission. These spectra allow us to establish constraints on the geometric distribution and physical characteristics of the emitting gas. We implemented a model of a hot gas disk to fit to our observations. Our results agree with previous conclusions, that 51 Oph is most likely a classical Be star, surrounded by a massive disk of hot gas. Our new findings include that the disk is probably seen at high inclination ($i > 83^o$) though a lower inclination ($i < 36^o$) is also possible. The vibrational excitation temperature of the gas is close to 3500K at the inner edge and falls off as expected from comparison to various disk models. The excitation temperature of the $v = 2 \rightarrow 0$ rotational bands is higher than for the vibrational transitions and indicates a source of energy

beyond radiative equilibrium in the inner regions of the disk. The quality of our data allows us to fit the emission line width. We find that on average, turbulence and geometrical broadening in the disk contribute ∼3km/s to the emission line width.

The other two stars from which we observed CO overtone emission are HD58647 and HD36917. HD58647 is probably a classical Be star like 51 Oph. Combining our high-resolution spectra with our model indicates that this star is surrounded by a disk of hot gas which is optically thin and not in radiative equilibrium with the radiation of the star. The star HD36917 is the only Herbig Ae/Be star for which we have observed CO overtone emission at high resolution. The emission appears to be caused by hot gas in a directed flow. We determined an upper limit for the mass flow rate of about $5 \times 10^{-6} M_{\odot}$/yr, which would be rather high for such a star.

BIOGRAPHICAL SKETCH

Born in Zürich, Switzerland, Marc Berthoud has been interested in science and technology since childhood. He has always enjoyed hands-on learning, especially related to computers or computer programming. He could often be found working for hours at a time in the computer lab of his high school, the Mathematisch-Naturwissenschaftliches Gymnasium Rämibühl, where he obtained his Matura degree in 1991.

After a mandatory Swiss government holiday with mud and guns, Marc continued his studies in physics at ETH Zürich. His diploma thesis on the mission planning for a micro-satellite was submitted in 1997.

Always being a world traveler, it is no surprise that Marc chose to continue his studies in 1998 at Cornell University, where he first joined the NEAR group to study the surface of the asteroid Eros. Later, he became a member of the FORCAST instrument team, working with Terry Herter. This instrument is being built for the SOFIA airborne telescope. As fate would have it, SOFIA has been delayed repeatedly, and science operations are now scheduled to begin in 2009; hence, none of the fun and interesting work on FORCAST is mentioned in this thesis.

For You

ACKNOWLEDGEMENTS

The work on this thesis would not have been completed without the invaluable assistance of many people. Not only were professional contacts important, but also relatives and friends who supported me during my time at Cornell. The following list includes many of them, but is by no means complete.

The most important guidance in conducting my research and writing this thesis was provided by my mentor and colleague, Luke Keller. My adviser, Terry Herter, gave me the fantastic opportunity to join the FORCAST team. His ideas, critiques, and seemingly infinite knowledge of astronomy have been crucial for setting the high standard that I've tried to achieve in this thesis.

Thanks goes to my family for their support and assistance, and for providing the occasional reason to escape Ithaca. Karen, in particular, patiently put up with me, and offered many hours of encouraging discussions and editorial advice.

The members of my committee, David Chernoff, Gordon Stacey, and Bryan Isacks, provided consistent support. Advice also came from other Cornell faculty members, especially Jim Bell and Ira Wasserman.

The friendship, solidarity, and exchange of ideas among fellow graduate students has been wonderful. I have been lucky to become good friends with some of them (you know who you are). The active student life at Cornell, has been an important factor in helping me to survive graduate school.

I have collaborated with scientists at Cornell and around the world: Important observations and research were done with David Whelan. His fresh outlook and enthusiasm will serve him well for his graduate studies at the University of Virginia. Discussions with Elise Furlan helped my understanding of young stars; she also acquired some of the data that I analyzed in this thesis. Matt Richter provided the data that originally started my research. I also had helpful discussions with

Wing-Fang Thi, Joan Najita, Claire Chandler, and Moshe Elitzur.

This work would not have been possible without assistance from the friendly, effective, and very competent scientific support and administrative personnel in the Space Sciences building. The staff at Palomar Observatory (where I took most of my data) is doing an excellent job supporting observers and maintaining their impressive facility. I was also assisted by the staff at Mauna Kea, especially at the Infrared Telescope Facility.

My research used data from the 2MASS survey operated by University of Massachusetts, the Simbad stellar database, and the ADS abstract service. Much of the Linux software I used was written by programmers who provide their code under free licenses. The work of the countless contributors to Wikipedia has been very useful to me.

This research was primarily supported by NASA through the SOFIA project.

I thank you all.

TABLE OF CONTENTS

LIST OF TABLES

LIST OF FIGURES

Chapter 1
Introduction

Since the 1960s, numerous young stellar objects (YSOs) have been identified and studied by astronomers. Such objects are stars in the process of formation or such that have formed within the last few million years. They are mostly associated with starforming regions and are commonly surrounded by material in the form of disks, shells, winds and/or jets. Only recently, however, with the improved observational capabilities at sub-millimeter and infrared wavelengths, have we been able to study the circumstellar gas around YSOs. We are now beginning to understand the processes of star and planet formation in detail; such studies are critical in order to investigate and understand the formation of our own solar system, will allow us to infer the history of extrasolar planets and ultimately help us to quantify the chance of finding life elsewhere in our galaxy. Here we present such an infrared study of the circumstellar material around such young stars.

1.1 Atomic and Molecular Emission

Spectroscopic studies of circumstellar material have identified emission lines from various atomic and molecular sources. The solar system abundance for the most common elements is given in Table 1.1. If all carbon is tied up in CO then we might expect an interstellar H/CO ratio of 3000; values between 1000 and 10^4 are used in the literature. Most of the remaining oxygen forms water, while a small amount of oxygen combines with silicon and other metals to form various types of

Table 1.1: Solar system element abundances, normalized to 1,000,000 for hydrogen (Cox, 2000).

H	He	C	O
1,000,000	98,000	360	850

mineral grains.

Hydrogen is the most abundant element. Neutral hydrogen atoms in a hot gas emit radiation from electron transitions in a series of lines called Lyman, Balmer, Paschen, Brackett, and other series, each named after its discoverer. Hydrogen molecules emit photons from electron transitions with an energy of several eV, that require pumping by FUV radiation. Such transitions are not expected in dense gas, since molecular hydrogen would dissociate at temperatures lower than required from these transitions. Hydrogen molecules can also emit in the infrared through mixed rotation-vibration (a.k.a. ro-vibrational) transitions. Such emission occurs in warm gas, since the first state is ~ 500K above ground (Brittain *et al.*, 2007). Such emission is about $10^{14}\times$ weaker than similar emission from CO, discussed below. A commonly observed example of a molecular hydrogen ro-vibrational transition is the 1-0 S(1) line at 2.12183μm.

While being much less abundant than hydrogen, **Carbon Monoxide (CO)** has numerous strong emission lines. The gas is ubiquitous in interstellar and circumstellar gas: it sublimates around 20K and dissociates at 4000K in dense gas (Najita *et al.*, 2007) (for lower density gas the dissociation temperature is higher, as collisions are less frequent). CO is observed in many astronomical environments and is often used as a proxy to measure gas mass. Various types of CO emission can be used to determine the temperature and other physical characteristics of the gas. *Overtone emission* arises from transitions where the vibrational energy decreases by two quantum states. Such emission is observed from hot (1000-5000K) gas at wavelengths around 2.3μm. This type of emission is strong in high density (above $10^{10}\,\mathrm{cm}^{-3}$) gas with molecules excited above 2000K. Emission caused by a energy decrease by one quantum level is called *fundamental emission*. This type of emission is mostly observed in colder (200-1000K) gas, and is observed at wavelengths

between 4.6 and 5.0μm. Fundamental emission is much stronger than overtone emission as its Einstein coefficients are larger by many orders of magnitude, due to the stronger electric dipole moment of the transitions. Although fundamental emission is more difficult to observe since it is in the M-band, numerous lines can usually be observed. ^{13}CO fundamental emission has also been observed. Finally, *Pure rotational* lines from CO are observed at millimeter and sub-millimeter wavelengths. These lines trace cool and cold gas. CO emission will be discussed in more detail in chapter 2.

Water and **Hydroxyl** emit in colder gas. OH has a similar spectral structure as CO, with fundamental emission lines around 3.6μm. Water is present between 150K (sublimation) and 2500K (dissociation) (Najita *et al.*, 2007). H_2O from hot sources can easily be observed from the ground, as it emits in lines not present in the cooler H_2O in our atmosphere. Colder H_2O can also be observed in high-resolution spectral observations if the Doppler shift relative to the Earth moves the lines away from atmospheric absorption lines.

Ionized Gas has numerous emission lines. Each atomic species emits at various wavelengths, depending on its excitation environment and ionization state. Such emission lines are observed mostly at higher energies, in the visible and ultraviolet. Electrons in the gas also emit *free-free* emission as they scatter off of the ions. Free-free emission is observed in the near- and mid-infrared, depending upon the mass and kinetic temperature of the gas.

Other molecules like CO_2, O_3, Polycyclic Aromatic Hydrocarbons (PAHs), and other organic molecules have rich spectra in the infrared, but are less abundant.

Solid particles of **Dust** emit a continuum spectrum with broad solid state features. Silicates have a characteristic spectral feature around 10μm. The shape of this and other features depends upon the physical properties and mineral compo-

sition of the dust.

1.2 Herbig Ae/Be Stars

Although all young stellar objects (YSOs) are fundamentally similar, a number of designations have evolved to describe these objects:

T-Tauri Stars (TTS) are YSOs with an effective surface temperature colder than 6400K (F5). For main sequence stars, this implies a stellar mass below $2M_{\odot}$ (Valenti *et al.*, 2003). Hundreds of such objects have been identified, mostly by their infrared excess. The IR excess is thought to be caused by warm circumstellar (CS) material, mostly in the disk. The inner edge of the disk is thought to be truncated at the co-rotation radius by stellar magnetic fields. Disk material is diverted and follows magnetic field lines to fall onto the star. Such streams are called *funnel flows*. The accretion shock from the impact onto the star heats the gas to 10^4K and beyond, causing visible and strong UV continuum emission. Continuum emission at all wavelengths fills in photospheric absorption lines, an effect called *veiling*. Finally, outflows from TTS are observed in various ultraviolet, visible and infrared emission lines, such as the MgII doublet at 2800Å.

TTS are divided into the *Classical TTS* (CTTS) that show Hα emission and are thought to be accreting, and the *Weak-line TTS (WTTS)* without Hα emission, where accretion has presumably stopped. A particular type of CTTS are *FU Ori Objects* discussed by Hartmann *et al.* (2004). Such stars exhibit luminosity outbursts, which can last between 10 and 100 years. During these outbursts, the star's brightness can increase by as much as a factor of 100. Current models explain this phenomenon as a sustained increase of accretion onto the star.

Warmer YSOs are called **Herbig Ae Be (HAeBe) Stars**. They are warmer than 6400K and show an infrared excess, just like TTS. We will discuss their

characteristics in the following paragraphs. *Intermediate Mass TTS (IMTTS)* are TTS with masses between 2 and $4M_{\odot}$. They range in spectral type from cold F-type to hot K-types. These stars will eventually evolve to become HAeBe stars. *Vega-Type Stars* are YSOs older than TTS and HAeBe stars and are surrounded by a disk of dusty debris. Such *debris disks* form after the initial gas and dust has been cleared from the system and consist of dust created by collisions between planetesimals. HAeBe stars eventually evolve into Vega-Type systems (Waters & Waelkens, 1998). The main difference between HAeBe stars and TTS is that higher-mass HAeBe stars are thought to evolve faster and reach the MS earlier than TTS. TTS also have strong surface magnetic fields, whereas such fields have only been observed from a few HAeBe stars (Wade *et al.*, 2007).

HAeBe stars are defined as B, A, or hot F-type YSOs. Although well defined from the evolutionary perspective, HAeBe stars are hard to identify observationally, since other star types have similar characteristics. Examples are Be stars with companions, classical Be stars, Wolf-Rayet stars, and AGB stars. Although the exact number of observable HAeBe stars depends on the selection criteria, more than one hundred HAeBe stars have been identified, many in star-forming regions (Vieira *et al.*, 2003). The stellar class was first identified and characterized by Herbig (1960). He studied stars of type A or hotter with emission lines (especially Hα). The stars are located in obscured regions, and illuminate reflection nebulae. The first criterion determines the mass range of the stars, and the other three criteria select for young stars. Malfait *et al.* (1998) surveyed HAeBe stars by selecting stars of B, A, and F-type with broad emission lines. All selected stars have an IR excess caused by CS dust. This allows HAeBe stars to be differentiated from classical Be stars that have IR excess from free-free emission. Some HAeBe stars selected by Malfait also have reflection nebulae and are located in star forming

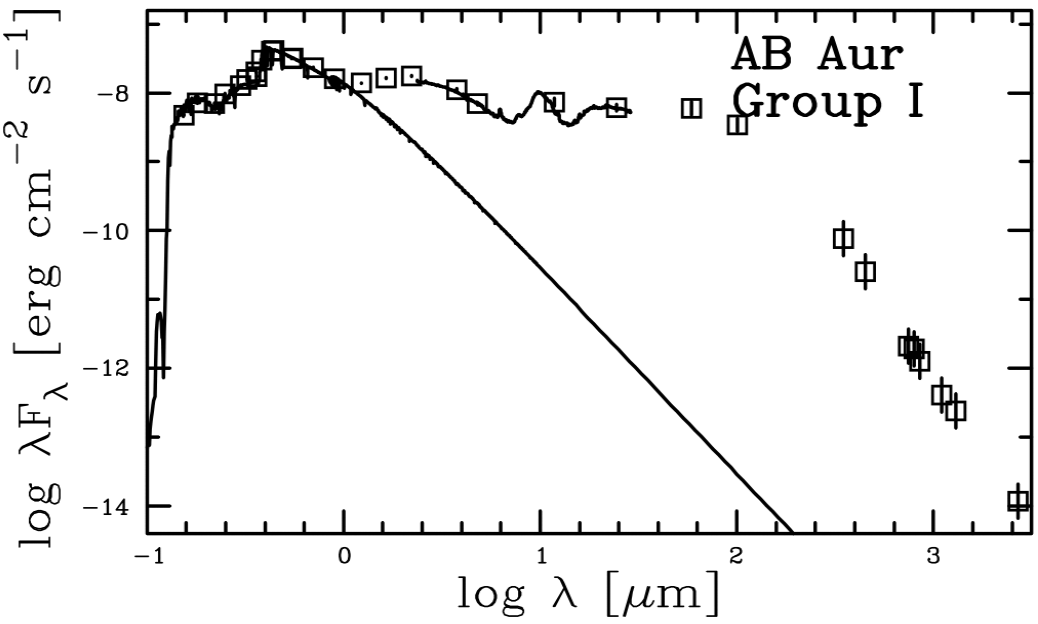

Figure 1.1: Full spectrum of the HAeBe star AB Aur. The plot is from Acke & van den Ancker (2004). The plot shows flux versus wavelength. Both axes are in log scale, the wavelength is μm. The squares are observed photometric data from the literature, the solid continuous line is the reddened Kurucz model for the stellar photosphere, the short line in the infrared shows the infrared spectrum from IS0.

regions. In their survey of HAeBe star Hα emission, the selection criteria of Vieira *et al.* (2003) included stars of type F5 or warmer with Hα emission, excluding giant stars, symbiotic stars, and luminous blue variable (LBV) stars.

The **spectral energy distribution** of the HAeBe star AB Aur is shown in Figure 1.1. At short wavelengths, the stellar spectrum dominates. At longer wavelength, the IR excess is visible in the photometric data and in the ISO spectrum. The IR excess is caused by circumstellar material most likely a disk (Malfait *et al.*, 1998; Meeus *et al.*, 2001; Acke & van den Ancker, 2004). The 10μm emission from silicate dust is visible at $\log(\lambda = 1.0)$.

In the following paragraphs we focus on existing knowledge of the CS material close to HAeBe stars:

The **disks** around most HAeBe stars are optically thick and have a vertical temperature gradient (Dullemond & Dominik, 2004). The disk contains between

10^{-5} and $10^{-1}M_{\odot}$ of dust and can be observed by its IR emission. Thermal emission from the hot dust (from 100 to 1400K the sublimation temperature for most minerals) provides most of the continuum emission. Solid state features are also seen in the near- and mid-IR. HAeBe stars warmer than B5 may not have disks since the disk dissipation times are comparable to the short pre-main-sequence lifetime for these stars.

The **dust** component of the **disk** has been investigated by a number of authors. Malfait *et al.* (1998) surveyed HAeBe stars to investigate the IR emission from CS dust. They analyzed infrared spectral energy distributions as shown in the boxes in Figure 1.1, fitting the dust disk model from Waters *et al.* (1988) to the observed spectra. The model assumes the dust is optically thin. Malfait *et al.* used the model to identify disks with single or double emission components and derived an evolutionary sequence for HAeBe disks: Initially, stars with proto-planetary disks have broad, single-peaked infrared excesses from a large continuous disk. Later, they develop composite excesses when gaps in the disk appear, probably due to the formation of large planets. The inner disk disappears before the outer disk, and the entire disk eventually becomes a debris disk (e.g. Vega, ϵ Eridani, Fomalhaut).

A later analysis of ISO spectra from the disks of 14 isolated HAeBe stars was performed by Meeus *et al.* (2001). The goal of the survey was to determine the mass and other physical properties of the CS dust. They analyzed ISO SWS spectra from 2 to 45μm and also used UV, optical, IR, and sub-millimeter photometry. Their sample included more evolved HAeBe stars with ages from 100kyr to 10Myr. All stars showed evidence of warm, dusty inner disks and large dust grains. Small dust grains are absent around some of the objects. Dust emission features from some of the stars indicate the presence of a hot, optically thin disk atmosphere. Some stars have a large mid-IR excess, indicating the presence of a heated, flared

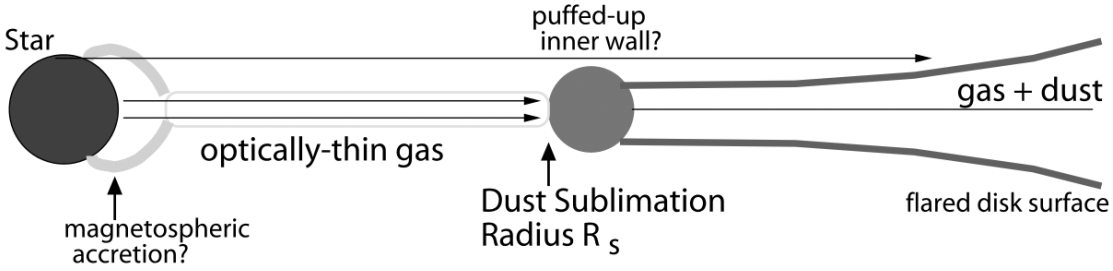

Figure 1.2: Schematic picture of the disk model used by Dullemond & Dominik (2004). The figure is from Monnier *et al.* (2005). Shown is a cross section of the inner disk region. To the left is the star with the optically thin inner disk. The disk becomes optically thick at the inner edge of the dust disk. In this picture the outer disk is flared, hence illuminated by the star.

outer disk, while other stars seem to have a self-shadowed outer disk. These disk characteristics are not correlated with stellar age. PAH band emission is observed from about 50% of the stars, all of which appear to have a flared outer disk.

The observations of Meeus *et al.* (2001) were discussed by Dullemond & Dominik (2004) using a dust radiative transfer model. Their two-dimensional model is shown in Figure 1.2 and includes an optically thin inner disk hole, a puffed-up inner disk rim, and a (possibly flared) outer disk. The model also includes the density and temperature distributions of dust throughout the disk. The presence of an optically thin inner disk hole causes the inner rim of the dusty disk to be far from the star, and to be puffed-up due to heating by direct starlight. The flaring of the outer disk is caused by a high disk mass to stellar mass ratio, a massive outer disk, or the presence of small grains in the disk. The model confirms that the mid-IR disk excess originates in the flared, illuminated outer disk. For flared disks, the z/R ratio in the disk increases from 0.1 at 1AU to 0.3 at 10AU. Dullemond and Dominik suggest an evolutionary sequence where the optical depth decreases as dust grains grow in the disk. This implies that flared disks are more likely to be found around younger stars.

Interferometric observations at 2.2μm by Eisner *et al.* (2004) confirm the pres-

ence of a large hole in the inner disk of HAeBe stars. They also find that the location of the inner edge of the dust disk depends only on the stellar luminosity, and is independent of other stellar parameters. However, for hot B-type stars ($L > 1000L_{\odot}$), the inner disk is optically thick, and the location of the inner edge of the dust disk does not follow the luminosity-dependent relationship. Further work by Monnier *et al.* (2005) and Vinković & Jurkić (2007) confirms that for HAeBe stars the location of the inner edge of the dust disk is proportional to $\sqrt{L_*}$, indicating that the dust rim is determined by the sublimation of dust particles in radiative equilibrium. They also confirm the existence of an optically thin inner disk for HAeBe stars and a thick accreting disk for stars with $L > 1000L_{\odot}$. Finally, they discuss how a dusty halo surrounding the star may contribute to the IR luminosity and the extinction of the star, especially for less massive TTS.

Emission from the outer disk was analyzed by Acke & van den Ancker (2004). They confirm the findings of Meeus *et al.* (2001) and Dullemond & Dominik (2004) by analyzing ISO spectra of 46 HAeBe stars. They find that the existence of PAH emission is usually correlated with the presence of a flared outer disk, but is not correlated with other disk properties. HST coronographic observations by Grady *et al.* (2005) confirm that as the outer disk is only visible in systems where PAH emissions are present. Medium resolution infrared spectra from the Spitzer Space Telescope obtained by Keller *et al.* (2007) disagree with these results. They observe PAH emission from systems with flared as well as self-shadowed outer disks and find that PAH emission intensity appears to correlate inversely with the scale height of the inner disk wall.

The **gas** within CS **disks** is difficult to observe, as the optical depth of the dust disk usually hides the emission lines from the CS gas. Gas emission from the inner disk regions of YSOs is discussed in detail by Najita *et al.* (2000) and Najita

et al. (2007). CO fundamental emission has been observed from most HAeBe stars. Usually the emission is broad and centrally-peaked, indicating that at least some of the gas is located at large distances from the star. Such emission has also been observed from gas located inside the dust sublimation radius, i.e. inside the dust disk. CO emission has also been observed at, or even inside, the co-rotation radius, indicating that the gas is likely involved in accretion and x-winds (accretion and wind flows originating at the inner disk edge Shu *et al.*, 1997). Observations and models of CO emission further from the star indicate that this emission can originate in the hot atmosphere of a colder, dusty disk. This atmosphere is about ten times warmer than the disk midplane, and may be heated by winds or by direct stellar UV or X-rays. The disk atmosphere seems to be composed of simple molecules and small dust grains.

Gas in the disk midplane is even more difficult to detect due to the large dust optical depth. However, such observations are important in order to understand accretion and planet formation. In the disk midplane, there is significant aggregation of dust and rich organic chemistry. It is possible that MagnetoRotational Instabilities (MRI) provide the viscosity necessary for accretion. Since this process requires ionized regions, observers and modelers are currently investigating the presence and size of such regions. CO fundamental emission has also been observed from gaps in CS disks. Recently Brittain *et al.* (2007) surveyed CO fundamental emission from 14 HAeBe stars. They find that all sources with an optically thick inner dust disk have CO emission. They also note a correlation between Brγ and CO fundamental emission.

Understanding **accretion** process is critical in order to understand the interaction between the disk and the star, as well as the evolution of the disk. Accretion presumably occurs when gas is picked up by the stellar magnetic field at the

co-rotation radius, and then falls onto the star along the magnetic field lines as funnel flows. Such accretion flows can be observed as redshifted emission from hot gas. Traditionally, accretion has been measured using the strength of Hα emission (Calvet *et al.*, 2004), but other photospheric lines are also related to accretion. Accretion shocks at the bottom of the funnel flows have been detected by spectral identification of the gas before and after the shock. Accretion luminosity is best measured using UV excess veiling of the stellar spectrum further discussed in chapter 3. The accretion rate $\dot{\mathrm{M}}$ can be determined using:

$$\mathrm{L_{acc}} = \mathrm{G}\frac{\mathrm{M_*}\,\dot{\mathrm{M}}}{\mathrm{r_*}} \tag{1.1}$$

where it is useful to use

$$\mathrm{G} = 3.15 \times 10^7 \frac{\mathrm{L_\odot R_\odot yr}}{\mathrm{M_\odot^2}}$$

Typical accretion values for TTS are $\dot{\mathrm{M}} = 10^{-8}\mathrm{M_\odot/yr}$. Accretion rates generally decrease with stellar age, but large variations are observed. $\mathrm{L_{acc}}$ was measured by Calvet *et al.* (2004) for 9 IMTTS. A study of UV spectra from HAeBe stars by Valenti *et al.* (2003) detected no measurable UV excess or veiling that would indicate accretion.

Winds are another important source of gas emission lines. They are caused by the interaction of the accretion flow with the star and the disk. Winds are observed as a blueshifted emission from CS gas, seen mostly as Hα absorption. Najita *et al.* (2000) found that the likely presence of winds correlates with the existence of accretion. (Wind models will be presented in Chapter 2.) Observations of HAeBe stars by Vieira *et al.* (2003) indicate that all such stars have Hα emission. They observe several types of line profiles, and discover that the profile type and the emission flux for a particular source can change on a timescale of months or weeks. A common indicator for winds are *P-Cygni* line profiles, which show a large blueshifted absorption component and a large redshifted emission component.

The absorption is presumably from infalling material, while the emission is from outflowing wind. Inverse P-Cygni line profiles are also observed and indicate infall of material along magnetic field lines similar to TTS. Some HAeBe stars have P-Cygni or inverse P-Cygni profiles. Imhoff (1994) observed that most HAeBe stars have P-Cygni line profiles in the MgII lines. Some HAeBe stars have an envelope, which is detected by absorption lines from cold gas like CO (Hartmann *et al.*, 2004).

1.3 Other A & B Stellar Types

There are several stellar types which can be misidentified as HAeBe stars:

Classical Be Stars are B-type main sequence stars with forbidden line emission. The line emission is likely caused by the reprocessing of stellar light by CS gas. They show evidence of CS material, mostly in the form of an infrared excess, probably caused by free-free emission from such material. These stars rotate quickly, but the rotation is not fast enough to cause decretion and account for the presence of the CS material. Therefore, other processes must be responsible for the presence of the CS material. The Be nature of these stars is transient; it is possible that normal B stars become Be stars. Reviews of these stars were written by Porter & Rivinius (2003) and Lamers (2006).

AGB Stars are older stars that have moved off of the MS, past the stage of He burning in the core. There are 2 phases of AGB burning: In *Early-AGB* stars, the main energy source is a He-burning shell around a C or O core. *Thermally-Pulsing-AGB* stars produce most of their energy in a H-burning shell, with occasional flashes of He-burning that can last between 10^4 and 10^5 years. A star may lose between 50 and 70% of its mass during the AGB phase. Due to the abundance of CS material, AGB stars have IR excesses. The geometry of this material is a

topic of ongoing research. This type of star has been reviewed by Olofsson (1999). Observations of AGB stars and HAeBe stars differ in the strength of the Balmer discontinuity and in the stellar luminosity.

1.4 Open Questions

The evolution of YSOs and their CS material is the topic of numerous ongoing studies. Although the properties of the dust are better known, since dust is easier to observe, there is much more to learn about the gas. This knowledge will be crucial in determining the lifetime and evolution of gas and dust disks, which is one vital step in order to fully understand disk accretion and star formation. Although the timescales in the dust disk are becoming clear, more research is needed to determine the same values for the gas component of the disks (Najita *et al.*, 2007). The characteristics of the gas are needed in order to determine the amount of accretion and the mechanism for accretion, as well as the conditions for planet formation, growth, and migration. Accretion in the disk requires viscosity in order to transfer mass and angular momentum, but the gas density in CS disks is too low to provide the necessary viscosity. One mechanism to enhance viscosity is turbulence, which could be measured by determining the intrinsic emission line width in the disk, or by studying the amount of vertical mixing in the disk (i.e. comparing the molecular abundances in the midplane with these in the atmosphere). Another process that causes viscosity is Magneto Rotational Instability operating in ionized regions. If MRIs are the dominant cause for disk viscosity, it is possible that large non-accreting regions of neutral gas may be observed in the disk. Finally, turbulence and therefore viscosity can also be driven by instabilities arising from the dust-gas interaction: Dust grains orbit the star on Keplerian orbits, while the gas orbits slower than Keplerian velocity, since it is partly supported by the pressure in the

disk.

CS disks are the birthplaces of planets, so it is important to determine the properties of the disks in order to constrain models of planet formation. The lifetime of the gas in the disk has direct implications for the formation of giant planets: If the lifetime is short, a fast process of planet formation is necessary, e.g. gravitational instabilities. If the gas lifetime is longer, a slower process such as core accretion is possible (Najita *et al.*, 2007). Other indicators can also be used to determine the mechanisms for planet formation (Matsuo *et al.*, 2007). For smaller (terrestrial) planets, the amount of gas affects the orbital eccentricity which is important for collisional growth of planetesimals. Once planets have formed, the migration of these planets is affected by turbulence and the amount of gas in the disk.

To investigate the interaction between the disk and the star, it is important to know the geometric structure and physical characteristics of the disk. For example, an accretion rate larger than a certain value will cause an optically thick inner disk without an inner disk hole (Garcia Lopez *et al.*, 2006). Also, it is important to investigate the relationship between the accretion rate and the rate of mass loss through winds and jets. High-resolution spectroscopy will provide the data necessary to determine which emission and absorption lines are caused by disk and/or wind material. CO overtone emission requires hot, dense gas. As such emission is not common among YSOs the precise mechanism that causes such conditions needs to be investigated.

1.5 Outline

The following chapter discusses the techniques used for observations and data reduction. We also present the model we use to fit the CO emission spectra.

Chapter 3 discusses the results of our medium resolution spectral survey of HAeBe stars. We concentrate on the results and implications for the Brγ fluxes. The next chapter presents the high resolution observations of CO overtone emission from the star 51 Oph. Our model fit to this high-quality data allows us to determine most relevant parameters for the gas disk. The last chapter discusses the high-resolution observations of the CO v = 2 $\rightarrow$ 0 bandheads of the stars HD36917 and HD58647.

Chapter 2
Techniques

2.1 Observing and Reducing Near IR Spectra

Two systems to identify stars common in the literature are HD number (from the Henry Draper Catalog) and SAO numbers (from the Smithsonian Astrophysics Observatory Catalog) are used in this thesis. We use HD numbers to identify the stars we study and we use SAO numbers for the calibrator stars. Throughout the work I will use hot (or warm) and cold to compare stellar spectral types instead of late and early.

2.1.1 Telescope Preparations and Procedures

The main challenge when observing in the Near-IR is atmospheric absorption, mostly by water vapor. Spectral windows in atmospheric transmission shown in figure 2.1 allow observations in certain bands. Due to the low spectral resolution (R=500) of the figure some narrow atmospheric absorption lines are not visible in the image. It is quite easy to observe in the J and H-band, but there are regions with large absorption in the K band. Due to deep atmospheric absorption lines the L and M-bands can only be observed in during very favorable conditions and/or at a very good site. As most absorption lines are caused by water, a dry atmosphere is critical for infrared observations.

Calibrator stars are observed to clean the spectrum of the sky absorption lines. The calibrator star does not necessarily need to be very close in position to the target star, although this is preferred. But the calibrator should always be observed at the same airmass and as close in time as possible. Important is that the calibrators are bright to minimize the necessary integration time to obtain the

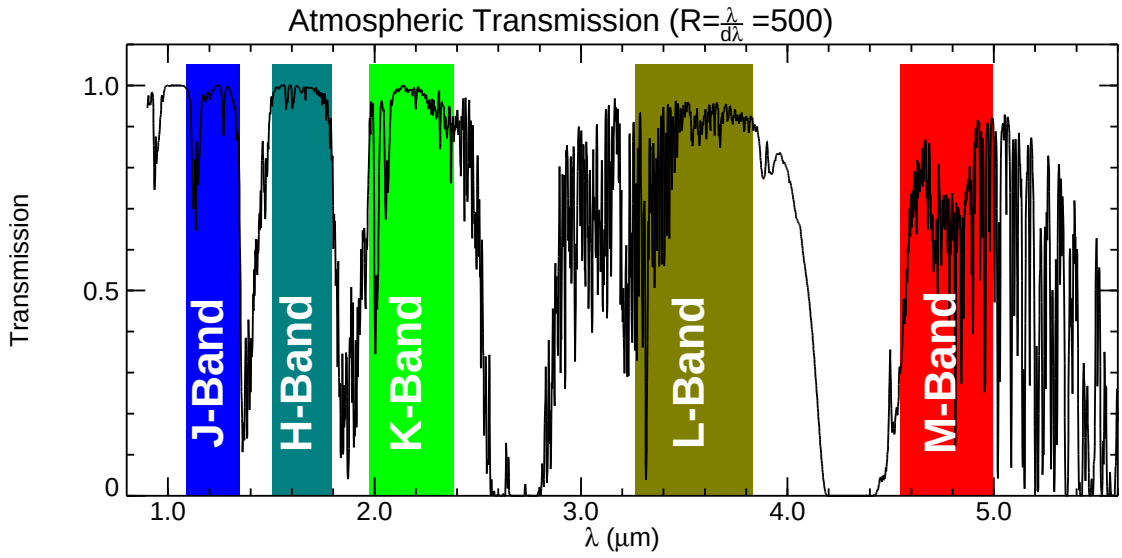

Figure 2.1: Near Infrared atmospheric transmission profile. The transmission is shown with 1.6mm of precipitable water vapor and an airmass of 1.5. The spectrum was produced with the ATRAN software (Lord, 1992) and was obtained from the Gemini telescope website. Shown are the atmospheric transmission bands as listed in Cox (2000). The spectrum is shown at a resolution of R=500.

necessary signal to noise ratio (S/N) on the calibrator.

For astronomical observations it is important to observe objects at least 30° above the horizon to reduce the effects of the atmosphere (45° is better). The amount of atmosphere between the star is measured as airmass, which is defined as

$$\text{airmass} = \frac{1}{\cos(\text{zenith angle})} \tag{2.1}$$

The observations should be planned that the observed objects are high above the horizon for the duration of the necessary integration time. To one hour after sunset should not be used for planning observations to allow time for setting up the telescope and give time for the thermal background to decrease.

A critical factor for any observations is the necessary integration time. It depends on the experiment requirement for the S/N of the reduced spectrum. To fit the model of the CO gas, our observations require S/N of a few hundred. The

integration time relates to the signal to noise ration by the following formula:

$$\frac{\mathrm{S}}{\mathrm{N}} = \frac{\mathrm{Sgt}}{\sqrt{\mathrm{Sgt} + \mathrm{n_p Bgt} + \mathrm{n_p Dt} + \mathrm{n_p r^2}}} \tag{2.2}$$

Using the values for our observations of 51 Oph with the NIRSPEC instrument, the parameters have the following values: g is the gain measured in electrons per ADU (analog to digital units, i.e. number of measured electrons per digital count), $\mathrm{g} = 4\mathrm{e}^-/\mathrm{ADU}$ for NIRSPEC. B is the background signal, Bt=65ADU in our case. $\mathrm{n_p}$ is the number of pixels used for the spectral extraction at one wavelength ($\mathrm{n_p} = 11$ in our case). The total integration time is t, which in case of NIRSPEC is 8 coadds 5 seconds each for a total of 40s. S is the signal count (of all $\mathrm{n_p}$ pixels) which we measured as 3200ADU. D is the dark current of the detector ($0.2\mathrm{e}^-/\mathrm{s/pix}$) and $\mathrm{r}^2 = 1250\mathrm{e}^-/\mathrm{pix}$ is the detector read noise. For the calculation we assume that the spectrum was extracted by summation of rows and find that S/N=710. This is more than the effectively measured S/N=250 in our spectra. The effective S/N is worse due to systematic variations (e.g. fringing) and uncertainties in the data reduction. Further the above calculation is valid for the brightest parts of the spectrum only. Some regions are considerably darker, due to atmospheric absorption, decreasing the measured S/N. Due to such differences, the results of earlier observations at a particular telescope are very useful to estimate the necessary integration time.

Despite the best planning the weather, instrument or software trouble can, and often do, affect the observations.

An **observing run** would proceed as follows. Knowledge of the instrument configuration and the source list from the proposal would be revised and updated before travel. We usually traveled one day in advance to familiarize ourselves with the observatory during the night before our first observing night and to change our

sleep schedule. The day before the run the observing sequence was planned, we familiarized ourselves with the telescope and instrument operations and we would set up folders and a quick reduction pipeline for the data. Most large telescopes are operated by specialized engineers (the telescope operator), the observer usually operates the instruments. Remote observing is useful at it saves travel time and is particularly recommended if the observer is already familiar with the telescope. It requires a reliable connection and special software designed to operate the instrument remotely. (An iChat or Skype connection with the telescope operator helps.)

During observations we would position the star in the slit and on the detector using the slit viewer, an optical element that allows the user to image the focal plane where the slit is placed. This check was necessary to avoid bad regions on the detectors. We observed the targets in turn at two telescope positions that differ by a small angle on the sky. This *nodding* procedure is used to subtract the sky and instrument background. We usually used an ABBA nod pattern, which means for one sequence one frame is taken in nod beam A and the next one in nod beam B. The first frame for the next sequence is in nod beam B, followed by a frame in nod beam A. These sequences are repeated as long as necessary to obtain the necessary integration time. As described above, we would observe calibrator stars with known spectra to measure sky absorption. The necessary integration times were determined by applying the formula above. Flatfield, dark current and wavelength calibration frames to measure detector performance and for wavelength calibration were taken at the beginning of each observing night. For the observations at the IRTF telescope we took flatfield frames of the dome, for the Palomar observations we took flatfield frames from the sky.

2.1.2 Reduction of Spectra

The different steps necessary for spectral extraction are illustrated in Figure 2.2. Examples for the **observed image** are given at the top of the figure. The images shown were acquired using SPEX instrument on IRTF. The target star for this observation is SAO 171317. For illustration purposes, only a subset of the 1024 × 1024 detector image is shown. The wavelength range is about 2.18μm to 2.43μm (left to right). In these images the dispersion direction is horizontal while the vertical direction follows the image of the slit on the sky. The following process produces these images: The light from the star is absorbed by the atmosphere. This absorption is wavelength dependent as absorption lines from water and other molecules are primarily responsible for this absorption. Such absorption lines are visible as darker lines across the spectral trace in the "Chop A" image. The spectrograph disperses the incoming star light using diffraction gratings, prisms or a combination of the two. The instrument can also add its own interference pattern to the spectrum (fringing). This effect is caused by pairs of almost parallel transmitting optical surfaces acting like a Fabry-Pérot interferometer. The spectral response of the spectrograph will determine the instrument resolution and depends directly on the slit width. The detector will add variations in the image because of differences between individual pixels. Bad pixels will generate random signals throughout the image. Line and continuum background are added to the image from the sky (such sky emission lines are visible in the right image), from the telescope and the instrument and from the detector.

The following discussion roughly applies to all programs for reducing spectral data. To obtain the spectrum the following **extraction steps** are performed (see Figure 2.2):

- **Bad pixel Removal:** For some images we used the sigma filter software

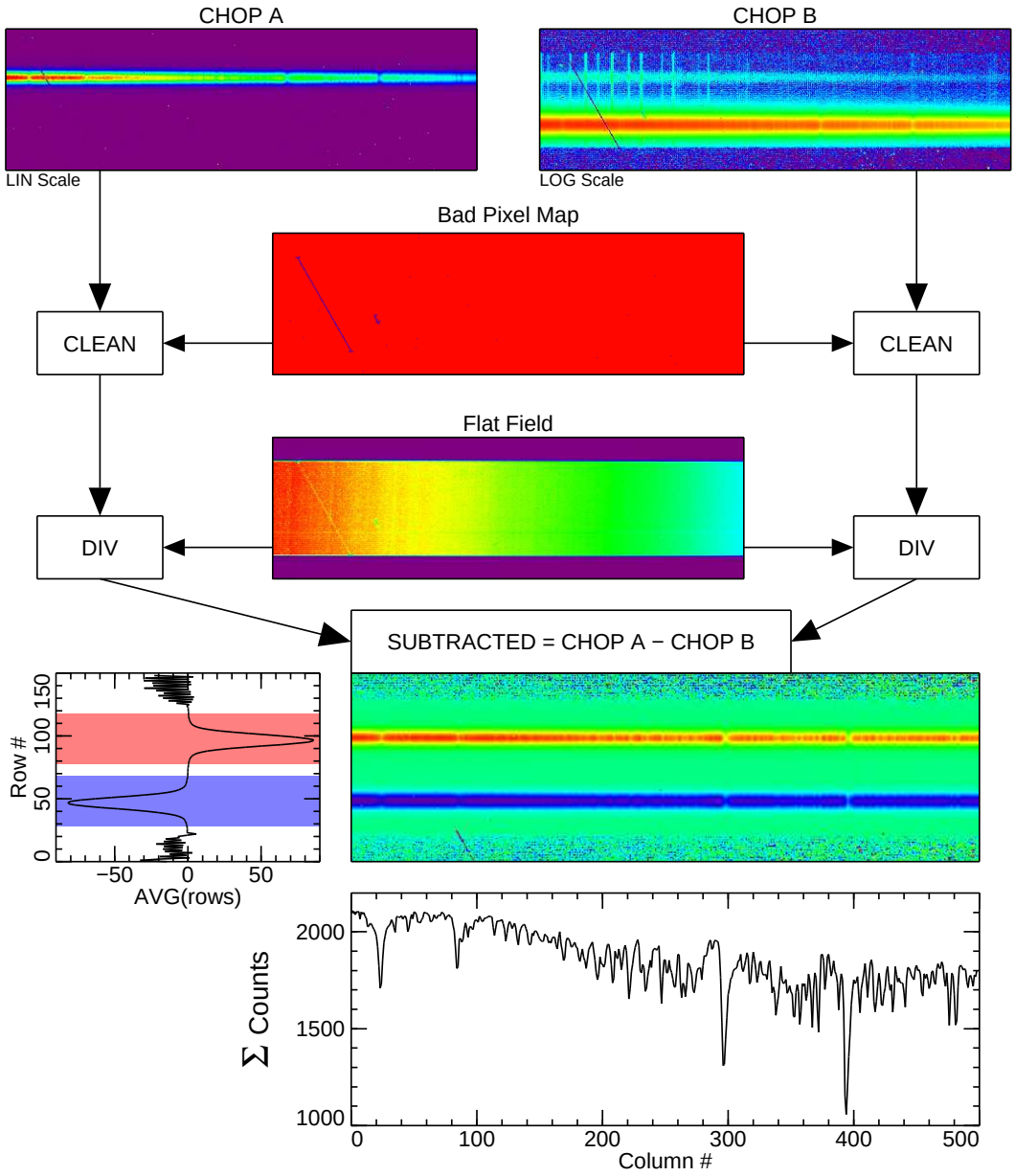

Figure 2.2: Reduction of the low-resolution spectra: The top two images show the raw data from the two chop positions. High values are red, low values purple. To illustrate weak features the right image was scaled logarithmically. The image below shows the bad pixel map, with bad pixels in purple. The other image needed to reduce the data is the flat field shown below. The lowest image shows the subtraction of the two cleaned and flat-fielded chop frames. The plot to the left shows the average spatial profile of the spectrum. The bottom plot shows the extracted spectrum.

written by Joseph Harrington to clean the images of bad pixels. This software estimates the flux value for bad pixels by interpolating over adjacent ones. It requires a map of bad pixels for the detector. A somewhat reliable way of obtaining such maps is by identifying pixels with values that always vary a lot from adjacent pixels. Similar processes were used for the other images.

- **Flat Field Correction:** To correct for the non-uniform response between individual detector pixels the image is divided by the FlatField. This frame is obtained by taking several frames while illuminating the instrument with a white light source. These frames are cleaned for bad pixels and median combined. In Figure 2.2, the height of the illuminated part of the flat field indicates the length of the slit.

- **Nod Subtraction:** The cleaned and flat fielded frames from each nod are subtracted. The subtracted frame in the figure clearly shows the positive (red) nod A trace, the negative (blue) nod B trace and the zero (green) background. The noisy bands on the top and bottom are instrument noise amplified by division by the very small flat field signal beyond the end of the slit. This step cancels the sky and emission continuum and lines. It also removes emission from the instrument and the dark signal from the detector. At our wavelengths, the background emission can vary quickly, such that fast nodding is necessary for ensure uniform background removal.

- **Spatial Rectification:** Due to instrument design constraints, the spectral and spatial direction are tilted relative to the image rows and columns for some instruments. Such images need to be spatially rectified. This is usually the case for cross dispersed spectra, but, as confirmed by visual inspection, is negligible for our single order data.

- **Spectral Extraction:** To extract the spectrum we used the Optimal Ex-

traction algorithm as described by Horne (1986). This algorithm first creates a spectral profile by averaging the rows of the spectrum. This spectral profile is shown in Figure 2.2 on the left of the subtracted frame. The profile is used to select the spectral region to extract (blue & red shaded regions). The profile (or a function that fits it) is then fitted to the columns of the subtracted frame to determine the spectrum, shown below the difference frame. This procedure also removes residual background emission. For high signal to noise data it is simpler to extract the spectrum by adding the pixel values for each row (this is how the spectrum shown in the figure was obtained). The extracted spectrum is shown below the subtracted images. The sky absorption lines in the spectrum are clearly visible along the traces in the subtracted frame.

- **Coadding:** After extraction the spectra from the different nod cycles are coadded. This is done by adding all spectra. If signal to noise or integration time differ for different sets of data, the spectra should be weighted appropriately.

- **Telluric Correction:** An important contribution to the observed spectrum is the wavelength dependent absorption by the atmosphere. Figure 2.3 illustrates the process to correct this effect. Both the source and the calibrator spectrum are extracted as described above. The large sky absorption features around 2.06μm are clearly visible in the spectra as well as the decline in instrument response towards shorter wavelength. To obtain the sky absorption spectrum the calibrator spectrum is divided by a model of the spectrum of the calibrator star. For our purposes the spectrum of a blackbody with the calibrator star's effective temperature is an adequate model. We alternatively used the models by Kurucz (1992) to determine sky subtraction but

there was no large difference. The source spectrum is then divided by the sky absorption spectrum to compute the reduced spectrum of the source. For some sources we used the XTellCor package (Vacca *et al.*, 2003) that uses a similar procedure but requires an A0 type calibrator star.

- **Wavelength Calibration:** The spectrum is then wavelength calibrated using reduced spectra of lamp lines or using sky emission or absorption lines with known wavelengths. We used lamp lines for the calibration of the SPEX data and sky lines to calibrate the PHARO spectra.
- **Flux Calibration:** To flux calibrate the spectra we adjusted the spectra to match the integral of the spectrum over the K-band window to the published K-band magnitude values from the 2-MASS survey (Skrutskie *et al.*, 2006).

2.2 CO Emission Disk Model

The presence of CO as the main tracer of molecular gas in a circumstellar environment presents the potential ability to determine a number of parameters of the emitting region: temperature, density, optical depth, location, velocity etc. But to be able to do this we require the ability to model the emission in detail. The inherent richness of information complicates the analysis, since this also makes parameter space large. However as we shall see, high S/N, high spectral resolution measurements coupled with modeling does enable the determination of (or in some cases to constrain the) many physical parameters of the disk.

In this section we outline and develop the model we have constructed for the CO emission. We emphasize the mathematical and numerical approach and procedures, whereas the modeling of the data and the scientific interpretation will be discussed in the following chapters.

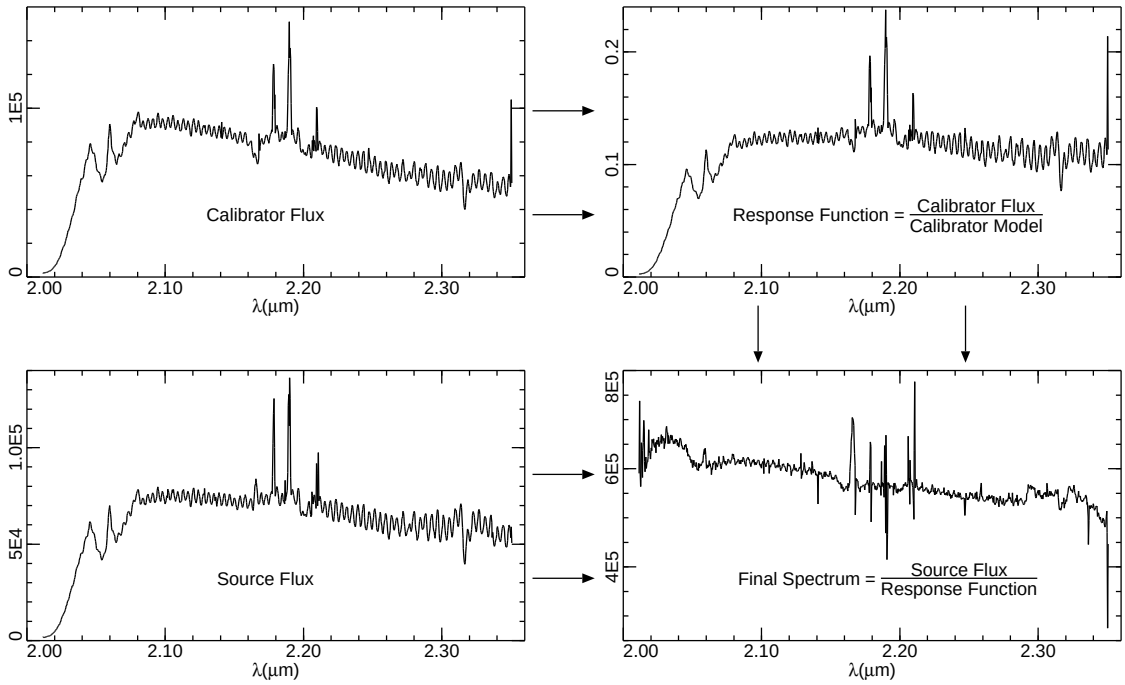

Figure 2.3: Correction of sky and instrument effects using the calibrator: The top left image shows the extracted spectrum of the A0 class V star SAO133645. This spectrum is divided by a model spectrum of the calibrator to obtain the spectral response function of the sky and instrument (top right). The extracted spectrum of our program star HD36917 (bottom left) is divided by the response function to obtain the final reduced spectrum (bottom right). All fluxes are in arbitrary units.

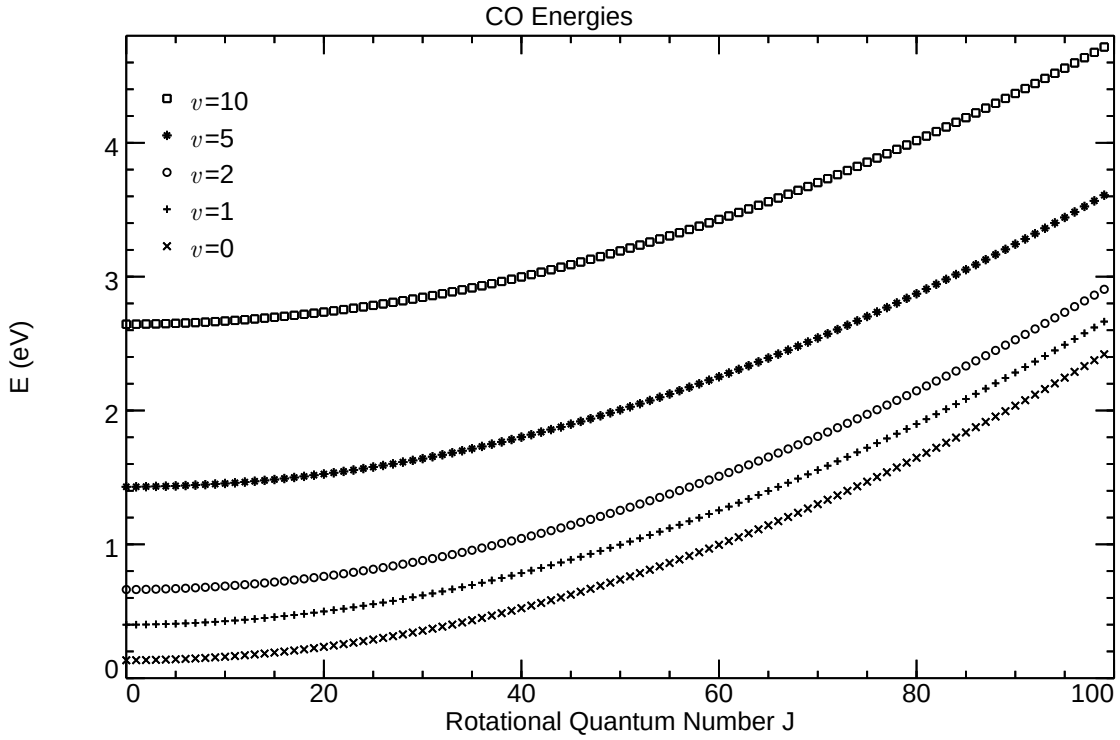

Figure 2.4: Ro-vibrational Energy levels of the CO molecule. For each vibrational level (v=0, 1, 2, 5, 10) the energies for the rotational levels J=0..100 are shown. The energies were calculated using Dunham's formula (see text).

2.2.1 CO Overtone Emission

The transitions we observe are due to the coupling of vibrational states (quantum number $\boldsymbol{v}$) and rotational states (quantum number $\mathbf{J}$) of the CO molecule. A diagram of the energy levels in the CO molecule is shown in Figure 2.4. The figure shows how the energy levels are roughly $\propto v$ and $\propto \mathrm{J}^2$. In particular, we look at *overtone* emission (i.e. $\Delta v = 2$ and $\Delta \mathrm{J} = \pm 1$). For the P-branch ($\Delta \mathrm{J} = 1$) the transition energies decrease with increasing J. For the transitions of the R-branch ($\Delta \mathrm{J} = -1$), the energies of the lines first increase with increasing J. The energies reach a maximum around $\mathrm{J} \sim 50$ (for $\Delta v = 2$), then decrease for higher values of J. The lines with the highest energies combine to form a strong emission *bandhead*. This effect can be explained as follows: The transition energies can be understood

as the sum of the contribution from the change in J (ΔJ $= -1$) and the change in v ($\Delta v = -2$). The contribution from ΔJ $= -1$ increases with increasing J, while the larger contribution from $\Delta v = -2$ decreases with increasing J. The increase of the first contribution is larger than the decrease of the second contribution for J < 50, causing an maximum in the transition energy at J ~ 50. Such bandheads also occur for *fundamental* ($\Delta v = 1$ transitions but are not observed as the bandhead happens around J ~ 90) level which are only populated at temperatures higher than the dissociation temperature of CO.

2.2.2 CO Emission Model

We model the CO rotational-vibrational emission as described in Kraus *et al.* (2000). We briefly summarize the methods here. To calculate the molecular **energy levels**, we use the Dunham coefficients $\mathrm{Y_{k,l}}$ of Farrenq *et al.* (1991) with the equation suggested by Dunham (1932):

$$\mathrm{E}(v, \mathrm{J}) = \mathrm{hc} \sum_{\mathrm{k,l}} \mathrm{Y_{k,l}} \left(v + \frac{1}{2}\right)^{\mathrm{k}} \left(\mathrm{J}^2 + \mathrm{J}\right)^{\mathrm{l}} \tag{2.3}$$

As defined above, v and J are the vibrational and rotational quantum numbers. For this simple model, we assume that the gas is in LTE, hence all quoted temperatures are *excitation temperatures*.

We calculate the **level populations** $\mathrm{n}_{v\mathrm{J}}$ according to the Boltzmann distribution

$$\mathrm{n}_{v\mathrm{J}} = \frac{\mathrm{n}}{\mathrm{Z}}(2\mathrm{J}+1)\mathrm{e}^{-\frac{\mathrm{E}(v,\mathrm{J})}{\mathrm{kT}}} \tag{2.4}$$

with n being the particle volume density. The partition function Z was calculated numerically by summation up to $v = 15$ and J $= 110$. The states with larger quantum numbers contribute little to the partition function because of their large energies (thus low level populations - see Figure 2.4). To determine the **absorption**

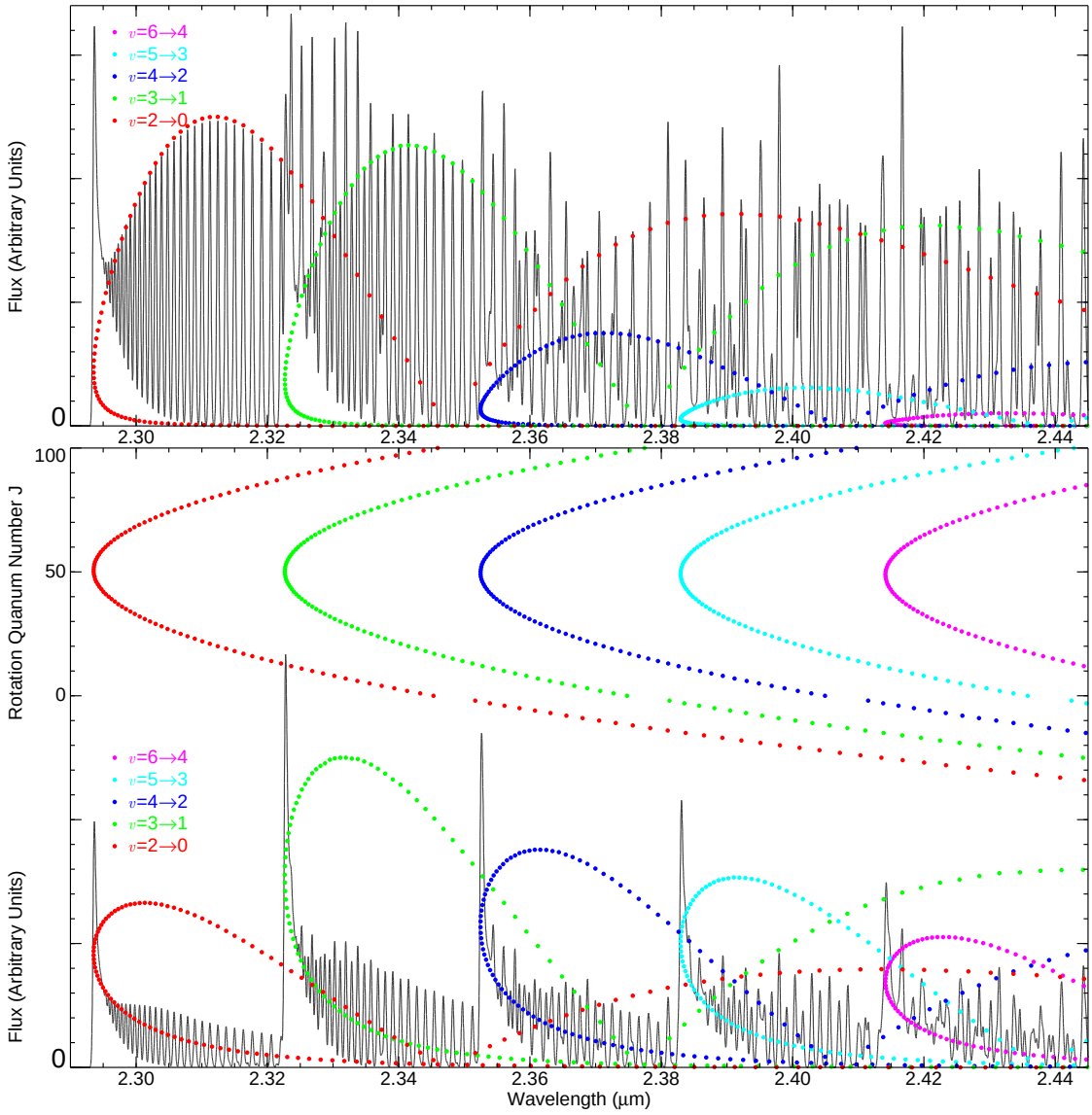

Figure 2.5: Illustration of the formation of CO spectra. The top part of the bottom plot indicates the wavelengths of the overtone transitions for the P-branch (negative rotational quantum numbers J) and the R-branch (positive rotational quantum numbers J). The different colors indicate the different vibrational transitions. The black line indicates the optical depth for optically thin CO gas with an emission line width ($V_{g,emm}$) of 30 km/s. The dots plotted with the optical depth indicate the strengths of the individual transitions. The top plot indicates the transition strengths and optical depth for an excitation temperature of 2000K, the bottom plot for 4000K.

coefficient K_ν, we used the Einstein coefficients $A_{vJv'J'}$ of Chandra *et al.* (1996) in conjunction with the relation between the Einstein A and B coefficients, which gives

$$K_\nu = \frac{c^2 n_{vJ} A_{vJv'J'}}{8\pi\nu^2} \left(\frac{2J+1}{2J'+1} \cdot \frac{n_{v'J'}}{n_{vJ}} - 1 \right) \Phi(\nu) \tag{2.5}$$

The indexes v and J are for the upper energy level, while, v' and J$'$ are for the lower energy level. $\Phi(\nu)$ is the line profile function. The Einstein A coefficients decrease with increasing v and increase slowly with increasing J. Hence the line intensity depends mostly on the level populations.

The formation of the spectra in illustrated in Figure 2.5. The pileup of lines in the R-branches at J=50 can be seen to form the bandheads. As the A coefficients don't vary much, the differences in line strength are mostly due to the level populations, which are determined by the excitation temperatures. The plots shows how for colder gas the low vibrational and low rotational levels ($v = 2, 3$ and J ~ 20 levels) are more important whereas for warmer temperatures vibrational levels up to $v = 4$ and levels around J ~ 40 contribute more to the spectrum. It is important to note how the relative strength of the bandhead increases with rising temperature.

The plots can also help us to understand why no bandheads are usually seen in absorption by cold CO gas. In that case only low J rotational levels are excited and radiation at the wavelength of the bandhead will not get absorbed due to the lack of molecules with high rotational excitation. The detection of bandheads in absorption or emission is a clear sign for the presence of hot gas (at least $\sim$ 1000K).

The use of LTE applies to the rotational levels within each vibrational level. A density between 10^6 and $10^8\,\mathrm{cm}^{-3}$ is necessary for these levels to thermalize (Scoville *et al.*, 1980; Thi *et al.*, 2005). Therefore our observations of the $v = 2 \rightarrow 0$ bandhead are accurate and not affected by assuming LTE. Vibrational levels however are only thermalized at gas densities above $10^{10}\mathrm{cm}^{-3}$ (Scoville *et al.*, 1980).

The equilibrium is established through collisions with HI, which has a much larger collision cross section with CO than H_2. In optically thick gas (i.e. when radiative transitions dominate) the vibrational levels are not thermalized (Scoville *et al.*, 1980; Najita *et al.*, 1996b). Otherwise (for optically thin gas) a common excitation temperature is appropriate to describe the excitation of the vibrational levels. Najita *et al.* (1996b) found that non-LTE effects are more important in the colder, outer regions of circumstellar structures. As most of the emission we observe originates in the hotter, inner regions, our assumption of LTE is adequate for our observations.

We use a Gaussian **line profile function** $\Phi(\nu)$ with width $V_{g,emm}$ for the emission line profile. In the previous CO overtone models we reviewed, this width has been "preset" by the modeler. We believe that our data are of sufficient quality to allow us to fit this width for the first time.

The **intensities** on the disk surface were calculated using

$$I_\nu = B_\nu(T)\left(1 - e^{-\tau_\nu}\right) \tag{2.6}$$

with the optical depth τ_ν being

$$\tau_\nu = N \sum_{lines} \frac{K_\nu}{n} \tag{2.7}$$

where N is the column density and n the density of CO and K_ν the absorption coefficient.

When estimating the temperature of the gas by measuring the bandhead it is important to consider the optical depth. The effect of high optical depth is shown in Figure 2.6. For optically thin gas the bandhead is clearly stronger than the lines with lower J values. However, as the optical depth increases these lines increase in strength relative to the bandhead. As our formulas show the optical depth depends not only on the column density N_{col} but also on the emission line width $V_{g,emm}$.

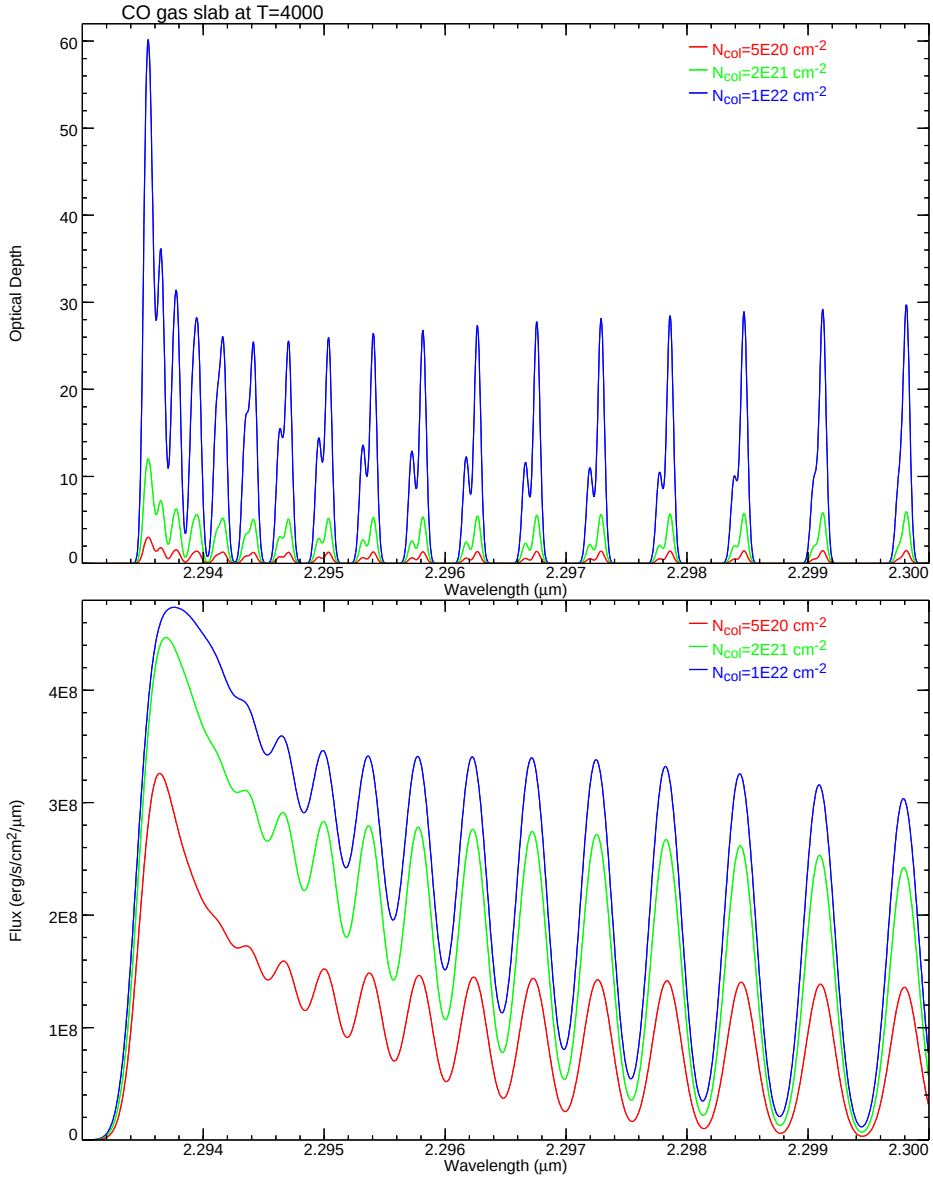

Figure 2.6: Effect of large optical depth on the CO spectrum. The plots show the bandhead of the $v = 2 \rightarrow 0$ transitions for an excitation temperature of 4000K. The plots show a column density of 5×10^{20}, 2×10^{21} and $1 \times 10^{22} \frac{1}{\mathrm{cm}^2}$. The top plot indicates the optical depth, while the bottom plot shows the final spectra as observed through a low resolution spectrometer.

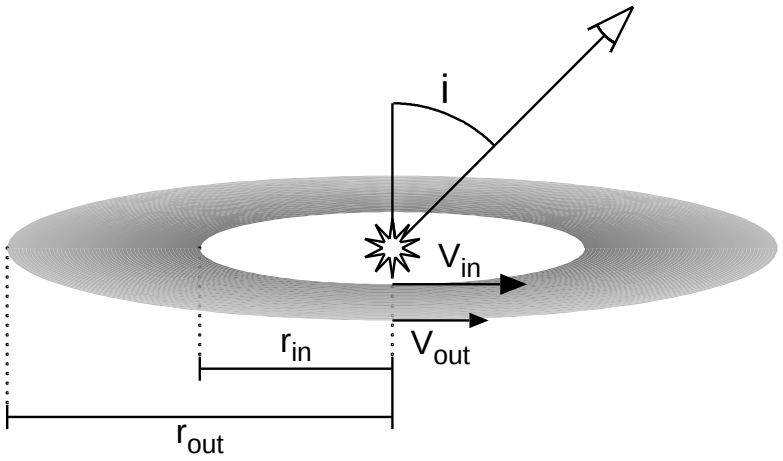

Figure 2.7: Schematic of the disk model: The Keplerian disk is geometrically flat with the column density and the temperature changing with radius. The inclination angle (i) is measured between the disk normal and the line of sight.

To test different CO distributions, we model **various gas geometries**, including a narrow gas ring rotating around the star at a fixed speed, as well as an extended disk with the gas rotating in Keplerian orbits. A schematic of our **disk** model is shown in Figure 2.7. For this disk, we use a power law temperature distribution for the excitation temperature of the CO gas as a function of radius in the disk:

$$\mathrm{T(r)} = \mathrm{T_i} \left(\frac{\mathrm{r}}{\mathrm{r_i}} \right)^{-\beta} \tag{2.8}$$

where $\mathrm{T_i}$ is the temperature at the inner edge of the disk ($\mathrm{r_i}$) and β is the power law index. Thi *et al.* (2005) have chosen $\beta = 3/4$, which is the theoretical value for a flat disk irradiated by the star or a disk accreting with constant viscosity (Hartmann, 2001).

In a similar way, we use a power law to describe the variation in column density across the disk

$$\mathrm{N(r)} = \mathrm{N_i} \left(\frac{\mathrm{r}}{\mathrm{r_i}} \right)^{-\gamma} \tag{2.9}$$

We further fit $\mathrm{V_{p,i}} = \mathrm{V_{Kepler,i}} \sin \mathrm{i}$ for the projected Keplerian velocity (at the inner edge of the disk) and the ratio of outer to inner radius $\mathrm{r_o/r_i}$. We do not fit

the inner and outer radius individually since these cannot be determined without knowing the inclination angle i. To match the observed flux, we fit the solid angle under which we see the disk:

$$\Omega = \frac{(\cos \mathrm{i})\, \pi\, \mathrm{r_i^2}\, [(\mathrm{r_o}/\mathrm{r_i})^2 - 1]}{\mathrm{d}^2} \tag{2.10}$$

Here, i is the inclination, $\mathrm{r_i}$ is the inner disk radius and d is the distance to the star. We assume that the height of the disk is geometrically thin.

We also fit models with a **narrow gas ring**, in which case we only have one temperature T, one column density n, the solid angle Ω and the maximum radial velocity $\mathrm{V_p} = \mathrm{V_{Kepler}} \sin \mathrm{i}$. The spectrum of such a ring is shown in Figure 2.8. Both ring and disk model assume that the optical column is vertically thin and that the gas properties don't vary along this column.

The variables Ω, N(r), T(r) and $\mathrm{V_{g,emm}}$ are linked in the following ways: For optically thin emission, the incoming flux is conserved if Ω increases and N(r) decreases. For larger column densities, the fitting of the temperature is affected by the optical depth. The optical depth of individual CO emission lines is large if the column density N(r) is large, or if the lines are narrow, *i.e.* $\mathrm{V_{g,emm}}$ is small. A large column density will affect the lines at the bandhead more than the lines at longer wavelengths. For optically thin gas, a stronger bandhead indicates higher temperature. As the optical depth increases, the strength of the bandhead emission decreases relative to the other lines, requiring a higher temperature to fit the same spectrum (see Figure 2.6).

We also fit an **expanding sphere** or **conic double shell** of gas. The goal of this model is to fit spectra with a convex ridge between the bandhead shoulder and the peak. Such models have been used by others to fit similar spectra: A simple model with two clouds of gas each with a large Gaussian velocity distribution was

used by Kraus *et al.* (2000). Chandler *et al.* (1995) used a more detailed wind model that included changes simulations of the wind density, temperature and radial velocity. Najita *et al.* (1996b) found that high wind densities are required for CO overtone emission and suggest that winds are more likely to display asymmetric emission profiles as the receding gas may be hidden by the disk. Our wind model simulates an expanding shell or double cone of optically thin, hot CO gas. We fit the total number of molecules (actually the shell projected solid angle Ω times the preset column density N_{col}). We also fit the emission line width $V_{g,emm}$, the temperature and the velocity V_o of the spherically symmetric outflow. In the case of conic double shell we also fit the inclination i of the conic axis towards the observer and the opening angle θ of the cone.

The last model we fit, is an optically **thick slab** of gas which is **rotating** around an axis perpendicular to the line of sight and **expanding** in the line of sight direction. This model is used to test the effect of an expanding gas column on the emission line width $V_{g,emm}$. Apart from the gas temperature we fit the column density N_{col} at the center of the slab. The density of the gas inside the optical column decreases towards and away from the observer according to a Gaussian profile with width V_{col}. The width of the slab parallel to the axis of rotation decreases with distance from the cloud center according to a Gaussian profile with velocity width V_{diff}. We also fit the projected solid angle Ω of the slab.

To calculate the amount of emitting gas in all our models one has to multiply the column density N_{col} with the surface area calculated from the solid angle of the structure ($A = \Omega\, d^2$) where d is the distance to the object.

The effect of these geometries on the spectrum is shown in Figure 2.8. The top plot (a) shows the bandhead and the emission from the lines with $J < 50$ on the long wavelength side. As they approach the bandhead the lines merge

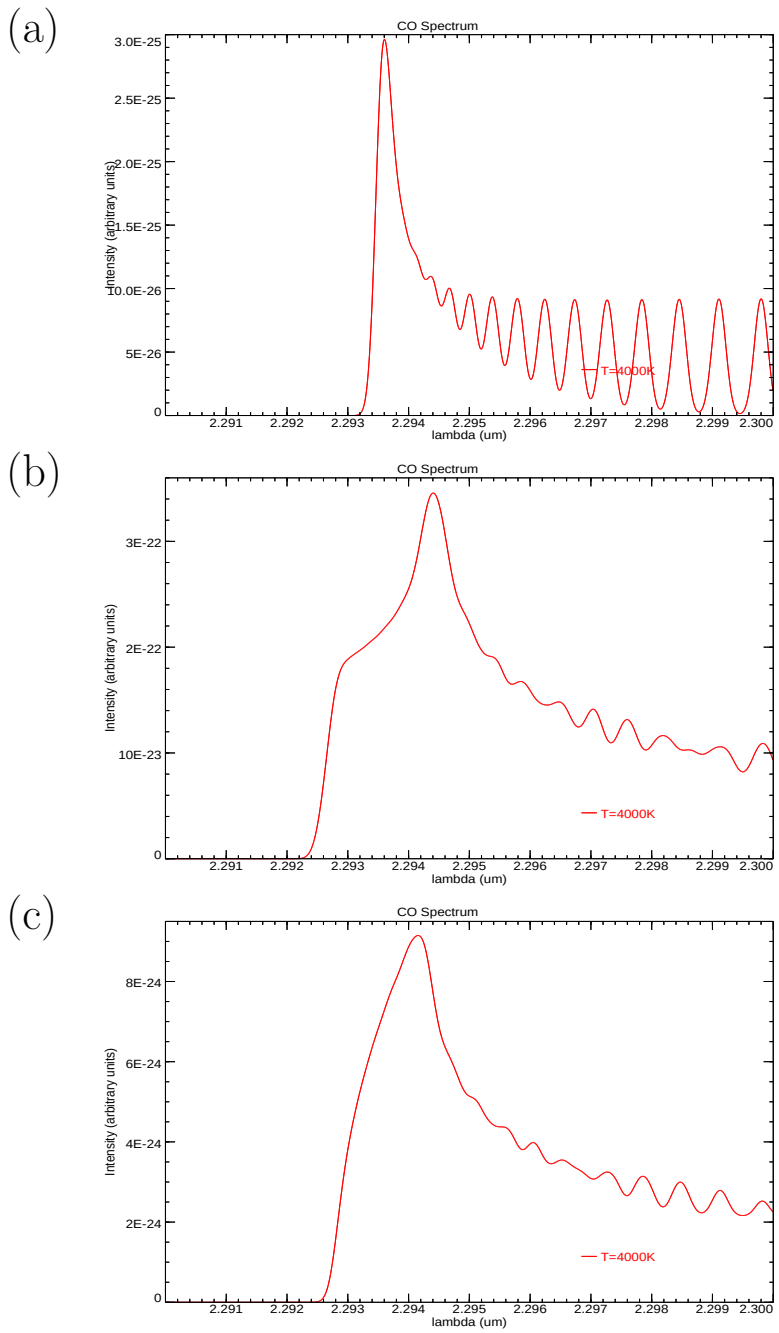

Figure 2.8: Spectra of the CO $v = 2 \rightarrow 0$ bandhead with different gas geometries. All spectra show optically thin emission at a temperature of 4000K. The top spectrum is for a non-moving cloud of gas (a). The next spectrum is for a rotating disk or ring (b) and the bottom spectrum shows the emission from a rotating, an infalling or an expanding shell (c). These three geometries all create the same spectrum.

because the distance between the lines decreases. The spectrum of a disk or a ring in Figure 2.8(b) forms an M-shaped emission line profile . This line shape causes the bandhead to split into a shoulder and a peak connected by a concave ridge. The shoulder is caused by the short wavelength point, the peak by the long wavelength one. The distance between the shoulder and the peak is determined by the maximal difference in line of sight velocity of the gas. The two maxima in the line profile cause an interference-like beating effect in the individual rotational lines longward of the bandhead. In Figure 2.8(b) destructive interference is seen at 2.2960 and 2.2987μm and constructive interference at 2.2975μm. The location of these features depends on the maximal difference in the line of sight velocity of the gas. The emission from a shell causes a rectangular emission line profile. This causes a shoulder shortward of the main peak of the bandhead and again a beating pattern for the individual rotational lines longward of the bandhead in Figure 2.8(c). However in this case the ridge between the shoulder and the peak of the bandhead is convex. The precise shape of all these spectra is also affected by optical depth.

It is necessary to fit a Doppler velocity offset to account for the star's radial velocity. This offset is constant and does not affect the physics of the model. We also fit a wavelength independent flux offset since our background models are not always reliable. As the flux offsets are small compared to the signal, we do not fit a continuum slope. Varying these additional parameters significantly improved the quality of the fit.

The final model spectrum is convolved with the spectral response of the instrument used. For NIRSPEC we used a Gaussian profile with a width of 5.0 km/s, consistent with measured FWHM of lamp lines in our calibration spectra.

We checked the results from our model by comparing shape and flux of our

spectra to the figures published by Najita *et al.* (1996b); Thi *et al.* (2005); Kraus *et al.* (2000). These checks indicate that our models are correct, as we find good matches with all published spectra. These checks were done for a wide range of conditions: some of the published spectra are optically thin, some thick and others in different geometries.

2.2.3 Numerical Implementation

Our fitting and error determination routines are divided into several interacting packages. The innermost set of functions is responsible for calculating **optical depth spectra of CO gas** with a given emission line width. To decrease the computation time, we compute a table of line absorption coefficients $\mathrm{K}_{v\mathrm{J}v'\mathrm{J}'}$ at a given set of temperatures and determine the necessary values through interpolation (The indexes v and J are for the upper energy level, while, v' and J$'$ are for the lower energy level.) We also compute the line profile $\Phi_{v\mathrm{J}v'\mathrm{J}'}(\nu)$ for each line visible in the spectrum for an array of wavelengths in the interval $[\lambda_{\mathrm{line}} - 3\,\Delta\lambda_{\mathrm{g,emm}}\ .\ .\ \lambda_{\mathrm{line}} + 3\,\Delta\lambda_{\mathrm{g,emm}}]$. Before each request for a series of spectra the limits in interpolation temperature and wavelength are checked. If the fitting requires values out of the current range the table of absorption coefficients and line profiles is recalculated. Then the optical depth per column density $\left(\frac{\tau_\nu}{\mathrm{N}}(\mathrm{T})\right)$ and blackbody spectrum ($\mathrm{B}_\nu(\mathrm{T})$) are calculated for the required temperature. Calculating the optical depth is one of the two most numerically intensive steps as each line profile has to be multiplied with the interpolated absorption coefficient. Although the summation in Equation 2.5 adds all CO lines, only a few lines have to be considered for each frequency ν. All steps are optimized to ignore lines that are outside the wavelength range of the final spectrum.

A set of functions is responsible for the **geometry**, temperature distribution

and column density distribution of the gas. For each geometrical configuration (slab, shell, ring, . . .) a similar set of functions has been programed that is called by the overlying program through function pointers. Hence the overlying optimization and error plotting routines are independent of the gas structure and could be used for any other multi-parameter spectral fit. The geometry functions use the optical depth per column density $\frac{\tau_\nu}{N}$ and blackbody spectrum B_ν to determine emission from individual optical columns. This emission spectrum has to be convolved with the Doppler spectrum of the observed structure. This convolution is the second numerically intensive step and is optimized to use classical convolution or convolution by FFT depending on the width of the Doppler spectrum. For the disk the spectra of various rings are integrated numerically.

Various intervals and constants have to be set to balance the requirement for accuracy with the need to minimize the number of computations. The temperature interpolation interval was set to ensure that the fitted parameters do not change by more than 10% of the uncertainties estimated using the technique described below. The wavelength sampling interval ($d\lambda$) is about 1/3 of the equivalent width of $V_{g,emm}$. The number of steps in radius and phase angle has been set such that the maximal Doppler shift of adjacent computational cells is smaller than $d\lambda$.

We determine the best fit to our model by minimizing χ^2. This value is defined as

$$\chi^2 = \sum_i \frac{(d_i - f_i)^2}{\sigma_i^2} \tag{2.11}$$

where d_i are the data points and f_i the corresponding points in the model fit. The values σ_i are the measurements errors for the data points d_i. If the fit is appropriate then χ^2 should be similar to the number of degrees of freedom (dof). Otherwise the errors σ_i could be underestimated or a better model could be possible (if $\chi^2 >$ dof), the errors could be too large or the model have too many parameters

(if $\chi^2 < \mathrm{dof}$). The S/N ratio of the measured spectrum is used to determine χ^2 values. Minimizing χ^2 is equivalent to maximizing the likelihood for the model parameters. The probability for a certain parameter is proportional to

$$\mathrm{e}^{-\frac{\chi^2}{\mathrm{dof}}} \tag{2.12}$$

We use this formula for our error analysis. The fitting of the model uses a grid search in parameter space followed by Powell's method to find the minima in χ^2. This method repeatedly minimizes χ^2 for each parameter until the result changes by less than a value specified to represent less than 0.1σ error in the parameters. The ten dimensional χ^2 space has numerous local minima. Thus we improved our search by varying the parameters individually.

We estimate the uncertainties for each fitted parameter by calculating χ^2 as a function of each parameter, as shown in Figure 2.9. The plots illustrate the error analysis for the parameter $\mathrm{N_i}$ for the $2.36 - 2.39\,\mu$m spectral range of our NIRSPEC data of 51 Oph. For values of $\mathrm{N_i}$ between 6×10^{20} and 15×10^{20}, we minimize χ^2 by varying all of the other parameters using Powell's method, as described above.

The probability distribution for each fitted parameter is obtained by using Equation 2.12. As the residuals in our fits are generally larger than the $1-\sigma$ errors, we normalize the minimum χ^2 per degree of freedom to 1. The listed error for that parameter is the Gaussian width of this distribution. The χ^2 per degree of freedom plot shows local minima. This common property of the χ^2 space requires much fitting to find (probable) global minima. The probability somewhat resembles the Gaussian curve that was fitted to determine the error in $\mathrm{N_i}$. For parameters with an unambiguous value (ex: λ_{off}), the probability curve follows the fit closely, whereas the probability for parameters with several possible solutions (like β) looks much more noisy.

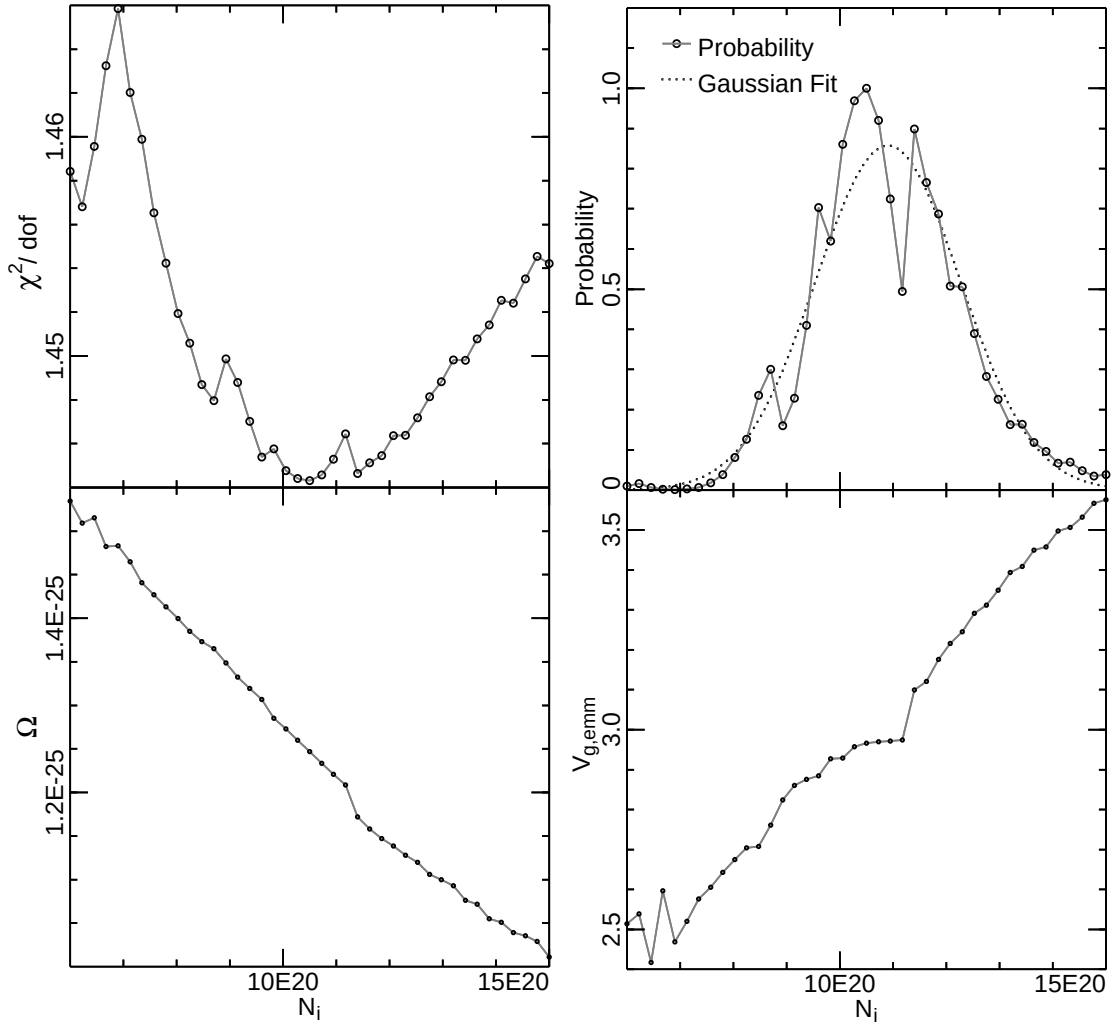

Figure 2.9: Error estimation for the fitting parameter N_i using the $2.36 - 2.39\,\mu$m spectral range. The top left graph shows the χ^2 per degree of freedom as a function of N_i. The probability for χ^2 per degree of freedom normalized to 1 is plotted in the top right graph. Also indicated in this graph is the Gaussian fit to the probability curve, which was used to determine the uncertainties in N_i. The two bottom graphs show how Ω and $V_{g,emm}$ change with respect to N_i. The units are the same as in chapter 4.

To test this method, we generated noisy synthetic spectra and used them to fit the parameters. We then compared the standard deviation of these parameters with the uncertainties obtained with our method, using the S/N that was used to create these synthetic spectra. Even without normalizing χ^2, the values agreed, thus validating our method.

The error analysis also yields information about how the different parameters depend on one another, as shown in Figure 2.9. The plots show how $V_{g,emm}$ and Ω vary with N_i as we minimize χ^2 as described above. Such correlations between parameters are seen in all of our fits.

A semi-automatic scripting program allows creation of all error plots for a given fit with minimal user interaction. This is important as the error determination is also used to ensure the current minimum in χ^2 is not a local one.

Even though this software has worked reliably one challenge is its use of large amounts of memory. Certain compilers can not create programs with that much variable space. Nevertheless the programmer wants to make sure sufficient memory is allocated as otherwise arrays can be overwritten causing mistakes by overwriting adjacent data. As the conditions slightly shift whenever the line strengths and profiles are recalculated it is possible that the search algorithm enters an infinite loop, requiring aborting the search. This inconvenience can be fixed by using more relaxed precision requirements.

2.2.4 Corrections and Improvements

Our model assumes a geometrically thin disk. We therefore ignore the change in radial velocity that occurs because the optical column through any point in the disk midplane includes different radial velocities. This effect increases with increasing disk thickness and increasing inclination.

A simple model using a thin cylindrical disk shows that the effect can be measured as follows: The disk is viewed under the inclination angle i and the optical column go through the disk midplane at a point where the line of sight component of the Keplerian velocity is V_0 and the azimuthal angle is ϕ. The gas at the surface of the disk at a distance Z from the disk midplane will have two contributions to the change in velocity relative to $\sin\phi\, V_0$: 1) the contribution from the change in Keplerian velocity from being further from / closer towards the central star and 2) having a different direction of said Keplerian velocity due to a different angle ϕ. The total difference in line of sight velocity in between a point in the disk midplane and at a vertical distance Z, $V_{\mathrm{ls\,diff}}$, is equal

$$V_{\mathrm{ls\,diff}} = \frac{3}{4} V_0 \,(Z/R) \sin 2\phi \tan i \tag{2.13}$$

where Z/R is the disk thickness over the local radius, V_0 the orbital velocity at the observed distance form the star, ϕ the azimuthal angle (with $\phi = 0^o$ being towards the observer). We assumed that the disk is thin and neglected any $(Z/R)^2$ or higher order terms. If the disk has a vertical Gaussian density profile with a width ΔZ, the above formula also gives the Gaussian width of the emission from the optical column $\Delta V_{\mathrm{column}}$.

To check and improve on our formula above we programed a simple model of a Keplerian disk with such a Gaussian vertical gas density profile. The model determines the amount of gas in each optical column as a function of radial velocity towards the observer. Such profiles are shown in figure 2.10. In accordance with our formula above the profiles are widest at $\phi = 45^o$. The profile at $\phi = 70^o$ (dark gray curve) is interesting, as it goes to larger velocities than the profiles at larger azimuth angles ($\phi = 80$, 90^o). This is because the $\phi = 70^o$ optical column crosses the $\phi = 90^o$ plane at smaller distance to the star, hence at a larger Keplerian velocity. The widths of these profiles in function of azimuth angle are shown in

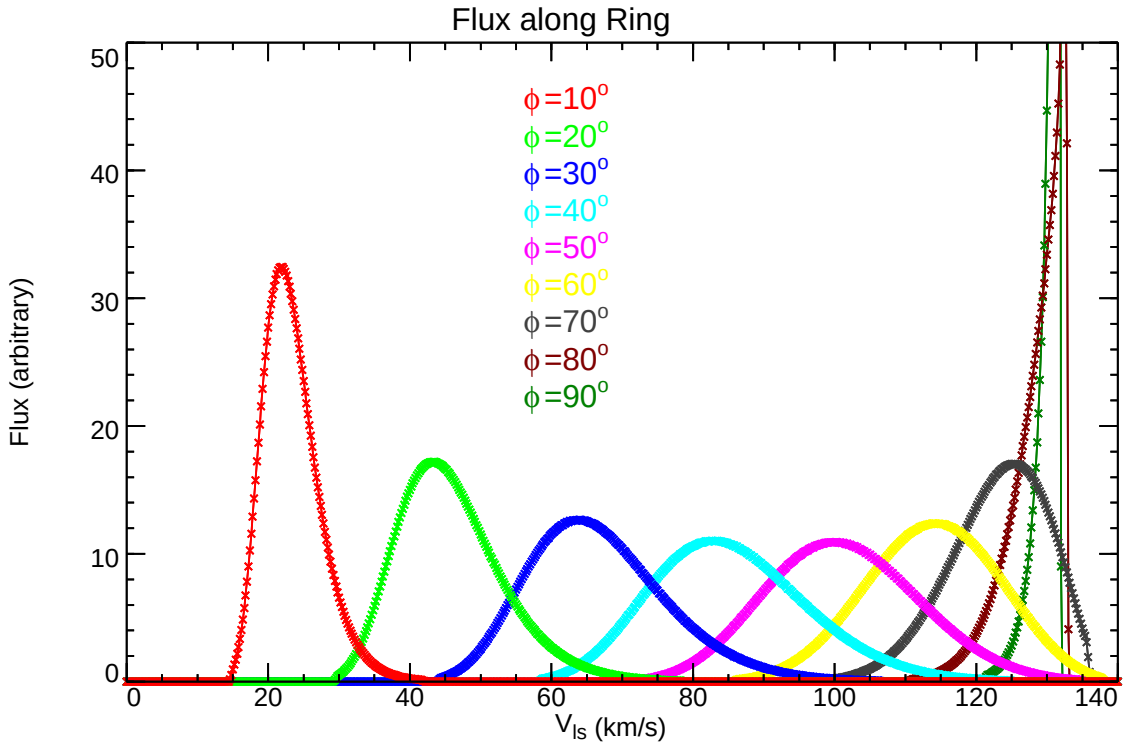

Figure 2.10: Velocity profiles of optical columns in a Keplerian disk. The model was calculated for i = 80°, Z/R = 0.02 and V_0 = 134 km/s. Shown are the profiles for a series of azimuthal angles ϕ. Each data point represents the amount of gas in that particular optical column with that particular velocity towards the observer.

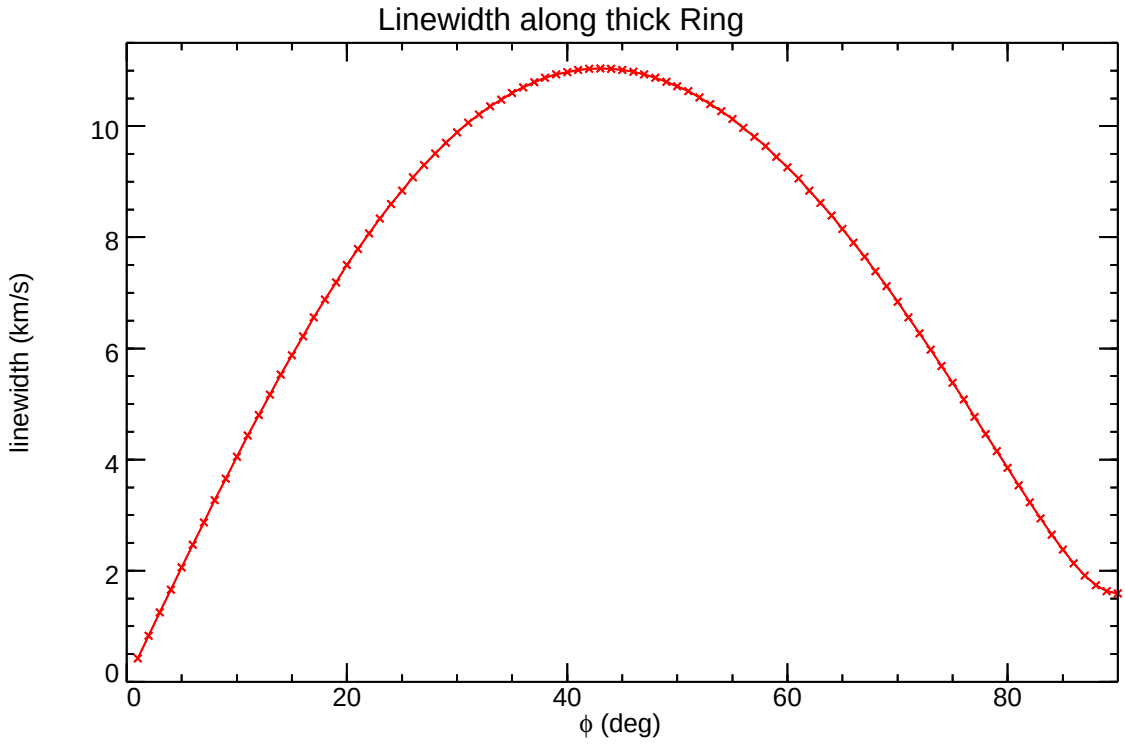

Figure 2.11: Gaussian width of the emission profile for the optical column of a disk in function of azimuth angle ϕ. The plot essentially shows the widths of the curves in figure 2.10.

Figure 2.11. The curve roughly agrees with the $\sin 2\phi$ behavior of Equation 2.13 except at $\phi = 90^{\circ}$ where higher order ΔZ/R terms become important. Comparing our plot with Equation 2.13 gives $\Delta V_{column} = 11.4\,km/s$ at $\phi = 45^{\circ}$, which is very close to the maximum in Figure 2.11.

For an optically thin disk this process does not affect the fitting. For an optically thicker disk, we would expect the following effects: The emission line width will be thinner and mostly determined by the thermal and turbulent motion of the gas at $\phi = 0,\ 90^{\circ}$. For intermediate ($\phi = 45^{\circ}$) regions the line width will be wider, hence (as discussed above) the fitted column density will be lower. This effect will affect the emission line profile of the disk, decreasing the flux at the spikes and in the middle of the M-shaped disk profile. The emission line width we measure in the disk will also be affected by this result.

We combined the cylindrical disk model discussed earlier in this section with our CO emission model to check these predictions. The effect of the larger optical depth is usually weak. The shape of the spectrum only changes significantly when Z/R becomes similar to cos i at an average optical depth of a few or higher. In that case the shoulder shortward of the bandhead maximum becomes less pronounced and the ridge between the shoulder and the maximum becomes straighter, maybe somewhat convex.

Another effect affects our model: If the velocity width in the observed column (ΔV_{column}) is larger than the emission line width of a parcel of gas within the column, the gas in the column will not emit coherently, hence not contribute to the optical depth τ at the same wavelengths. Our model could interpret such emission as coming from separate parts of the disk and underestimate the column density N, while overestimating the solid angle Ω. The values of N and Ω would thus be lower and upper limits respectively. This effect does not affect the total

mass which is $\propto N\,\Omega$.

This issue can be summarized as following: What emission line width $V_{g,emm}$ and column density N_{col} are measured from an optically thick column with a velocity dispersion along the optical column? Fitting simulated data using our rotated and stretched slab model indicate the following result: Both the emission line width and the velocity dispersion are measured as the emission line width $V_{g,emm}$ and the column density reflects the density and emission line width of the entire column, not just the gas part that emits coherently. This result indicates that the dispersion in the optical column effectively decreases the optical depth according to the following formula:

$$V_{g,emm}(\text{fitted}) = \sqrt{V^2_{g,\text{turbulence\&thermal}} + \Delta V^2_{col}} \tag{2.14}$$

For high optical depth disks we therefore expect the M-shaped profile to be altered as described above. It is unclear what effect this alteration has on our fitted spectra. Turbulent motion in the disk and high inclination effectively lower the measured optical depth in the gas (i.e. they increase the fitted emission line width $V_{g,emm}$). However, our measured column density N as well as the solid angle Ω are accurate.

An improved model would require integration of the optical depth along the optical column for each point in the disk. Fitting such a model is currently beyond the scope of this work.

Chapter 3
Survey of CO Emission from HerAeBe Stars

3.1 Introduction

The survey presented here tries to address two issues related to HAeBe stars: First, the amount and evolutionary history of the CS gas close to the star. This knowledge is important to understand planet formation and migration in these regions, and to understand the interaction between the disk and the star. We use the CO overtone bands to accomplish this. The second question we try to address is the reliability of using line emission to measure accretion rates in these systems. We answer this questions using UV line fluxes from the literature as well measured Brγ fluxes. We acquired K-band spectra, which contain the CO overtone bands as well as the Brγ line. Analysis of high resolution spectra of CO overtone bands will be presented in the following chapters.

3.1.1 Disk Surveys

An earlier survey of the infrared excess of HAeBe stars was done by Malfait *et al.* (1998). They modeled the stellar spectra of visible and infrared colors using a hot optically thick dust disk model. Their results suggested an evolutionary sequence from an embedded star to a star with a disk which later disappears. Later studies by Meeus *et al.* (2001), Dullemond & Dominik (2004) and Acke & van den Ancker (2004) suggested that all HAeBe stars have a geometrically thin optically thick dust disk with an extended dusty atmosphere. This disk atmosphere can initially be illuminated by the star. The dust disk probably also has a puffed up inner rim

(Dullemond & Dominik, 2004). As the dust grains grow the disk flattens and it becomes self-shadowed by it's own puffed up inner rim.

Circumstellar gas is certainly present in many HAeBe disks but is harder to observe. Gas emission lines can be observed from the star, from an optically thin inner disk (inside the dust sublimation radius), from a thin atmosphere of an optically thick disk with a temperature gradient, from an optically thin outer disk or from an optically thin gap in an otherwise thick disk (Najita *et al.*, 2007). It is also possible to see gas emission from disks with larger dust grains (hence optically thin) but where gas is still abundant. Gas can be excited and heated to emit by stellar radiation, gas collisions (thermal), mechanical heat (accretion), MHD waves or by interaction of the disk with the stellar wind (Carr *et al.*, 1993). Recent results in high resolution observation of circumstellar gas are reviewed by Najita *et al.* (2007). As at this time it is not possible to spatially resolve the disks (especially the inner disk regions) the emission is observed at high spectral resolution and different gas components are identified by their Doppler shift. Such studies show abundant ro-vibrational lines from molecules. Atomic transitions of neutral and ionized atoms are also observed. These observations allow us to measure temperature as well as the column density and the abundance of the circumstellar gas. Depending on the viewing geometry, a large Doppler shift is measured for gas in fast in- or outflows, as well as for gas close to the star with a large Keplerian velocity.

Past observations of gas in the disks of YSOs include:

- FUV pumped emission from **Molecular Hydrogen** (H_2) has been observed from most CTTS. The observations are consistent with models of H_2 in disks and outflows Najita *et al.* (2007). Infrared ro-vibrational lines (like the $v = 1 \rightarrow 0$ S(1) line) were observed in some CTTS and one WTTS. Pure

rotational lines are seen. Such observations help determine the total gas mass in the disk.

- High resolution observations of **Carbon Monoxide** (CO) overtone emission exist from numerous YSOs (Carr *et al.*, 1993; Chandler *et al.*, 1995; Najita *et al.*, 1996b; Kraus *et al.*, 2000; Carr *et al.*, 2004; Thi *et al.*, 2005). This type of emission requires warm (T > 2000K), dense (n > 10^{10}cm^{-3}) gas (Scoville *et al.*, 1980). These conditions are met in inner gas disks, the inner regions of winds as well as inside accreting funnel flows. However, such emission is only detected from a small number (5-10%) of the observed objects. Most CO overtone emission originates from circumstellar disks, as shown by the symmetric, double peaked profiles (Najita *et al.*, 2007). Observations of superthermal line broadening by Carr *et al.* (2004) and Hartmann *et al.* (2004) as well as our observations (see Chapters 4 and 5) show that turbulence is significant in the disk. The turbulence and the related release of accretion energy could be a significant source of heating and viscosity in the disk (Carr *et al.*, 2004). Other possible sources for heating the gas are direct starlight and other sources listed earlier in this section.

  CO fundamental emission is much more common and is observed from a large number of sources (Brittain & Rettig, 2002; Brittain *et al.*, 2003; Piétu *et al.*, 2003; Najita *et al.*, 2003; Blake & Boogert, 2004; Dent *et al.*, 2005; Najita *et al.*, 2007). The Einstein coefficients (A-values) for these emission lines are several orders of magnitude larger than for the overtone emission. Hence gas at lower densities and excitation temperatures can be detected in these lines (Carr *et al.*, 2004). Fundamental emission from CO is therefore observed from a larger range of excitation temperatures than overtone emission. Usually the lines are centrally peaked which indicates low Keplerian velocities

and are seen from gas ranging from 0.1 to 2AU for TTS. ^{13}CO fundamental emission is also observed (Najita *et al.*, 2007). The inner edge of the CO emission region is observed inside the dust sublimation and inside corotation radii. Interesting are the observations from the HAeBe star HD141569 where the vibrational excitation temperature is higher than the rotational excitation temperature indicating that the gas is pumped by stellar UV radiation (Brittain *et al.*, 2003). Therefore the gas is probably in a disk atmosphere that is illuminated by direct starlight.

- Emission from **Water** (H_2O) is observed from numerous YSOs. Colder water is observed in the outer disk regions (Carr *et al.*, 2004; Najita *et al.*, 2007). Observations of water from the YSO SWS 13 indicate that the water abundance is lower by one order of magnitude than would be expected from chemical models (Carr *et al.*, 2004).

- A survey of **Atomic Lines** by Vieira *et al.* (2003) shows that such lines are abundant in the 131 YSOs they studied. Hα emission from more than half the re-observed objects showed variations in flux and line shape on a timescale of months and years. They also observed that forbidden line emission (OI and SII) are more common in stars with large IR excesses, that indicate the presence of photon dominated regions.

3.1.2 Measuring Accretion Rates

Measuring accretion luminosity (L_{acc}) for HAeBe stars is difficult because the techniques commonly used for TTS can not easily be applied: Accreting gas usually has a temperature around 10,000K (Valenti *et al.*, 2000). L_{acc} is measured from the UV excess above the stellar photospheric spectrum. Such a spectrum is shown in Figure 3.1 for the IMTTS EZ Ori. Shortward of $\approx$ 2600Å most of the flux is

UV excess caused by accretion. The accretion rate can be estimated by equating L_{acc} with the potential energy lost by the accreting material:

$$\dot{M} = \frac{L_{acc}\, r_*}{G\, M_*} \tag{3.1}$$

where r_* and M_* are the stellar radius and mass respectively.

For HAeBe stars however, the photosphere has a similar effective temperature to the accretion flux. Hence no separate accretion and photospheric components can be identified in the spectrum. Figure 3.2 shows such a spectrum. The different plots show that the measured UV excess can depend critically on the measured or assumed extinction value (A_V). In the UV the extinction by CS and interstellar material is significant as extinction can decrease the stellar UV flux by more than one order of magnitude. This makes it important to have the correct extinction value as well as a applicable extinction curve. Another method to measure accretion is to use tracers such as line emission usually present in spectra of accreting systems. Such lines in the UV (e.g. MgII and CIV lines) are subject to extinction just like the rest of the UV spectrum. Lines in the IR on the other hand have to be corrected for veiling by CS infrared excess emission. As this paper will compare such techniques, we discuss them later in more detail.

Another approach to measure L_{acc} is to consider a variety of accretion indicators. Grady *et al.* (2007) use the presence of jets, Herbig Haro knots and lines with P-Cygni profiles to constrain the accretion of HD169142. In other papers the same authors use variations in the FUV flux from the star. As L_{acc} for a particular source is known to vary over time they assume that the lowest measured flux is from the stellar photosphere only and that any larger flux is due to accretion. The results from this method still depend on the extinction measurements, thus it requires concurrent observations to determine these values. Grady *et al.* (2007) find that the accretion rate for HD169142 is below $10^{-9} M_\odot$/yr.

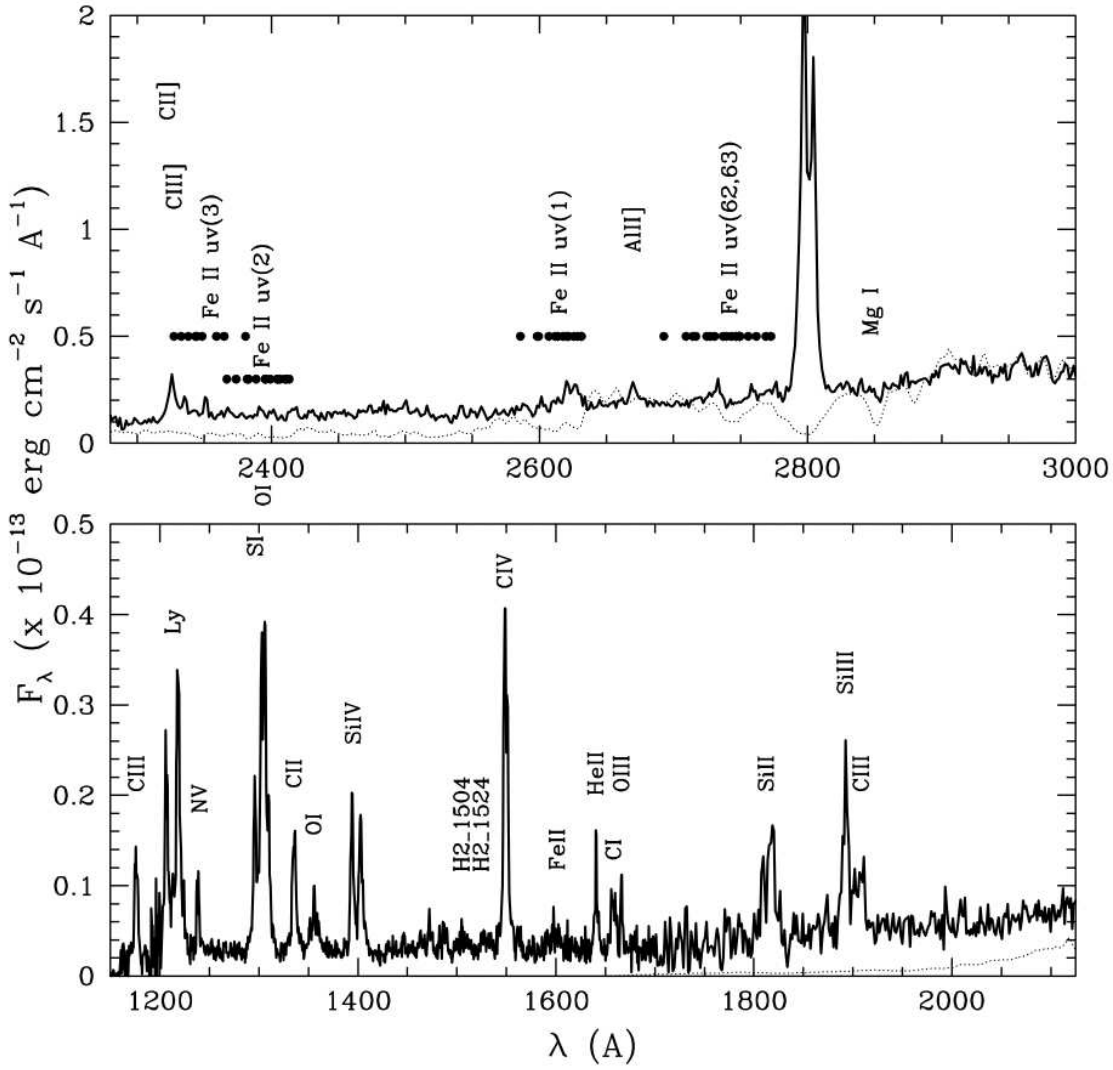

Figure 3.1: UV spectrum of the IMTTS EZ Ori. The plot was taken from Calvet *et al.* (2004). The data was obtained using HST. The dotted line shows a model of the photosphere scaled using V photometry. The various UV lines are identified.

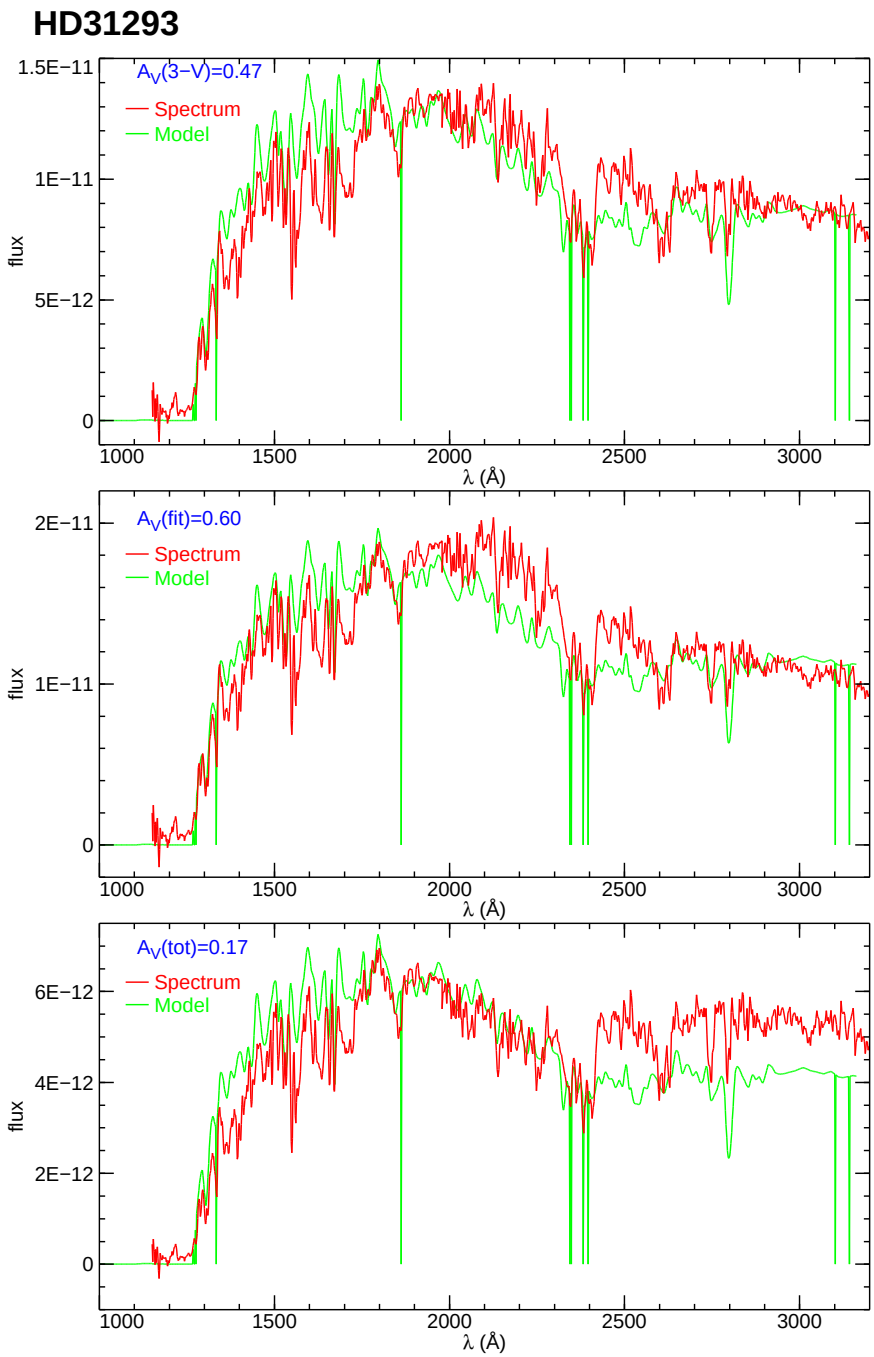

Figure 3.2: UV spectrum of the Herbig Ae/Be star HD31293. The UV spectrum was obtained by the IUE satellite and reduced by Valenti *et al.* (2000) and Valenti *et al.* (2003). The model spectrum is the stellar model by Kurucz (1992). The model spectrum is medium fitted to the data. To show the effect of extinction correction we show the spectrum dereddened using the 3000Å − V correction and the extinction value from the spectral fit by Valenti *et al.* (2003) as well as the extinction value determined by Malfait *et al.* (1998).

Bracket Gamma (Brγ) emission is proposed as an indicator of accretion by various authors (Najita *et al.*, 1996a; Muzerolle *et al.*, 1998; Calvet *et al.*, 2004; Garcia Lopez *et al.*, 2006). In YSOs there are two contributions from Brγ to the stellar flux: Stars warmer than about F8 have Brγ absorption in their photosphere. CS infrared excess emission can veil this absorption line. The second contribution is Brγ emission from accretion processes, a hot disk and/or wind (Najita *et al.*, 1996a).

Early high resolution spectral observations of Brγ emission from 6 CTTSs were made by Najita *et al.* (1996a). The lack of blueshifted absorption indicates that the winds flowing towards the observer are colder than previously thought. They also observed redshifted absorption indicating that the absorption was mostly caused by *infalling* gas instead of outflowing winds. The asymmetry of the lines indicate that Brγ emission is associated with accretion instead of disks. A larger survey was done by Muzerolle *et al.* (1998). They looked at the Brγ and Paβ lines from 30 TTSs and measured L_{acc} using visible and UV colors. Both Brγ and Paβ lines are correlated with L_{acc}. The correlation found by Muzerolle *et al.* for the Brγ line is:

$$\log\left(\frac{L_{acc}}{L_{\odot}}\right) = 1.26\log\left(\frac{L_{Br\gamma}}{L_{\odot}}\right) + 4.43 \tag{3.2}$$

A survey focusing on 9 more massive IMTTSs was done by Calvet *et al.* (2004). The goal of their study was to obtain reliable values for the spectral class, extinction and veiling. They used simultaneous multi-wavelength observations of colors and spectra spanning from the UV to the IR. Simultaneous observations in the different spectral ranges were necessary as some objects show brightness variations. They used an $R_V = 3.1$ extinction law with a weaker 2200Å graphite feature than the law proposed by Cardelli *et al.* (1989). This extinction law proved to reliably fit the extinction for stars located behind the Taurus star forming region. One of

their UV spectra is shown in Figure 3.1. The spectrum shows the photosphere with a blackbody temperature of 5000-6000K and the accretion emission with a temperature of $\approx$ 8000K. They obtained the $\dot{M}_{acc}$ by using the formula above with r_* and M_* from stellar models. They also observed Brγ emission and corrected the equivalent width for veiling as we describe below. They found that Brγ emission is consistent with magnetospheric accretion models and confirmed and extended the relationship between Brγ flux and L_{acc} proposed by Muzerolle *et al.* (1998). Their extended relationship is

$$\log\left(\frac{L_{acc}}{L_\odot}\right) = -0.7 + 0.9\left[\log\left(\frac{L_{Br\gamma}}{L_\odot}\right) + 4.0\right] \tag{3.3}$$

which agrees with above formula in the $\log\left(\frac{L_{Br\gamma}}{L_\odot}\right) = -6$ to -2 range covered by the data. However, the $\log\left(\frac{L_{acc}}{L_\odot}\right)$ values can deviate by up to one order of magnitude.

A survey of Brγ from HAeBe stars was done by Garcia Lopez *et al.* (2006). They analyzed high and medium resolution spectra of Brγ emission from 27 sources and used similar procedures as we describe below to correct for veiling and photospheric emission. Using above formula from Calvet *et al.* (2004) to calculate L_{acc} they found that the accretion rate for these systems is small with a lower $\dot{M}/M_*$ than TTSs.

Another possible indicator of accretion are **atomic UV emission lines**. In particular the CIV line at 1548Å and the MgII line at 2800Å are shown to correlate with L_{acc}. The first survey of MgII UV lines from HAeBe stars was made by Imhoff (1994). She found that most HAeBe stars with large IR excess have P Cygni line profiles in UV lines (large blue shifted absorption with redshifted emission). This type of line profile (also seen in Hα) is thought to be an indicator for accretion and winds.

A survey of UV spectra of YSOs (HAeBe stars and TTSs) was done by Valenti *et al.* (2000) and Valenti *et al.* (2003). They reduced all available high resolution spectra from the IUE satellite. The results from the $1200 - 1900$Å wavelength

range are in Valenti *et al.* (2000) and the results from the $1900 - 3200$Å range are in Valenti *et al.* (2003). Their spectra were used in Figure 3.2. Valenti et al. fit the UV spectra to determine exact type and extinction. They use an $R = 3.1$ extinction law and find that more than half of the HAeBe stars have UV continuum flux variations larger than 10%. Atomic lines are seen in HAeBe spectra, like the MgII line (mostly from colder stars) and numerous FeII lines in absorption and emission. The example in Figure 3.2 shows some MgII absorption and maybe CIV absorption. However both of these signals are weaker than the expected absorption from the photospheric model. In CTTSs however, the lines are much stronger. In the spectra of most cooler (CTTS and IMTTS) stars many UV atomic lines are several times brighter than the continuum (see Figure 3.1).

The short wavelength spectra of 49 TTS from Valenti *et al.* (2000) were analyzed by Johns-Krull *et al.* (2000). Using accretion value from the literature derived from visible spectra and high resolution line spectra they find the following correlation between the CIV 1548Å line flux and the accretion rate:

$$\log\left(\dot{\mathrm{M}}\right) = 0.75\log\left(\mathrm{E_{CIV}}\right) - 30 \tag{3.4}$$

where $\dot{\mathrm{M}}$ is measured in $\mathrm{M_\odot/yr}$ and E, measured in 10^6 ergs/s, is the luminosity of the line. However the validity of this correlation depends on the literature source for the accretion rate and the extinction values. They also find correlations between other line UV line fluxes and accretion.

The survey of Calvet *et al.* (2004) mentioned above also analyzes correlation between UV lines and $\mathrm{L_{acc}}$. For the IMTTSs they surveyed most UV atomic lines like the MgII and the CIV line are very strong, as can be seen in Figure 3.1. Calvet *et al.* (2004) find that the MgII line flux correlates with $\mathrm{L_{acc}}$ according to

$$\log\left(\frac{\mathrm{L_{MgII}}}{\mathrm{L_*}}\right) = -2.5 + 0.8\left(\log\left(\frac{\mathrm{L_{acc}}}{\mathrm{L_*}}\right) + 1.26\right) \tag{3.5}$$

and the CIV line flux according to

$$\log\left(\frac{L_{CIV}}{L_*}\right) = -3.5 + 0.5\left(\log\left(\frac{L_{acc}}{L_*}\right) + 1.26\right) \tag{3.6}$$

Some of the measured stars differ from the fit by up to half an order of magnitude. We will use these empirical relations to compare to our L_{acc} obtained from the Brγ measurements.

The next section describes our procedures for data reduction and analysis. The following section describes our results, which are discussed in section 4. A short conclusion section completes the chapter.

3.2 Observations and Data Reduction

The **goal of our observation** was to take K-band spectra of all stars in the list by Malfait *et al.* (1998). The signal / noise should allow us to identify significant features including CO overtone and Brγ emission. The targets we observed are listed in table 3.1. It contains all stars on the Malfait *et al.* (1998) list observable from the northern hemisphere.

We used the **PHARO instrument at Mount Palomar Observatory** in December 2003 and September 2004. Due to bad weather we didn't get any data on another observing run at Palomar in February 2005. The Telescope is located at 33° 21' 22" North, 116° 51' 53" West at 1710m above see level on Palomar Mountain. For our observations we used the 5.08m (200") Hale Telescope with the adaptive optics guiding system. As we looked exclusively at bright stars we could guide the AO system using the star itself.

The PHARO camera we used is a cryogenically (liquid Helium) cooled near-infrared imager and spectrograph (Hayward *et al.*, 2001). It allows J, H and K-band

Table 3.1: List of surveyed Herbig Ae/Be stars: The names in the first column are used throughout the paper. All the types are from the Simbad website. The last column lists where the star was observed as follows: PA03 and PA04 are for Palomar observations on December 2003 and September 2004, SP05 and SP06 represent SPEX observations at IRTF on February 2005 and February 2006, NS03 stands for NIRSPEC at Keck on June 2003 and CS5 represents CSHELL observations at IRTF on February 2005. This list also includes objects later found to have binary companions.

Name (Alt Name)		Type	RA & Dec (J2000)		M_K	Observations
HD17081		B7 IV	02 44 07.3	-13 51 31	4.51	PA03, PA04 SP06
AB Aur	HD31293	A0 V pe	04 55 45.8	30 33 04	4.3	PA03, PA04
HD31648		A3 pshe+	04 58 46.3	29 50 37	5.69	PA04
HD34282		A0e	05 16 00.5	-09 48 35	7.42	PA04, SP05
HD35929		A5	05 27 42.8	-08 19 38	6.76	PA04
HD36112		A3e	05 30 27.5	25 19 57	5.9	PA04
HD244604		A3	05 31 57.3	11 17 41	7.21	PA04
HD36917	V372 Ori	A0 V	05 34 47.0	-05 34 15	6.4	PA03, CS05
HD37258		A2 V	05 36 59.3	-06 09 16	7.66	SP05
HD37357		A0 V e	05 37 47.1	-06 42 30	7.24	SP05
HD37411		B9 V	05 38 14.5	-05 25 13	7.55	SP06
MWC 120	HD37806	A0 V	05 41 02.3	-02 43 01	5.77	SP06
HD41511		A2 esh	06 04 59	-16 29 04	1.67	SP05
MWC 147	HD259431	B6 Vpe	06 33 05.2	10 19 20	5.62	PA03, SP06
MWC 158	HD50138	B9 esh	06 51 33.4	-06 57 59	4.18	PA03
HD56895B		F0 V	07 18 31.8	-11 11 34	3.56	PA03, SP06
HD58647		B9 IV	07 25 56.1	-14 10 43	5.43	PA03, CS05
HD141569	BD - 03 3833	A0 V	15 49 57.8	-03 55 16	6.82	NS03, PA04
HD142666	BD - 21 4228	A8 V e	15 56 40.0	-22 01 40	6.04	NS03
HD143006	He 3 - 1126	G6/G8	15 58 36.9	-22 57 15	6.73	NS03
HD144432	He 3 - 1141	A9 V	16 06 58.0	-27 43 10	6.14	NS03
HD149914		B9.5 IV	16 38 28.7	-18 13 14	5.74	NS03
HD150193	V* V2307 Oph	A1 V e	16 40 17.9	-23 53 45	5.64	NS03
51 Oph	HD158643	B9.5 V e	17 31 25.0	-23 57 46	4.31	NS03, PS04
HD163296	He 3 - 1524	A0 Vesph	17 56 21.3	-21 57 22	4.7	NS03
HD169142		B9 V e	18 24 29.8	-29 46 49	6.53	NS03
MWC 614	HD179218	B9 e	19 11 11.3	15 47 16	5.91	NS03, PA04
HD190073	V1295 Aql	A2 IV ep	20 03 02.5	05 44 17	5.78	NS03, PA04
MWC349	V* V1478 Cyg	Bpe	20 32 45.4	+40 39 37	3.15	NS03

imaging using various filters. In spectroscopic mode the instrument has a resolution of about $\frac{\lambda}{\Delta\lambda} \sim 1200$. The detector is a NICMOS 1024^2 HgCdTe detector. For our observations we used the 40" field of view (designed to work with the grisms) and a slit 0.26" wide. For spectral selection and dispersion we used the K-band grism and the corresponding filter.

The other instrument we used is the **SPEX instrument** at the **IRTF**. We observed on SPEX in February 2005 and in February 2006. Our 2006 observations were conducted while observing remotely from Ithaca College. IRTF (Infra-Red Telescope Facility) is located at the top of Mauna Kea at 19° 49' 34" North, 155° 28' 19" West and at an altitude of 4200m. The 3 meter telescope is optimized for infrared astronomy and allows a spatial resolution of 0.4" at 2.2μm. The SPEX instrument is a near infrared (0.8-5.5μm) spectrograph (Rayner *et al.*, 2003). The instrument has a low resolution (R $\sim$ 200) mode and cross-dispersed as well as single order high resolution (R $\sim$ 2000) modes. The instrument is cryogenically cooled using liquid nitrogen and uses a 1024×1024 InSb detector array with 0.15" per pixel resolution. A $60'' \times 60''$ slit viewer with a separate detector allows to position the telescope. We used the instrument in high resolution single order mode as only K-band spectra were required for our survey. The narrowest, $0.3'' \times 15''$ slit was used.

The observations were planned and executed as described in chapter 2. The list of calibrator stars we used is given in Table 3.2. Bright calibrators are rare as the calibrators need to be close to the observed stars. As we needed two (A-type and K-type) calibrators for each star, we spent considerable time observing these calibrators.

We reduced the data as described in chapter 2, using software written in IDL and C. For the SPEX data we used the Spextool package written by Cushing *et al.*

(2004). This tool was designed specifically to reduce near infrared cross dispersed spectra. Most of our reduction routines for the PHARO data were written by Luke Keller and David Whelan. The data was further analyzed using custom IDL and C programs.

3.3 Results

3.3.1 Spectra

The extracted spectra with telluric correction are shown in Figure 3.3. The model spectra shown are from from Kurucz (1992). These model spectra we used were packaged as part of the IUE data analysis software by the IUE Data Analysis Center at Goddard Space Flight Center. Throughout the paper we use this version of the Kurucz models. The data was reduced as described in the last section. Most stars have either Palomar or IRTF data, HD258431 has both, as can be seen by the higher quality and wavelength range of the IRTF data. For each star the spectra from all observations are shown with all the applicable calibrators. The spectra were corrected for extinction using the $R_v = 3.1$ extinction law by Cardelli *et al.* (1989), which is most often used in the literature. An IDL software package written by Elise Furlan was used for the extinction correction. The software relies on a table of extinction values which are interpolated and multiplied with the stellar extinction A_V. Calculation of the extinction values A_V is described below.

The S/N varies for different spectra. Some sources have a S/N below 100. No clear fringing pattern are visible in any of the spectra. The average slope of the spectra is determined by the photospheric spectra and the amount of infrared excess of the star. For many HAeBe stars with infrared excess the spectrum starts to deviate from the stellar spectrum around 2.1μm. This causes the spectra of

Table 3.2: List of calibrator stars. The stars are listed in order of increasing right ascension. To minimize confusion between target and calibrator stars, we referred to the calibrator stars by using their SAO number. Temperatures are in degrees kelvin. Most data are from the Simbad online database, the K-band magnitudes are from the 2MASS survey.

SAO#	HD#	Type	T_{eff}	RA & Dec (J2000)		M_K	Comment
148385	15130	A0 V	9520	02 25 57.0	-12 17 26	4.8	
148386	15144	A6 V	8030	02 26 00.4	-15 20 29	5.6	Variable Star
129984	16074	K4 III	4000	02 34 42.6	-07 51 34	2.4	Double System
75610		K0	5250	02 52 14.4	+29 47 14	6.2	
130197	18322	K1 III	4600	02 56 25.7	-08 53 53	1.47	Variable Star
57454	30651	K0	5250	04 50 48.1	+31 33 57	3.3	
77017	33413	A0	9520	05 11 18.1	+29 43 48	7.1	
112588	34317	A0V	9520	05 16 41.0	+01 56 50	6.3	
132036	35154	K0	5250	05 22 20.7	-08 15 43	6.3	
132157	36058	A0Vn	9520	05 28 56.9	-03 18 27	6.3	Double or Multiple
94622	244591	K5	4350	05 31 52.6	+11 12 15	5.5	Variable Star
77244	36469	K0	5250	05 32 58.0	+25 53 39	4.2	
94664		A2	8970	05 34 53.4	+11 10 04	8.4	
77281	36793	A0	9520	05 35 17.2	+25 49 44	7.4	
132463	37887	A0V	9520	05 41 36.0	-03 43 52	7.7	
132493	38225	K0	5250	05 44 02.8	-04 33 32	5.2	
113868	45137	A0V	9520	06 25 46.5	+02 16 18	6.5	
95769	258823	A5	8200	06 31 12.4	+10 07 05	8.1	
133645	48922	A0	9520	06 45 50.1	-00 42 59	6.8	
133807	50282	K0	5250	06 52 22.9	-05 18 59	4.3	
114626	50931	A0V	9520	06 55 34.6	+08 19 27	6.1	
173168	173168	A0IV/V	9520	07 11 41.6	-20 52 59	5.8	
152654	56525	A0V	9520	07 16 47.1	-13 40 52	7.0	
152839	58462	A1V	9230	07 25 06.8	-14 53 00	6.6	
153409	63323	K5II/III	3950	07 47 45.2	-16 00 52	2.0	Variable Star
140853	142864	A0	9520	15 57 08.6	-06 17 48	6.7	
140947	144390	K0	5250	16 05 59.8	-06 08 23	3.9	
185367	157527	K0III	4750	17 24 42.0	-21 26 29	3.8	Double or Multiple
186061	163955	B9V	10500	17 59 47.6	-23 48 58	4.5	
104503	178331	K0	5250	19 07 37.0	+16 17 24	5.2	
104650	180216	A2	8970	19 15 08.8	+16 11 50	7.1	
125372	189823	A0	9520	20 01 54.1	+05 53 42	8.5	
125411	190410	K2	4900	20 04 35.1	+06 11 02	6.5	

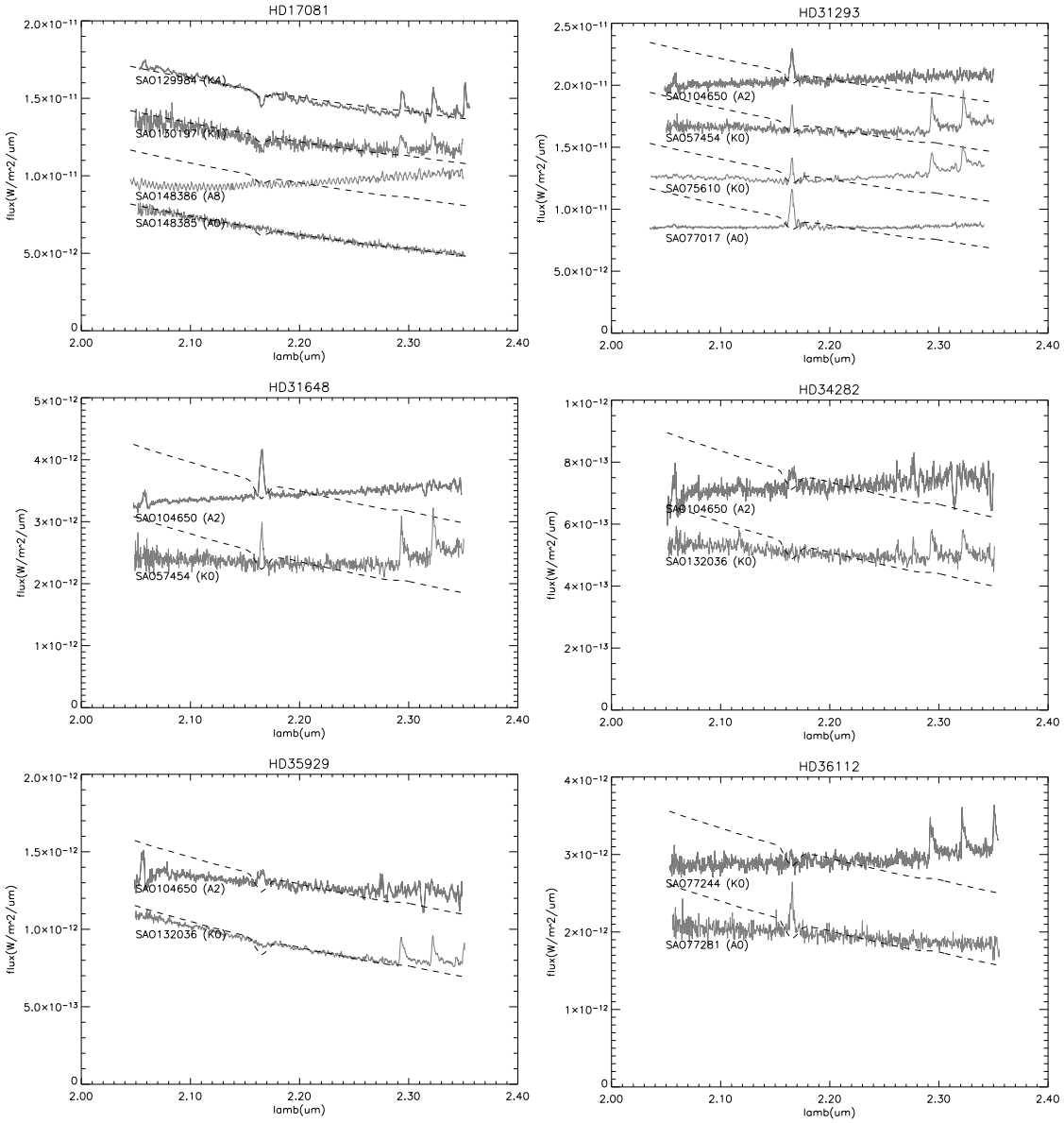

Figure 3.3: Low resolution spectra: For each star the reductions with each calibrator are shown with SAO number and spectral type of the calibrator. The dashed line in the background indicates the model spectrum by Kurucz (1992) average scaled to the spectrum. In each plot, the spectra above the bottom one are offset for illustration purposes.

Figure 3.3 (continued)

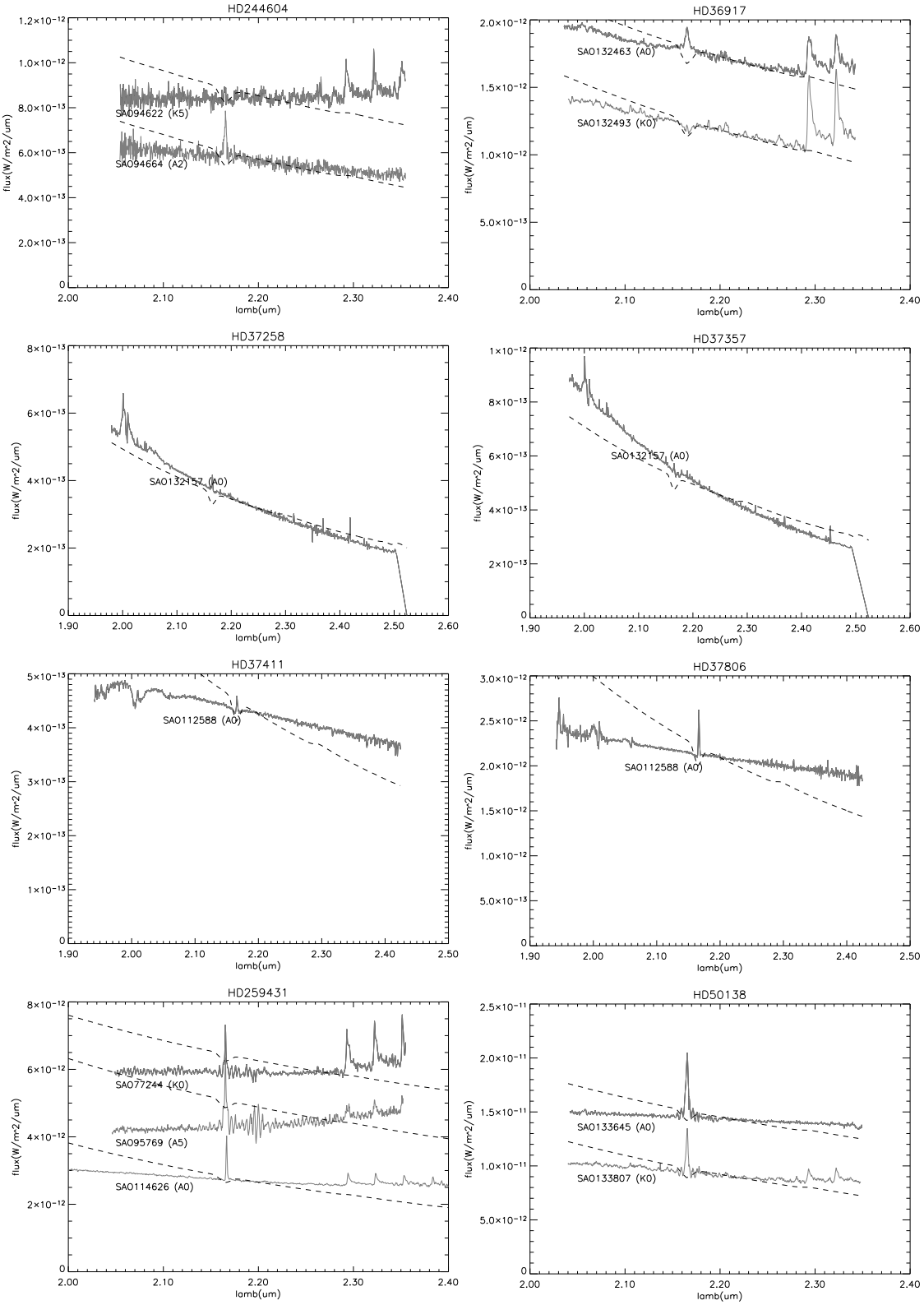

Figure 3.3 (continued)

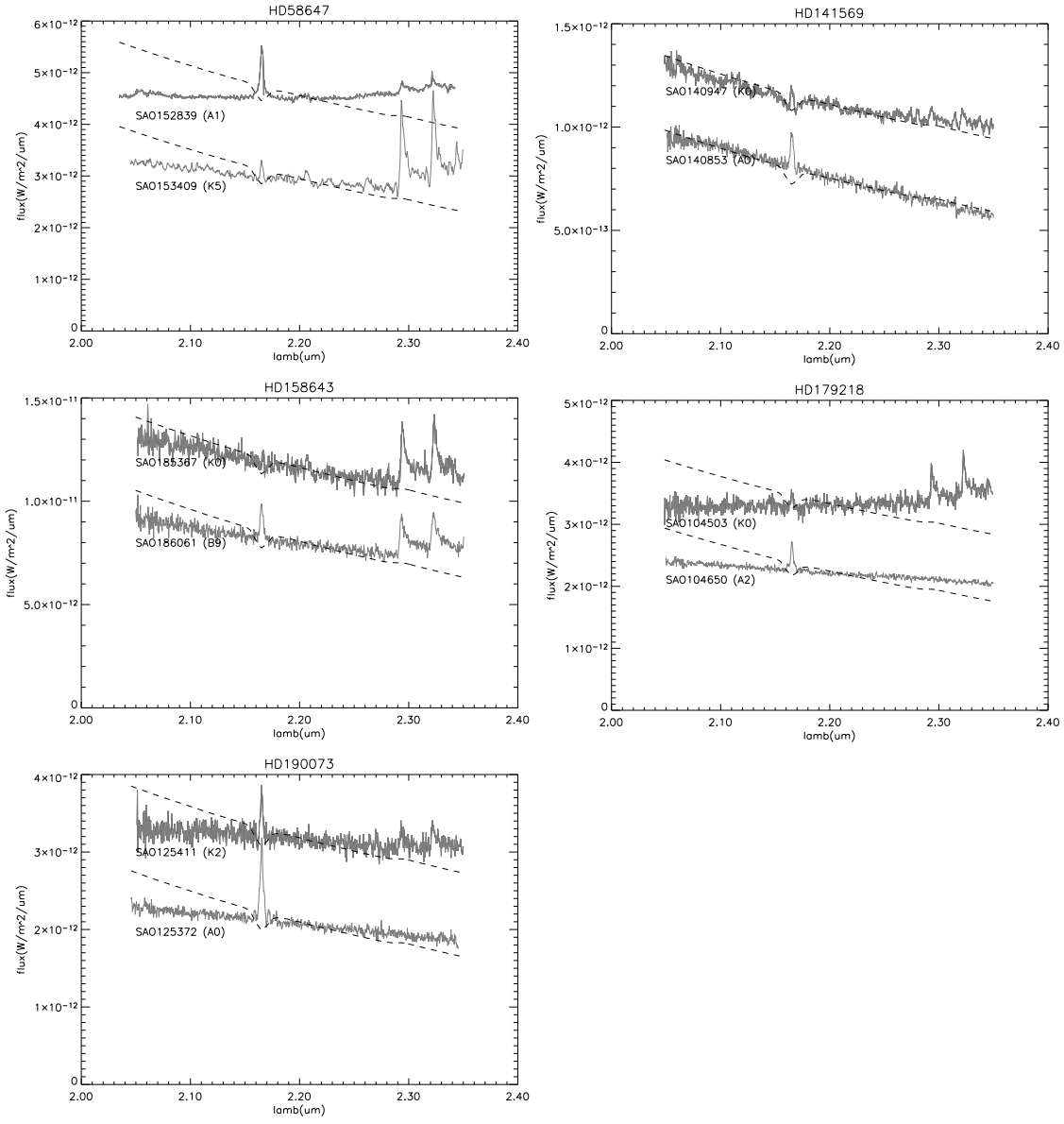

most stars to be flatter than the model spectrum. It is unclear why some spectra have a steeper slope than the model. This, as well as the observation that different reductions of the same star have different overall slopes can be caused by the following: either uncertainty in the spectral type of the calibrator or the undetected presence of extinction and/or an infrared excess in the calibrator spectrum. The spectra show Brγ lines at 2.615μm as well as the first three bandheads of CO overtone emission: the $v = 2 \rightarrow 0$ bandhead at 2.29μm, the $v = 3 \rightarrow 1$ bandhead at 2.32μm and the $v = 4 \rightarrow 2$ bandhead at 2.35μm. The Brγ feature from our source stars is visible in the reductions with K-type calibrators. In spectra with A-type calibrator this feature is contaminated by the Brγ absorption of the calibrator. In a similar way only the CO emission features in spectra with A-type calibrators are reliable, the features seen in the K-type calibrator spectra being caused by CO absorption in relatively the cool atmosphere of the K-type stars. Some spectra show a large double feature around 2.0μm. This feature, as well as the higher noise observed at shortest and longest wavelengths in some spectra, are caused by differences in the observed sky absorption between the calibrator and the program star.

3.3.2 Stellar Parameters

Additional data we obtained about the stars is listed in Table 3.3. Spectral type dependent factors necessary for calculating extinction, luminosity and veiling were obtained from "Astrophysical Quantities" (Cox, 2000). The uncertainties in the distances can be up to 20% depending on the source for the distance.

To calculate the **visible extinction** (A_v) we used the formula from Cox (2000)

$$\frac{A_V}{E_{B-V}} = 3.30 + 0.28\,(B - V)_0 + 0.04\,E_{B-V} \tag{3.7}$$

Table 3.3: Characteristics of surveyed Herbig Ae/Be stars. Type, M_B and M_V are from the Simbad website, M_K is from the 2-MASS survey Skrutskie *et al.* (2006). All distances were calculated from the hipparcos data except the following: The distances for HD34282, HD244604, HD 37258, HD169142 and HD190073 were taken from Acke *et al.* (2005), the distances for HD37357 and HD37411 are from Vieira *et al.* (2003) and the distances for HD35929 and HD36917 were chosen as the distance to Ori OB1.

HD#	Type	T_{eff} (K)	Distance (pc)	M_B	M_V	M_K	A_V	L_* ($L_\odot$)
17081	B7 IV	13000	135	4.12	4.23	4.51	0.07	777
31293	A0 V pe	9520	144	7.18	7.06	4.3	0.46	49.4
31648	A3 pshe+	8720	131	7.9	7.73	5.69	0.3	17.0
34282	A0e	9520	400	10.12	9.85	7.42	0.96	46.1
35929	A5	8200	460	8.52	8.13	6.76	0.8	224
36112	A3e	8720	204	8.54	8.29	5.9	0.57	31.5
244604	A3	8720	336	9.59	9.43	7.21	0.27	22.7
36917	A0 V	9520	460	8.13	8.03	6.4	0.4	194
37258	A2 V	8970	510	9.93	9.77	7.66	0.37	42.6
37357	A0 Ve	9520	320	8.95	8.85	7.24	0.4	44.1
37411	B9 V	10500	230	9.97	9.86	7.55	0.59	13.0
37806	A0 V	9520	880	7.95	7.93	5.77	0.13	610
41511	A psh	-	328	5.15	4.97	1.67	-	-
259431	B6 pe	14000	289	9.03	8.81	5.62	1.21	181
50138	B9	10500	289	6.61	6.58	4.18	0.33	329
56895B	F0 V	7200	-	8.75	8.42	3.56	0.1	0
58647	B9 IV	10500	277	6.85	6.81	5.43	0.36	252
141569	B9.5e	10000	99	6.90	7.00	6.82	-0.2	14.7
142666	A8 V e	7580	116	9.33	8.81	6.04	0.95	8.46
143006	G6/G8	5640	-	10.9	10.2	6.73	-	-
144432	A9V / F0V	7290	252	8.5	8.16	6.14	0.20	35.6
149914	B9.5 IV	10000	165	6.97	6.75	5.74	0.86	136
150193	A1 V e	9230	150	9.37	8.88	5.64	1.56	26.4
158643	B9.5 V e	10000	131	4.81	4.81	4.31	0.13	262
163296	A1 V e	9230	122	6.97	6.87	4.7	0.26	33.6
169142	B9 V e	10500	145	8.41	8.15	6.53	1.09	39.2
179218	B9 e	10500	244	7.7	7.2	5.91	1.88	554
190073	A2 IV pe	8970	320	7.92	7.82	5.78	0.17	84
MWC349	Bpe	-	-	13.0	13.2	3.15	-	-

where $(B-V)_0$ is the expected color difference for that stellar type and

$$E_{B-V} = (B-V) - (B-V)_0$$

is the B-V excess. This formula gives a similar result than the one we derived using our extinction curve, which is very similar to the

$$R_V \equiv \frac{A_V}{E_{B-V}} = 3.10 \tag{3.8}$$

curve by Cardelli *et al.* (1989). We used the former formula, although for our stars the differences are negligible. R_V is a dimensionless parameter introduced by Cardelli *et al.* (1989) which specifies the type of extincion.

Since the derived extinction value for a star depends on the stellar type, the extinction curve and the colors used, it is not uncommon for authors to get different values for the extinction. Calvet *et al.* (2004) discusses variations in extinction values caused by using different extinction curves. They also find that a $R_V = 3.1$ extinction curve is best for IMTTS. Hernández *et al.* (2004) found that a $R_V = 5$ extinction curve fits HAeBe stars best. The choice of extinction curve is important as the extinction determines the luminosity, hence the place of the star in the HR diagram. Calvet *et al.* (2004) also find that for a particular star extinction can vary up to two orders of magnitude as circumstellar material of different densities move in front of the star. They emphasize the need for concurrent observation of color values to determine extinction. The uncertainties in the extinction is about 0.1, depending on the star. However, if other extinction models were more accurate for our sources the values could vary by 0.5 or more.

Our extinction values are similar (within 0.5 magnitudes) to the ones obtained by Valenti *et al.* (2003) using 3000Å and visible colors. But our extinction values are about twice as large than the values measured by Malfait *et al.* (1998). These differences are probably due to the use of different sources for stellar type and

magnitudes. The extinction values we obtained are not correlated with any other properties of the stars we looked at.

To calculate the **stellar luminosity** we used the bolometric correction (BC) in the equation

$$L_*[L_o] = d[pc]^2 \, 10^{\frac{4.74-BC-V+A_V-5}{2.5}} \tag{3.9}$$

where V is the visual magnitude and d the distance. To test this formula we both integrated the total flux of extinction corrected model spectra and the corresponding blackbody spectra. The results agreed within 10%. The uncertainties in the stellar luminosity can be as large as 50% and mostly depends on the uncertainty in the distance.

For most stars the calculated luminosity is similar to or (up to 10 times) above the value for the main sequence at that spectral type. Notable exceptions are:

- HD35929: This star is probably still accreting. It has been classified as a class III star by other authors (Dent *et al.*, 2005; van den Ancker *et al.*, 1998).
- HD259431: The uncertainties in the distance are large. Different distances quoted by different authors would increase the luminosity by up to one order of magnitude.
- HD169142: Other authors (Acke *et al.*, 2005; Grady *et al.*, 2007) have classified this star as an A5 instead of a B9. This correction would move the star to the main sequence (the different A_V would also dim L_* by a factor 2).
- HD37411: We used the photometric distance from Vieira *et al.* (2003). They also indicate that the star could be a part of Ori A group, which would make it 3-7 times brighter, but still to dimmer than a MS-star of that spectral type.
- HD141569: All recent publications we found agree on the distance and spectral type of this star. Nevertheless it is about one order of magnitude dimmer

than a MS-star of the same type. One possibility is that the published spectral type for this star is inaccurate.

3.3.3 Emission Lines

Table 3.4 displays the measured as well as the corrected line fluxes. For HAeBe stars the Brγ line emission from the circumstellar regions is mixed with the veiled Brγ absorption line from the stellar photosphere. The veiling is caused by infrared emission from circumstellar material.

We measured the Brγ **equivalent widths** by fitting a continuum to the spectrum adjacent to the line (we used the $2.135 - 2.155\mu$m and the $2.175 - 2.195\mu$m range for the continuum fit). After subtracting the spectrum from the continuum we integrate the line flux. The equivalent width is equal this integrated flux divided by the fitted continuum flux at 2.165μm. The uncertainty in our measurement is about 1Å. We measured Brγ equivalent widths from all the stars for which we had M or K-type calibrators. We also measured the widths for the stars that were reduced with ATRAN, as the A0-type model used in this package seems to reliably account for the Brγ flux of the calibrator. We checked if we could obtain the Brγ equivalent widths for the remaining stars using

$$\mathrm{EW}_{\mathrm{target}} = \mathrm{EW}_{\mathrm{measured}} + \mathrm{EW}_{\mathrm{model\,of\,calibrator}} \tag{3.10}$$

However we decided not to use this method, as the results vary by several Å from the ones we obtained using the standard procedure. The differences can be explained by the large variation in Brγ in normal stars (Wallace & Hinkle, 1997).

If UV spectra are available, the 2200Å graphite feature allows to differentiate between the **veiling** and the extinction (Valenti *et al.*, 2003). However, this technique depends on the nature of the extinction law. We used the simpler technique

Table 3.4: Observations of lines from our K-band spectra: K_{exc} is the extinction correction to calculate the K-band veiling. The equivalent widths (EW) for the Brγ line are the measured values, the (veiling corrected) photospheric value and the circumstellar line widths. Negative values indicate emission. The circumstellar equivalent widths for sources without measured widths were taken from Garcia Lopez *et al.* (2006). The MgII flux is from Valenti *et al.* (2003). Carbon monoxide (CO) overtone emission is indicated as: no emission (**N**), emission (**Y**) - from outflow (**flow**) - from disk (**disk**) or cold CO emission from a binary (**Bin**). The last columns indicates the status of the dusty disk: first the group as define by Meeus *et al.* (2001) followed by the structure as determined by Malfait *et al.* (1998).

HD#	K_{exc}	EW Brγ_{meas}	EW Brγ_{Phot}	EW Brγ_{CS}	CO	IR-Disk	
		Å	Å	Å		Group	Type
17081	0.0	10.1	8.5	1.6	N		outer
31293	2.4	-3.6	1.4	-5.0	N	I	gap
31648	1.6	-4.6	3.1	-7.7	N	II	gap
34282	1.6	1.9	2.8	-0.9	N	I	Gap
35929	0.3	3.6	10.2	-6.6	N	II	outer
36112	1.7	1.3	2.8	-1.5	N	I	gap
244604	1.8	2.7	2.5	0.2	N	II	gap
36917	1.3	4.9	3.7	1.2	Y-flow		gap
37258	1.6	-	-	-	N		gap
37357	1.3	-	-	-	N		gap
37411	1.9	1.2	1.8	-0.6	N		Gap
37806	2.0	-3.2	1.8	-5.0	N		gap
41511	-	-	-	-	N		Bin
259431	2.5	-6.8	0.8	-7.6	Y		gap
50138	2.2	-9.4	1.4	-10.8	N		gap
56895B	4.1	-	-	-	Y-Bin		Bin
58647	1.2	-0.4	3.6	-4.0	Y-disk		all
141569	0.4	5.5	7.8	-2.3	N	II	Out
142666	1.4	-	-	-2.4	N(Ns)	II	Gap
143006	-	-	-	-	N(Ns)		Gap
144432	1.1	-	-	-5.1	N(Ns)	II	Gap
149914	0.3	-	-	-0.8	N(Ns)		Out?
150193	1.8	-	-	-5.5	N(Ns)	II	gap
158643	0.4	1.8	7.6	-5.8	Y-disk		all
163296	1.9	-	-	-6.9	N(Ns)	II	Gap
169142	0.8	-	-	-9.7	N(Ns)	I	GGap
179218	-0.3	1.3	13.9	-12.6	N	I	Gap
190073	1.8	-5.9	2.5	-8.4	N	II	gap

from Rodgers (2001). The idea is to use the (extinction corrected) V-K color difference for the star and compare it with the difference for that stellar type to obtain the magnitude of the veiling (or excess) in the K-band:

$$K_{exc} = m_V - m_K - (M_v - M_K)_{typ} - A_V \left(1 - \frac{A_K}{A_V}\right) \tag{3.11}$$

where $A_K/A_V = 0.112$ was measured from our extinction law. The type dependent color differences $(M_v - M_K)_{typ}$ were obtained from Cox (2000). We obtained the photospheric equivalent widths from the Kurucz (1992) models and corrected them for veiling using $EW_{phot} = EW_{phot\,only}\, 10^{-\frac{K_{exc}}{2.5}}$ To obtain the circumstellar equivalent width we subtracted the photospheric value from the measured equivalent widths. These widths (EW_{CS}) have uncertainty values similar to the measured values EW_{meas}. However, the uncertainties are larger for stars with large photospheric contribution, especially if the extinction models were inadequate.

Our Brγ values agree within 2Å with the ones measured by Garcia Lopez *et al.* (2006). This allows us to include their values in our survey.

Circumstellar Brγ emission is observed from about 2/3 of our sources. None of the stars show clear circumstellar absorption of this line. However the emission is correlated neither with CO emission, nor the veiling, the spectral type, the stellar luminosity or the disk structure.

Most stars have no CO overtone emission. We identified some of the CO emission as coming from an outflow, a ring or a disk. Our fits to high resolution spectra of the CO overtone emission are discussed in the following chapters.

3.4 Discussion

3.4.1 Brγ Results

The lack of correlation of the CS Brγ with spectral type (see also Figure 3.4) and stellar luminosity confirms that the source for this emission is not directly related to the star. If Brγ emission were primarily due to stellar winds we would expect a correlation with spectral type and/or luminosity, which is not seen. There is also no correlation of the Brγ emission with properties of the disk we list in table 3.4, hence the emission must be independent of the dust or its atmosphere. We take this as confirmation that the Brγ emission is likely related to accretion, winds and/or the gas disk (Calvet *et al.*, 2004). Using our Brγ flux we compare the flux of Brγ photons to the expected flux of high energy UV photons from the star: The number of UV photons is about 8 orders of magnitude smaller than the flux required to sustain a photo ionization region responsible for the Brγ flux we observe. Hence another process like shocks must be responsible for the Brγ emission we observe. Estimates of the mass of emitting gas depend on assumed gas properties but for our objects this mass is smaller than one solar mass by several orders of magnitude. Comparison of stars we reobserved and of the stars in the survey of Garcia Lopez *et al.* (2006) indicates that the Brγ flux does not vary significantly over months or a few years. This may indicate that a steady state process is responsible for the emission.

3.4.2 Accretion Luminosity

Table 3.5 shows L_{acc} calculated using different tracers for accretion. None of the values agree although the values from the MgII and the CIV emission are similar within one order of magnitude. However both of these values of L_{acc} are at least

Table 3.5: List of stellar and accretion luminosities. All luminosities are given in units of $L_\odot$. The stellar luminosity L_* is given as calculated in the last section. The last three columns give L_{acc} as computed using the formulas by Calvet *et al.* (2004) from the Brγ flux and computed from the MgII (2800Å) flux from Valenti *et al.* (2003) and the CIV (1548Å) flux from Valenti *et al.* (2000).

HD#	Type	L_*	L_{acc} Brγ	L_{acc} MgII	L_{acc} CIV
17081	B7 IV	778	-	-	-
31293	A0 V pe	49.4	3.68	0.0000048	-
31648	A3 pshe+	17.0	1.44	0.00010	-
34282	A0e	46.1	0.38	-	-
35929	A5	224	5.01	0.00036	0.00097
36112	A3e	31.4	0.61	0.000018	-
244604	A3	22.7	-	-	-
36917	A0 V	194	-	0.000062	-
37258	A2 V	42.6	-	-	-
37357	A0 V e	44.1	-	0.000036	-
37411	B9 V	13.0	0.09	-	-
37806	A0 V	610	28.45	0.0016	-
259431	B6 pe	181	6.31	0.000020	-
50138	B9	329	28.51	0.000053	-
58647	B9 IV	252	3.86	-	-
141569	B9.5e	14.7	0.11	0.0000025	-
142666	A8 V e	8.46	0.31	0.0000052	0.00021
144432	A9 V / F0V	35.6	2.24	0.00028	0.0054
149914	B9.5 IV	136	0.27	-	-
150193	A1 V e	26.4	1.43	0.000024	-
158643	B9.5 V e	262	3.52	-	-
163296	A1 V e	33.6	2.63	0.000029	-
169142	B9 V e	39.2	1.07	-	-
179218	B9 e	554	5.75	0.0000098	-
190073	A2 IV pe	84	7.26	0.000113	-

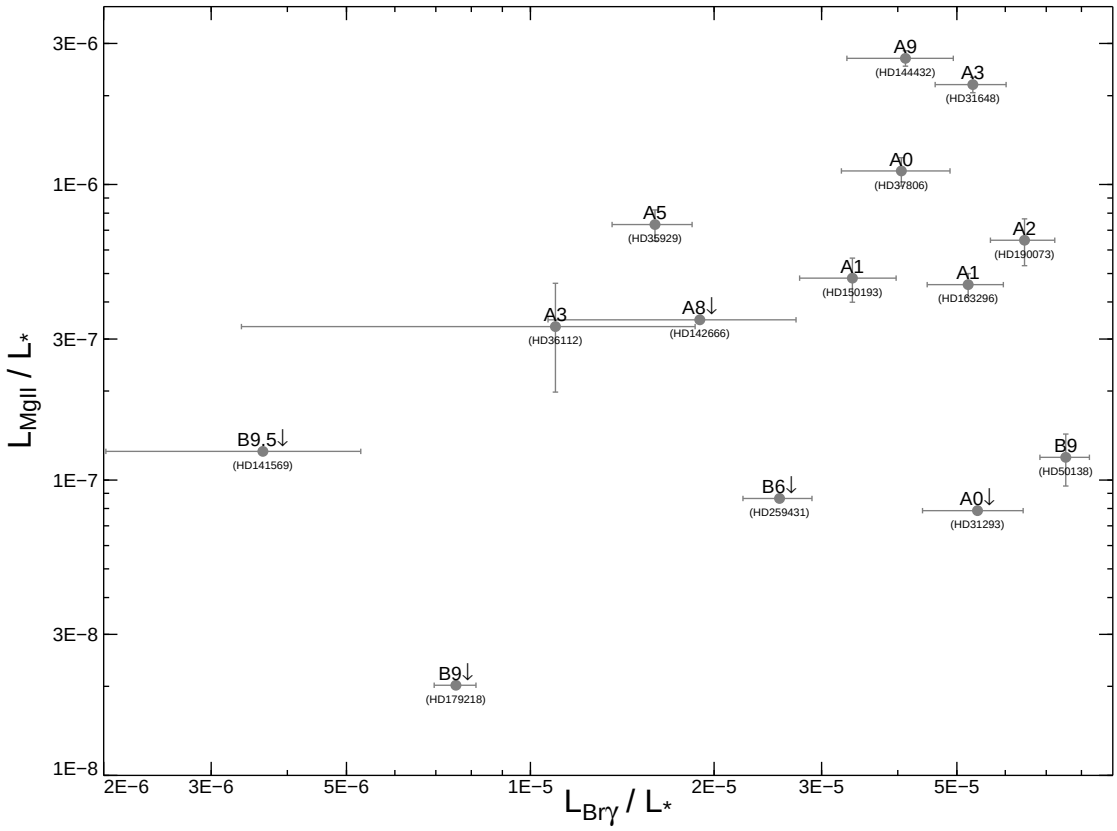

Figure 3.4: Comparison of the Brγ and MgII (2800 Å) luminosity of our stars. Both values are normalized using the corresponding stellar luminosities. The Brγ values are circumstellar values derived from Table 3.4, the MgII fluxes are from Valenti *et al.* (2003). $1-\sigma$ uncertainties are shown and were determined from our EW measurement for the Brγ and from Valenti *et al.* (2003) for the MgII. As the uncertainties were determined under the assumption that the veiling and extinction correction discussed in the previous section are appropriate, the real uncertainties could be larger.

3 orders of magnitude below the estimate of L_{acc} from the Brγ emission. This observation contradicts the relationships determined by Calvet *et al.* (2004) for IMTTS. Normalized Brγ and MgII luminosities are shown in Figure 3.4. The lack of correlation between these two lines supports the observations from the Table. As observed by Valenti *et al.* (2003) stars with colder spectral type can have brighter MgII emission.

There are several uncertainties that could cause these differences: The accretion luminosities used by Calvet *et al.* (2004) to derive Equations 3.3, 3.5 and 3.6 deviate from these relations by as much as a factor 3. This value is larger than the uncertainties of up to 50% expected from the uncertainties in distance and extinction (even if the extinction model is non-optimal). As brightness fluctuations can be expected for some stars our values can be off for the particular time we observed. Furthermore, the spectra used by Valenti *et al.* (2003) are averaged over all available spectra (low and high resolution) but the low-resolution data may be inadequate for measuring the narrow UV emission lines (Carol Grady, personal communication, July 2007). All these uncertainties are probably not larger than two orders of magnitude, hence they can not account for the large differences we observe in our estimates of L_{acc}.

The work of Calvet *et al.* (2004) analyzed IMTTS with strong CIV and MgII emission lines. Their empirical fits were never tested for stars with the much weaker emission lines that were measured from HAeBes by Valenti *et al.* (2000, 2003). The CIV and MgII line to stellar luminosity ratios are several orders of magnitude lower for HAeBe stars than for IMTTSs ($100 - 1000\times$ for the CIV, and $1000 - 50'000\times$ for the MgII). Hence the formulas determined by Calvet *et al.* (2004) may not be applicable to HAeBe stars. Furthermore, all formulas were tested for cooler TTSs (type F and colder). Finally, the lack of MgII and CIV emission from HAeBes

could be caused by a lack of these ionic species relative to TTSs. It not sure how this would happen as even IMTTSs with high UV excesses still show strong MgII and CIV lines.

The relationship between Brγ and L_{acc} was tested over a large range of stellar masses. We also did correct for photospheric Brγ absorption. However it is possible that there are other sources for Brγ emission not present around TTSs.

Using the upper limit to the accretion for HD169142 determined by Grady *et al.* (2007) we find that L_{acc} for that star should be below $0.02L_{\odot}$. This value is much lower than what we measure using Brγ and compatible to the low values determined for other stars using the UV lines. This observation confirms that (at least for this source) the Brγ emission is not caused by accretion but by a different process.

Assuming the real values for L_{acc} are much smaller than the values determined by the Brγ emission, we find that all these values are smaller than typical values measured for IMTTS (Calvet *et al.*, 2004). This is not surprising, as we would expect accretion to be weaker in older HAeBe stars (the evolutionary descendants of IMTTSs). On the other hand the large values of L_{acc} measured using Brγ would imply that the accretion of the presumably older HAeBe stars is similar to the younger IMTTS, a puzzling result. High resolution spectra will help identify the source of the Brγ emission.

3.4.3 CO Overtone Emission

CO overtone emission can be observed in 3 of our 27 (non-binary) targets. This confirms earlier observations by Najita *et al.* (2000) and others that such emission is not common. Hence the more common CO fundamental emission is better to determine the properties of the gas. The CO is not related to the Brγ emission nor

to other disk indicators. Hence the occurrence of CO emission appears independent of the bulk properties of the disk or the accretion onto the star. It may depend on disk geometry. On the timescales of our observations we found that the CO overtone emission are not a transient phenomena as we reobserved some of our targets up to two years apart with no change in CO overtone flux. CO overtone emission requires hot (above 1000K) and dense ($n > 10^{10} cm^{-3}$) gas (Scoville *et al.*, 1980). The lack of CO overtone emission for most of our observed HAeBes indicates that such conditions are not present around these objects. As CO dissociates at a temperature well above 1000K we expect gas with the correct temperatures to be present in the inner disk, closer to the star than the dust sublimation range. But the gas density in these inner regions must be low. As accreting gas must traverse this inner disk our observation implies that either viscosity in this part of the disk causes efficient disk accretion or that only little accretion is present. This last observation supports the relatively low accretion luminosities we measured from the UV line emissions. Our observations don't contradict the presence of massive inner disks for stars hotter than B5 (Monnier *et al.*, 2005) as no such stars are present in our survey. We will present a more thorough analysis of the CO emission in the following chapters.

3.5 Conclusion and Future Work

We find that

- We confirm that Brγ emission is not caused by the stars or the dust disks. It could be caused by star-disk interaction, by stellar winds and/or by hot disk gas.
- The indicators for L_{acc} we tested should be treated with caution. The values

of L_{acc} obtained from the Brγ are more than three orders of magnitude above the ones determined from UV lines. Although there are several uncertainties in our methods large differences remain. The L_{acc} we measure using the Brγ is probably higher than the real value, hence the circumstellar Brγ excess is caused by a process different than accretion.

- To have more precise measurements it would help to take UBV and IR photometry or optical spectra with Balmer lines at the same time as the spectra are taken to determine stellar parameters like extinction and veiling accurately. High resolution spectra and interferometric measurements of the Brγ emission are needed to determine the source of the emission.
- We confirm that CO overtone emission is not common in HAeBe stars though it remains unclear what determines if a certain star has such emission. This observation supports the lack of massive gas disks inside the dust sublimation radius and hence sets upper limits to the amount of gas accretion.
- It would be interesting to look for CO overtone emission from IMTTS which presumably have stronger accretion than HAeBes (as they are younger). Another possible class of targets are YSOs hotter than B5 which presumably have massive inner gas disks (Monnier *et al.*, 2005).
- None of the observed lines show strong variations on the timescales of months to a year.

Chapter 4
Emission from 51 Oph

4.1 Introduction

51 Oph (HD 158643) is a nearby (131 pc) bright (V=4.78) star with a large infrared excess and a rich IR spectrum indicating the presence of a large amount of gas and dust. The evolutionary status of 51 Oph is unclear. Based on visible spectra, Dunkin *et al.* (1997) confirmed earlier results that 51 Oph is a B9.5Ve star. However, using an improved classification system, Gray & Corbally (1998) re-classified 51 Oph as a A0II-IIIe star. Often the star has been classified as a Herbig Ae/Be (HAeBe) star. It has also been proposed that 51 Oph might be accreting from a companion or might be a classical Be star or an evolved star. In order to understand and classify the system a characterization of the distribution and the physical properties of the circumstellar dust and gas is necessary.

In the study of CS disks of HAeBe stars by Malfait *et al.* (1998), 51 Oph is one of two stars which does not fit this suggested sequence for disk evolution. Both stars have small, hot disks close to the star. Malfait et al. raise the possibility that the disks of these stars evolved without forming planets.

ISO spectra of 51 Oph have been re-analyzed by van den Ancker *et al.* (2001). They show a spectrum rich in molecular and atomic gas emission lines. The amount of warm (T = 1000 K) gas is higher than that of any HAeBe star observed by ISO. The 10 μm silicate feature has a strong shoulder that extends to 15 μm. These unusual spectral features motivated van den Ancker *et al.* to question whether 51 Oph is a pre-main sequence object. It could be a highly evolved star, could be accreting material from an evolved companion, or could be shedding mass due to its high rotation velocity ($V \sin i = 270$ km/s), as measured by Dunkin *et al.*

(1997).

Using the same ISO data set, Meeus *et al.* (2001) compared 51 Oph to 13 other HAeBe stars. They confirmed that 51 Oph has more gas than other HAeBe stars, and also found that it has less cold dust. Roberge *et al.* (2002) observed UV line emission, finding evidence for abundant in-fall of gas, and concluded that 51 Oph is a young example of a $\beta -$ Pic type star. This conclusion agrees with the analysis of ISO spectra by Waelkens *et al.* (1996), who reported that the dust around 51 Oph is similar to cometary dust. Using mid-IR interferometry, the extent of the dust disk was investigated by Leinert *et al.* (2004). They found that the disk of 51 Oph is much smaller than the disk of most HAeBe stars, thus confirming the conclusions of Malfait *et al.* (1998).

Thi *et al.* (2005) have observed CO overtone emission at 2.3 μm from 51 Oph. Their observations indicate large amounts of hot CO gas in a Keplerian orbit. Their model fits indicate that the line of sight velocity at the inner edge of the disk is 153 km/s with a temperature of 2850 K and the outside of the hot CO disk moves at 100 km/s with a temperature of 1500 K. Other findings are that the disk is seen nearly edge on ($i = 88^o$) and that the mass of CO responsible for the emission is (0.17 to 2.5)$\times 10^{-10}\,M_\odot$. Thi et al. conclude that 51 Oph has a large amount of hot (several 1000 K) gas inside the dust sublimation radius. Assuming a stellar luminosity of 260 $L_\odot$ (Thi *et al.*, 2005), this boundary lies at a distance of about 0.64 AU.

Here we present high resolution spectra of several CO overtone bandheads of 51 Oph. These measurements allow us to investigate the innermost regions of the disk inside the dust sublimation radius, as well as the interactions between the star and the disk. We determine physical characteristics of the CO gas in the disk by using a detailed disk model. This work includes the first fit of the emission

line width, which has a significant effect on the other fitted parameters. We also include an analysis of uncertainties in the observational data and in the modeled parameters.

4.2 Observations

We obtained K-band spectra in June 2003 using the NIRSPEC echelle spectrograph (McLean *et al.*, 1998) at the W. M. Keck Observatory on Mauna Kea, Hawaii. The spectral resolving power of our spectra, as determined by lamp lines and bright night sky lines, was $\lambda/\Delta\lambda = 25,000$ at $2.3\,\mu$m. The spectrum of 51 Oph resulted from 8 coadded integrations of 5 seconds each, nodding along the slit with a two position nod. We observed the A0V standard star HD155379 before the program observations.

For **data reduction**, we used the REDSPEC software written for NIRSPEC data (McLean *et al.*, 2003). To calibrate the data, we took flat and dark images and lamp spectra throughout the night. REDSPEC essentially reduced the data as discussed in Chapter 2. We did have to spectrally rectified the images to render spectral lines orthogonal to the dispersion direction and parallel to the array columns for later extraction of the spectral data. Spatial and spectral rectification parameters were determined using the raw data and the lamp spectra. We extracted the spectra using direct summation of rows. For the long wavelength order ($2.435 - 2.465\mu$m) we also had to shift the atmospheric spectrum slightly ($\sim 100\,$m/s) to optimize the atmospheric subtraction. For some spectral orders, the spectral rectification resulted in a poor wavelength calibration. This offset, which could be as high as $0.001\,\mu$m (or 130km/s), was due to a lack of lamp lines for certain spectral orders. We re-calibrated the affected orders by manually comparing telluric absorption features with a synthetic spectrum produced by the

ATRAN program (Lord, 1992). This manual recalibration is accurate to about $2 \times 10^{-5}\,\mu$m. We checked the final spectrum for fringing using the FFT analysis provided by REDSPEC, but no fringing pattern was found.

To **subtract** the **continuum** and flux calibrate the spectrum, we reduced all spectral orders to create a composite spectrum from $2.1\,\mu$m to $2.5\,\mu$m (see Figure 4.1). We expect the continuum to be a combination of the stellar spectrum and the short wavelength part of the thermal emission from circumstellar dust. We calculated this emission using the dust emission model of Waters *et al.* (1988). This model considers uniform dust grains in thermal equilibrium with the stellar radiation field. The model parameters were taken from Malfait *et al.* (1998). The continuum model was matched with our data and subtracted to obtain the spectrum of the CO emission. To calibrate the absolute flux, we used the 2MASS K magnitude of our target star. This absolute flux calibration directly affects the measured mass of the CO, but only has a minor effect on our other fitted parameters.

We determined the **signal-to-noise** of the spectrum by analyzing the difference between the data from the AB and BA nods. For both the source and the calibrator, the random flux uncertainties seem to be independent of flux, with S/N above 100 and often as high as 200. These values were used to determine the flux uncertainties in the final reduced spectra.

4.3 Results

Here we present our K-band spectra and describe our model to fit the CO emission of a gaseous disk orbiting the star. The entire reduced spectrum is shown in Figure 4.1. The spectrum of 51 Oph shows no features shortward of 2.29μm. The Brγ line of neutral hydrogen at $2.165\,\mu$m in the high-resolution spectrum is entirely due

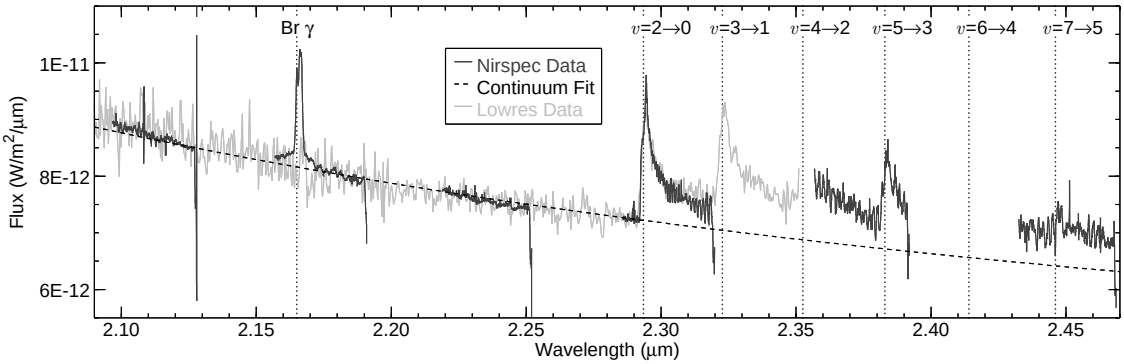

Figure 4.1: Reduced NIRSPEC spectrum from 51 Oph. The data segments are from the different orders of the spectrograph, order 36 on the left to order 31 on the right. The dashed line represents the continuum fit. Important spectral features are indicated by vertical dotted lines. Brγ emission is artificially induced by using a standard that has Brγ absorption. The low-resolution spectrum discussed in the previous chapter is shown in light gray and was obtained in September 2004 at Palomar Mountain. The low-resolution spectrum shortward of 2.20 μm was divided by the K-type calibrator, while the longer wavelength spectrum was divided by the A-type calibrator (hence the change in S/N).

to Brγ absorption from the calibrator star and is not visible in the low-resolution spectrum. We also see weak H_2O features at 2.290 μm (Figure 4.2).

The high resolution spectra and the fits are presented in Figure 4.2. We fitted all wavelength regions simultaneously and also fitted each region individually. These individual fits were done to learn more about the excitation temperatures of individual vibrational bands, and are of better quality than the full fit. All fitted and derived parameters are listed in Table 4.1.

We first computed the average maximum projected velocity without using the model: The shoulder shortward of the bandhead at 2.295 μm is a characteristic of CO emission in a rotating Keplerian disk or ring (Carr *et al.*, 1993). Both, the distance from the shoulder to the bandhead and the interference pattern on the long wavelength side of the bandhead allow measuring this projected velocity (see Najita *et al.* (2000) for a more detailed discussion). Both methods agree that 130 km/s is close to the maximum projected velocity for the emitting gas at a

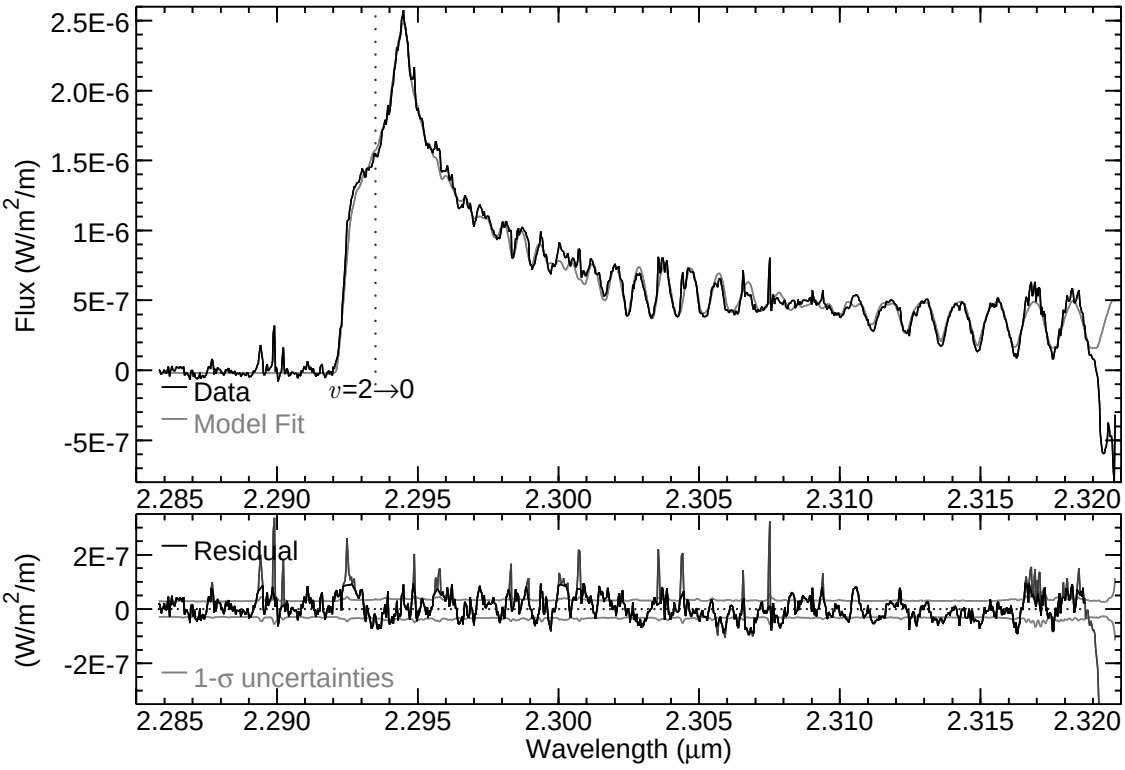

Figure 4.2: Continuum subtracted NIRSPEC spectra of HD158643 with model fits. The wavelength is shown in μm and the intensity is shown in Watts/m^2/m. The residual between the data and the fit is shown in the bottom plots, along with the statistical error. The rest wavelengths of the bandheads are indicated by vertical dotted lines.

Figure 4.2 (continued)

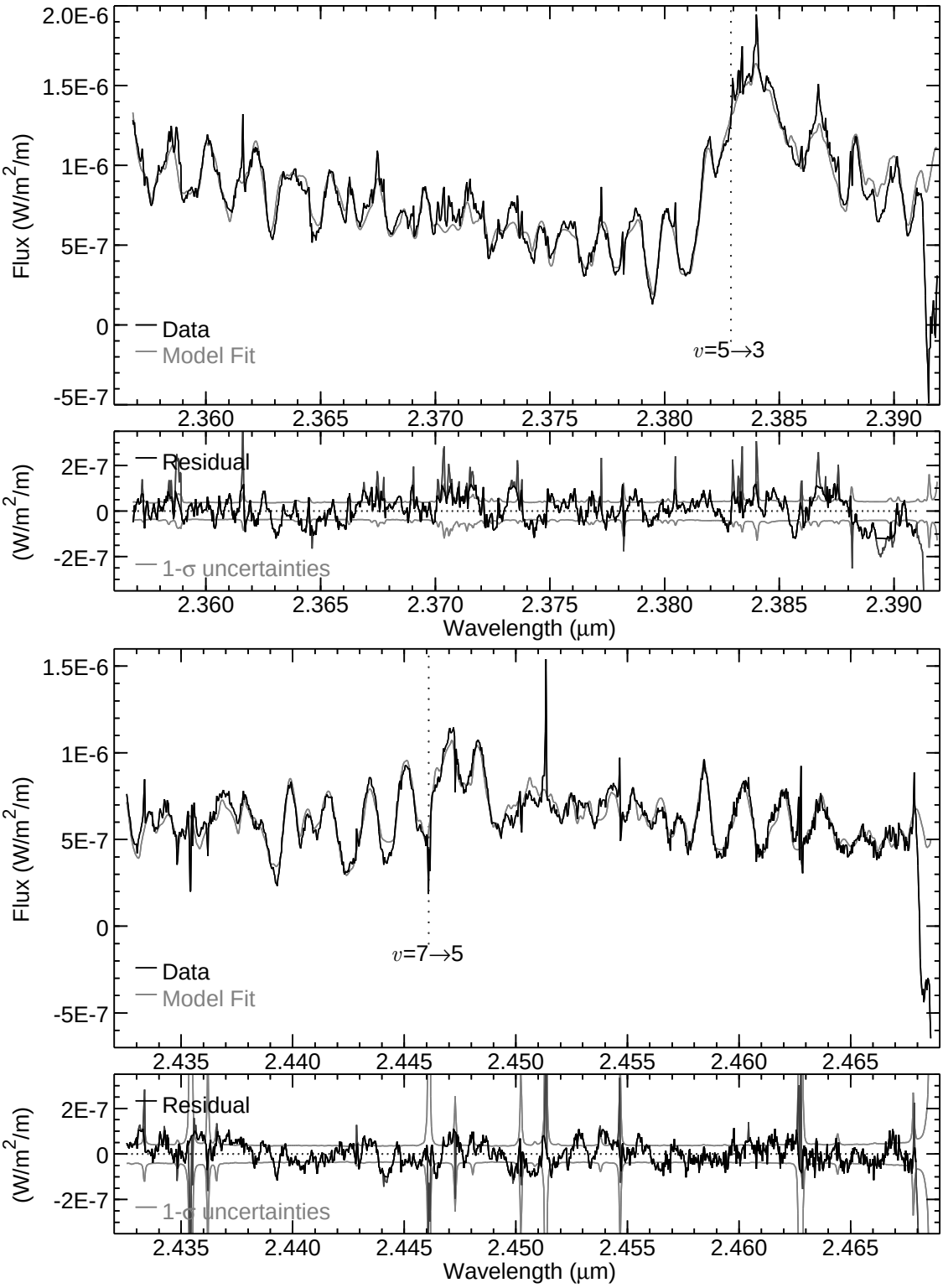

flux-averaged distance from the star.

Both ring and disk models described in Chapter 2 produce fits that are qualitatively acceptable. However the disk model is *quantitatively* a better fit. The errors are minimized and small spectral features are fit more accurately. The disk fits provide overall χ^2 values of about 2/3 of the ring fits. This indicates that most of the gas is probably in a disk of finite width instead of a vanishingly narrow region in orbital radius. Thus we are confident that the CO emission does not originate from an inner disk wall.

Using an optically thick disk model qualitatively improves the fit, especially for the 2.285-2.315μm region. The χ^2 also improves to about 2/3 of the optically thin values.

Analysis of the fitting results show that about 80% of the flux comes from the inner half of the disk, while the outer quarter of the disk contributes less than 5% of the flux. In the inner region of the disk, the maximum optical depth of the lines is between $\tau = 3$ and $\tau = 5$, which puts the emission at modest optical depth. Depending on γ, τ increases or decreases for the outer regions of the disk.

All fits show good agreement with the data in wavelength: The maxima and minima in the fit and the data coincide in wavelength. The residuals between the fits and the data are plotted at the bottom of each spectrum. Large deviations are mostly due to emission lines (water emission at 2.29μm) and bad sky subtraction. Regions with deep atmospheric absorption can be identified by large uncertainties in the residual plots. We neutralized such deviations by ignoring data points where the difference between the data and the fit is larger than 3σ when evaluating χ^2. The residuals are somewhat larger than the errors in the data and do not appear to be random noise. For a good fit, the values of χ^2 should be about 1 for each spectral range. As our χ^2 values are sensitive to the limits for data point exclusion, no clear

statement about the quality of the fit can be made. Our residuals are comparable to the differences found by other authors (Thi *et al.*, 2005).

All fits show some minima and maxima where there is disagreement in the flux. No consistent differences between the fit and the data can be identified. The long wavelength end of the spectrum, where the signal drops, was ignored for each fit. The best fit is in the $2.285 - 2.315\mu$m range. Both RMS residuals and χ^2 are smallest for this fit, and the match looks best upon visual inspection. One large region where the fit is bad, is around 2.3895μm, where the data is several σ below the fit.

Analysis of the parameter correlations in the error plots reveals that both N_i and β, as well as T_i and γ, are positively correlated. These dependencies indicate the conservation of average temperatures and column density by the fitting, further indicate the reliability of our procedures. As expected, Ω usually decreases with an increase in temperature, and therefore emitted flux. The negative correlation between β and γ can be explained as follows: an increase in γ will increase temperature and therefore brighten the inner regions of the disk, while the decrease in β will lower the average column density in the same region, counteracting the brightness increase.

The model fitting can be tested by analyzing the Doppler and flux offsets (V_{off} and $flux_{off}$). The Doppler offsets (V_{off}) for the three wavelength regions are similar, and are consistent with the measured errors, which are larger than the $0.02\,\mu$m or 2.5 km/s uncertainties in the wavelength calibration. On the dates we observed the radial velocity of the observer relative to the Sun was negligible, hence we measure a blueshift of 18 ± 4km/s. This is somewhat larger than the published radial velocity of 12km/s for the star (Evans, 1967), but similar to the velocity of the Ca II K line of about 16km/s measured by Hempel & Schmitt (2003). The fitted flux

Table 4.1: Fitted values from the disk model. Given are $1-\sigma$ uncertainties. The uncertainties of the derived values ($V_{p,o}$, T_o, n_o, $r_{i\,min}$, $M_{*\,min}$) are estimated from the uncertainties of fitted values. The χ^2 values are per degree of freedom and were computed ignoring points with more than 3σ deviation (4σ for all spectrum).

Range	(μm)	2.285-2.315	2.360-2.390	2.435-2.465	All spectra
V_{off}	(km/s)	17 ± 4	19 ± 4	17 ± 4	18 ± 3
$flux_{off}$	$(\times 10^{-14} \frac{W}{m^2\,\mu m})$	-1.71 ± 0.23	1.08 ± 0.8	10.32 ± 0.7	0.79 ± 0.25
$V_{p,i}$	(km/s)	162.9 ± 0.6	159.8 ± 0.5	161.0 ± 0.7	161.1 ± 0.6
$V_{p,o}$	(km/s)	80.2 ± 1.9	79.8 ± 1.1	88.6 ± 2.0	78.9 ± 0.6
r_o/r_i		4.12 ± 0.17	4.00 ± 0.11	3.30 ± 0.15	4.17 ± 0.06
Ω	$(\times 10^{-16}$ sterrad)	1.05 ± 0.09	1.43 ± 0.14	1.39 ± 0.2	1.37 ± 0.07
$M_{*\,min}$	($M_\odot$)	2.18 ± 0.15	2.58 ± 0.15	3.1 ± 0.3	2.41 ± 0.07
T_i	(K)	5010 ± 200	3390 ± 60	3330 ± 50	4020 ± 40
T_o	(K)	810 ± 60	1400 ± 100	1040 ± 70	704 ± 18
γ		1.287 ± 0.020	0.64 ± 0.05	0.97 ± 0.04	1.221 ± 0.012
N_i	$\left(\times 10^{20} \frac{1}{cm^2}\right)$	4.2 ± 0.3	12.9 ± 1.0	10.5 ± 1.5	3.09 ± 0.13
N_o	$\left(\times 10^{20} \frac{1}{cm^2}\right)$	24 ± 5	0.28 ± 0.08	4.4 ± 2.2	590 ± 170
β		-1.23 ± 0.22	2.76 ± 0.20	0.7 ± 0.4	-3.68 ± 0.15
$V_{g,emm}$	(km/s)	3.48 ± 0.09	4.57 ± 0.17	2.95 ± 0.25	3.96 ± 0.06
M_{CO}	$(\times 10^{-5} M_{Earth})$	3.8	4.4	6.5	2.5
χ^2		1.3939	1.5309	1.4663	2.4742

offset ($flux_{off}$) is small compared to the signal for all spectral ranges, indicating that our background model is adequate. The flux offset and uncertainties increase towards longer wavelengths, which is not surprising, since we fitted the background model to the part of the spectrum shortward of 2.30μm. We therefore expect the background model to be less reliable at longer wavelengths. As a different background model would change the slope of the spectrum, it would also affect the values of the fitted temperatures and column densities. We do not expect these changes to be much larger than our uncertainties.

The fit for the entire spectrum is worse than the fits for the individual spectral ranges. To avoid excluding large parts of the data when calculating χ^2, we needed to raise the exclusion interval to $\pm 4\sigma$. Hence the χ^2 value is larger and larger spikes in the data have a stronger influence on the fitted parameters. These problems make it clear that a more physically accurate model is needed to fit the entire

spectrum.

4.4 Discussion

The $v = 2 \rightarrow 0$ R-branch transitions are responsible for all emission seen in the range from $2.285 - 2.315\,\mu$m. The $v = 5 \rightarrow 3$ bandhead is visible in the $2.360-2.390\,\mu$m range. Lines from the $v = 2 \rightarrow 0$ P-branch and from the $v = 4 \rightarrow 2$ R-branch are present throughout this region of the spectrum. In the low temperature outer disk regions, the $v = 2 \rightarrow 0$ lines become more important. In the $2.435 - 2.465\,\mu$m spectral range, most of the flux from the brighter inner regions of the disk comes from a few strong lines of the P branches of the $v = 2 \rightarrow 0$, $3 \rightarrow 1$ and $4 \rightarrow 2$ transitions, as well as the weaker but more numerous lines from the $v = 7 \rightarrow 5$ bandhead and $v = 6 \rightarrow 4$ R-branch transitions. Although the strong lines are optically thick ($\tau \sim 4$), most emission is close to being optically thin. Hence the spectral regions sample different combinations of vibrational transitions, with the short wavelength region containing only one vibrational transition. In general, it seems that the fitted values for the 2.30μm wavelength region are most reliable since only one vibrational transition is involved and the background fit is most reliable in that range.

At the inner edge, the **projected velocities** ($V_{p,i}$) are consistent within the measured error bars for all spectral regions. As these regions sample different vibrational transitions, this finding indicates a common inner edge of the emission from the different transitions. The fits confirm the average maximum projected velocities estimated earlier in this chapter. The values of the ratio of the outer to the inner disk radius ($^{r_o}/_{r_i}$) are consistently much larger than unity, confirming that we are observing an emitting disk, not a narrow ring. As these ratios are determined by the less luminous outer regions of the disk, the low uncertainties

are somewhat of a surprise. Assuming $i = 90^o$ and using $M_* = 3.8\,M_\odot$ as used by Thi *et al.* (2005), our projected velocities indicate that the inner disk radius must be at 0.15 AU and the outer radius at 0.53 AU. If the inclination were smaller, the disk would be closer to the star. The proximity to the star also makes it unlikely that the gas we observe forms an atmosphere on top of a colder dust disk since dust would sublimate at these distances from the star (the dust sublimation distance is approximately 0.64 AU). Although a massive dust disk could self-shield against sublimation, the low IR continuum fluxes argue against such a massive disk (Malfait *et al.*, 1998). Only our inner edge radii are in agreement with the values obtained by Thi *et al.* (2005).

The values of the **projected solid angle** Ω are consistent among the orders to within our estimated uncertainties. $\Omega = 1.4 \times 10^{-16}$ corresponds to an area of about $0.11 AU^2$ at the 131 pc distance of 51 Oph. Such a small projected surface area is only possible with the above radii if we see a geometrically thin disk close to edge-on. (A $r_i = 0.15AU$, $r_o = 0.53AU$ disk has a face-on surface area of $0.81AU^2$.)

Combining Equation 2.10 with Kepler's third law, we find that the mass of the star can be expressed as

$$M_* = \sqrt{\frac{\Omega}{\pi(\frac{r_o}{r_i}^2 - 1)}} \frac{V_{p,i}^2\, d}{G} \frac{1}{\sin^2 i \sqrt{\cos i}} \tag{4.1}$$

which has a minimum at $i = 63^o$, thus giving a minimal estimate for the mass of the star ($M_{*\,min}$). Although the spread in the results is large, the mass quoted by Thi *et al.* (2005) is possible.

Using $M_{*\,min} = 2.2\,M_\odot$ in the $M_*(i)$ curve from Equation 4.1 and assuming that the mass of the star is above $3.8\,M_\odot$ restricts the possible range of inclinations to smaller than 36^o or larger than 83^o (angles in between would imply $M_* < 3.8\,M_\odot$). These angles correspond to inner radii smaller than 0.045 or larger than 0.12 AU, (using $V_{p,i}$).

It has been suggested by Thi *et al.* (2005) that the disk is edge on, which corresponds to $i > 83^o$. With this inclination, the thickness of the disk is limited by Ω and the the disk has to be geometrically thin ($Z/R < 0.1$ or $Z/R < 0.03$ for the inclination found by Thi *et al.* (2005)). We estimate the thickness of the disk to be Z/R=0.04 (see later paragraph), thus a disk with an inclination $i > 88^o$ is unlikely. In the edge-on case, the expected blackbody temperatures at 0.12 AU would be about 3300 K (using $L = 290 L_\odot$). As the dissociation temperature of CO is around 5000 K, other factors like UV dissociation would have to influence the radius of the inner disk edge. If $i < 36^o$, the inner disk edge would be at 0.05AU, which implies a temperature around 5400K, and might still be possible if CO could survive closer to the star than given by the local blackbody temperature. An inclination much smaller than $i < 36^o$ is unlikely, since this would imply that the inner disk edge is even closer to the star and hence even warmer. The co-rotation radius for different inclinations can be calculated by using the effective temperature and stellar luminosity from Chapter 3 with $V \sin i$ of the star from Dunkin *et al.* (1997). For $i = 90^o$ this radius is 0.031AU and it is 0.022AU for $i = 36^o$. These radii do not contradict our values above and indicate that the inner edge of the CO emitting region is defined by CO dissociation instead of being the inner disk edge. The fitted temperature (discussed in detail below) affects all these values since warmer gas requires less surface area for a certain emitted flux. However, we can consider the values from the $2.285 - 2.315 \mu$m spectral range as reliable as this fit is only affected by one vibrational transition. .

The fitted inner disk **excitation temperatures** are similar for the 2.37μm and the 2.45μm wavelength ranges and higher for the 2.30μm range. All these values are below the dissociation temperature for CO at 5000K. The temperature exponent γ varies significantly, causing the outer edge temperature to vary as well.

The fitted value of the temperature exponent γ will be mostly influenced by the brighter regions of the inner disk. Hence the temperature distribution in the outer parts of the CO overtone emitting disk may contribute little to γ. Therefore, we expect the real uncertainties in the outer edge temperature to be somewhat larger than reported. Nevertheless, the low outer edge temperatures are surprising. The temperatures are consistently below the dust sublimation temperature of 1400K, whereas the outer radius is inside the dust sublimation radius of 0.64 AU, even if the disk is seen edge-on. These low temperatures could be explained by self-shielding of the disk from stellar radiation.

Our model was written assuming that the gas is in LTE. At low gas density the different vibrational levels have different excitation temperatures (Najita *et al.*, 1996b). We therefore expect to see different results for the fitted temperatures for the different spectral ranges. The 2.30 μm wavelength range is not affected, as the emission is caused by the $v = 2 \rightarrow 0$ transition only. The quality of the fit (measured in χ^2) is best in the 2.30μm wavelength range. We think these values for excitation temperature of the $v = 2 \rightarrow 0$ transition are quite reliable. The fitted temperatures for the 2.37 μm and 2.45 μm wavelength ranges reflect the population distribution among the vibrational levels as well as a mixture of the excitation temperatures for the different vibrational levels. The lower temperature of these wavelength ranges indicates a lower population of the higher vibrational levels compared to 5000K LTE in the inner disk regions. It is also possible that the fitted temperatures indicate lower excitation temperatures for the rotational levels of the higher vibrational levels. This is unlikely, as the population of the rotational levels within the vibrational levels should be similar because rotational levels thermalize at low densities (Scoville *et al.*, 1980). However, no precise measure for the excitation temperature of these higher levels is possible. The flux weighted aver-

age temperatures are similar: 3050K, 2710K and 2530K for the three wavelength regions (increasing wavelength). As higher vibrational levels are present at longer wavelengths, this supports above findings that indicate that high vibrational levels are less excited compared to the LTE case, and that higher vibrational levels may have a lower excitation temperature.

The fits indicate that the falloff in excitation temperature for the $v = 2 \rightarrow 0$ transition is steeper than the value of 0.75 expected from the constant viscosity disk or the flat irradiated disk model (Hartmann, 2001) (or 0.5 for optically thin dust). This observation could be explained by direct excitation of the $v = 2$ levels in the inner regions by line absorption of stellar radiation. Another explanation could be that the gas close to the star is heated by additional effects like a strong stellar wind, or by interaction of the gas with the star's magnetosphere. Heating by magnetic fields may be less likely since the absence of Brγ emission from 51 Oph could indicate a lack of active accretion along magnetic field lines (Najita *et al.*, 1996a). Such excitation of the inner regions of the disk would support non thermal dissociation of CO for the i $> 83^{o}$ case. It is also possible that the inner disk edge gets the additional heating from direct starlight, but the gas density could be too low to populate higher vibrational levels. The temperature fits for both longer wavelength regions are more in line with current disk models. If i $> 83^{o}$ the temperatures of both of these fits roughly follows the expected radiative equilibrium temperature. This would indicate that the relative population of vibrational levels follows this temperature curve.

The excitation of the $v = 2$ level above LTE is confirmed when extending the fits for the spectral regions to the entire spectrum: The extensions of the fits for the 2.375μm and the 2.450μm regions fit each other. However they predict a lower flux for the 2.300μm region. In turn the extension of the 2.300μm fit predicts a higher

flux for the $5 \rightarrow 3$ and $7 \rightarrow 5$ bandheads (hence warmer excitation temperature).

Extending the fit for the 2.30 μm wavelength range to the full spectrum succeeds at fitting the continuum parts of the spectrum, but has too much flux for the $5 \rightarrow 3$ and $7 \rightarrow 5$ bandheads: This difference is expected, as the higher temperatures of the 2.30 μm fit strengthen these bandheads. On the other hand, extension of the other fits to the entire wavelength range shows that the fits for both longer wavelength ranges fit each other, but the $J < 50$ lines longward of the $v = 2 \rightarrow 0$ bandhead are stronger in these fits than in the measured spectrum. This last observation can be explained by the lower temperature of these fits that weaken the bandhead relative to the other lines for the $v = 2 \rightarrow 0$ transition.

We consistently fit higher inner disk temperatures than the values fitted by Thi *et al.* (2005) for the 2.30μm wavelength range. This difference may be caused by a different treatment of the background continuum flux.

The **optical depth** is small (< 1 for most of the spectrum) and approximately constant for the inner regions of the disk, across all wavelength ranges. This depth is caused by the emission line width $V_{g,emm}$ and the column density. The column density is mostly determined by the requirements for the optical depth and total flux, as shown by an anticorrelation between inner edge temperature (T_i), column density (N_i) and projected area (Ω). Despite the large variations in N_i and β, the flux weighted averaged column densities are similar for all spectral ranges: 7.8, 6.5 and 8.5 $\times 10^{20} cm^{-2}$. Due to large uncertainties, we are unable to determine reliably how the column density changes with radius. The increase in column density for the 2.30μm wavelength range causes an increase in flux with radius at the inner edge of the disk before the flux falls outside $r = 1.1\, r_i$. Hence, a model with an initial increase in column density at the inner disk edge may be necessary. Due to the large variations in column density with radius, we decided to list the masses

of CO which represent the mass of the gas that causes the 70% of the observed line emission. Using a H/CO ratio of 3000, the total mass of the inner disk is a fraction of $M_{\oplus}$, making the disk very light. Our values for the mass agree with the values obtained by Thi *et al.* (2005).

The **emission line widths** $V_{g,emm}$ are roughly similar across all spectral ranges. Like the column density this parameter is determined by the constraints on the optical depth. Although $V_{g,emm}$ probably changes with distance from the star, we choose to keep it fixed. We made this decisions for two reasons: first, we found large error bars in the parameter (N(r)) related to $V_{g,emm}$ and second, to vary $V_{g,emm}$ with distance from the star would have multiplied the computation time of our spectra. It is interesting to note the low uncertainty in the emission line width for the 2.30μm wavelength range. It is possible that this fit is better constrained because only one vibrational transition is involved. The average value of about 3.5km/s is larger than the thermal broadening expected for CO at the measured temperatures (about 1.5 km/s), but is similar to the thermal excitation expected for molecular hydrogen. Assuming turbulence and thermal broadening are the main contributors to the emission line width, the calculated typical turbulent velocity in the disk is about 3 km/s, which is well below the speed of sound (5 km/s) in hot, low density gas.

Another contribution to the emission line width comes from the shear within the optical column discussed in section 2.2.4. It is unclear what effect this shear has on our measured emission line width. Using the disk temperature and the stellar mass of 3.8 $M_{\odot}$ we can estimate the expected scale height in the disk (see Herter *et al.* (1979)). The Z/R thus obtained is 0.04 using our value for the flux averaged radius for the edge on disk (i = 90°). The value will be smaller for smaller inclinations (0.025 for 36°). Averaging Equation 2.13 and using these Z/R values

allows us to calculate the average velocity width within the optical column for our disk. In case i = 36° the expected widening is 1.9km/s, which would imply that this type of widening accounts for a large part of the measured value of $V_{g,emm}$ with thermal broadening and turbulence accounting for the rest. The average velocity width within the optical column for the i = 83° case is 21 km/s. This assumes that our slab model that determined Equation 2.14 applies to the more general disk case. Even if we assume large errors in our model assumptions this value is large compared to our measured $V_{g,emm}$. Hence in the high inclination seems less plausible. If the widening were indeed 21km/s, we would expect the decoherence between gas within the optical column to be considerable. A consequence would be that the real column density may be up to 6 times larger than our quoted N_{col} and that the real value for the projected solid angle is smaller than our value Ω by the same factor. A final argument against the i = 83° case is that in this case Z/R is similar to cos i. As our models have shown, such a geometry would not cause the concave curve between the shoulder and the bandhead maximum which is observed in our spectra.

An improved model will help create a more physically detailed picture of the CO emission. One way to improve our fit is the use of different excitation temperatures for different vibrational levels, as suggested by Najita *et al.* (1996b). Another improvement would be to allow for the gas to thin out towards the inner edge of the disk in order to obtain a more accurate radius distribution of the column density. A third possible improvement would be to use ISO data to constrain the background emission from the star and from hot dust at the longer wavelength ranges.

4.5 Conclusion

We have presented spectra of the hot gas in the innermost regions of the disk around the young massive star 51 Oph. We confirm that CO gas is orbiting the star in a low-mass disk at a small distance.

We found the following results:

- The projected size of the disk limits the mass of the star to $M_* > 2.2\,M_\odot$. Assuming a star of $4\,M_\odot$ limits the inclination of the system to $i > 83^o$ or $i < 36^o$. Our measured emission line width and inferred geometry supports the second case, whereas gas temperature estimates make the first case more likely.
- The excitation temperature for the level populations of the vibrational bands is about 3400K at the inner disk edge and changes with radius as expected from current disk models. These temperatures are consistent with the gas being in radiative thermal equilibrium for the $i > 83^o$ case.
- The excitation temperature for the rotational levels of the $v = 2 \rightarrow 0$ transition however, is about 5000K at the inner disk edge and changes with radius$^{-1.3}$. This observation requires additional heating by stellar radiation, winds or magnetic fields of the high rotational, low vibrational levels in the inner disk.
- Turbulence and differential rotation contribute between 2 and 3 km/s to the emission line width.
- We confirm earlier findings about the location of the inner edge of the emitting region.
- Strong lines are optically thick but most lines are optically thin.

- The emission is caused by about $10^{-4}\,M_{Earth}$ of CO gas at an average excitation temperature of 2700K and column density of $7.5 \times 10^{20} cm^{-2}$.
- We measured a blueshift of 18 km/s for the line of sight motion of the star.

This work clearly demonstrates the advantage of observing multiple bandheads. A more detailed model will allow better understanding of the excitation of the gas.

Chapter 5
High-resolution spectra from HD36917 and HD58647

5.1 Introduction

We were able to obtain high resolution CO spectra of two other program stars, albeit at reduced signal to noise, since observations were done at the IRTF telescope rather than at Keck.

5.1.1 HD36917

The star HD36917 (also called V372 Ori) is a A0V star, located in the Orion OB1 star association at a distance of approximately 460pc. The star has a luminosity of about 190$L_\odot$ and weak circumstellar Brγ absorption (see chapter 3). Its infrared spectrum was interpreted as a disk with a hot and cold component by Malfait *et al.* (1998) but looks similar to the Group II stars according to the Meeus *et al.* (2001) classification, implying a non-flared disk. The star's rotational $V \sin i$ is 130km/s (Wolff *et al.*, 2004). The UV spectrum reduced by Valenti *et al.* (2000, 2003) shows no strong emission lines and little variation in UV flux. The spectrum also shows a broad 2200Å absorption feature. Observations of visible lines by Manoj *et al.* (2002) show low line fluxes from photospheric lines which is uncharacteristic for HAeBe stars. They also confirm that HD36917 is kinematically connected to OB1 and conclude that the star is possibly at an intermediate stage between a HAeBe and a Vega-type star.

5.1.2 HD58647

The infrared excess star HD58647 is at a distance of 277 ± 60pc and has a luminosity of about $250 L_{\odot}$. Mora *et al.* (2001) have determined the spectral type as B9 IV ep by using visible spectral lines. The rotational velocity of the star is $V \sin i = 118 \pm 4$km/s. The spectrum has many non-photospheric features. The infrared color spectrum looks similar to the spectrum of 51 Oph (Malfait *et al.*, 1998). The star has a weak continuum excess compared with other HAeBe stars, but the excess is brighter relative to the star by a factor ~ 3 compared to 51 Oph. The visible line emission study by Manoj *et al.* (2002) revealed that HD58647 has strong Hα line emission but otherwise lacks the lines characteristic for HAeBe stars (the HeI 5875 and 6678Å lines and the OI 7774Å line). They conclude that the star is more likely a classical Be star, as its weak infrared excess is more consistent with free-free emission. Disk sizes measured interferrometrically by Monnier *et al.* (2005) indicate that HD58647 has a small, hot dust disk, similar to 51 Oph. This again indicates that the star is likely a classical Be star, as one would expect the emission region from free-free emission to be small. Circumstellar fundamental CO emission was surveyed by Dent *et al.* (2005) and Brittain *et al.* (2007), who detected only weak CO overtone emission from hot (1000K) gas. Brittain *et al.* (2007) observe a strong K-L excess indicating the presence of an optically thick inner disk. Brittain *et al.* (2007) also observe that the Brγ emission is double peaked, one of three stars with such emission (the others are 51 Oph and HD141569). They mention a possible correlation with double peaked Brγ and fast stellar rotation. Finally, Baines *et al.* (2006) used spectro-astrometry to observe the center of the Hα emission from HD58647. They interpret the astrometric offset in Hα emission as indication that HD58647 has a dim binary companion at a distance of more than 100AU. It is not clear though, if these offsets couldn't be caused by asymmetric

visibility of Hα emission from circumstellar sources.

5.1.3 Research in this Chapter

The goal of this chapter is to investigate the physical characteristics and distribution of circumstellar gas around both of these stars. We acquired high resolution spectra of the CO overtone $v = 2 \rightarrow 0$ bandhead emission. The observations will improve the understanding of the inner disk of these objects, setting boundaries for the relationship between the disk and the star.

The next section will discuss data acquisition and reduction, followed by the discussion of the results. The final section will determine the implications of our results on the understanding of the evolutionary status of these stars.

5.2 Data

Both stars were observed in February 2005 using the IRTF telescope on Mauna Kea (see chapter 3). For the high-resolution observations we used the CSHELL instrument, a cryogenically cooled echelle spectrograph (Greene *et al.*, 1993). The instrument is operated in single order mode and uses a variable filter as order sorter. The detector is a 256×256 pixel detector with 0.2" per pixel. We used the 0.5" slit which gives us a spectral resolution of R = 43000 and nodded in a ABBA pattern. SAO114034 and SAO152839 were observed as calibrator stars for sky subtraction.

The spectra were reduced in a similar way as described in chapter 3. For the flux calibration and the background subtraction we use the medium resolution spectra presented in chapter 3. To avoid contamination of the CO spectrum by the calibrator we used A-type calibrator stars for the medium and the high resolution

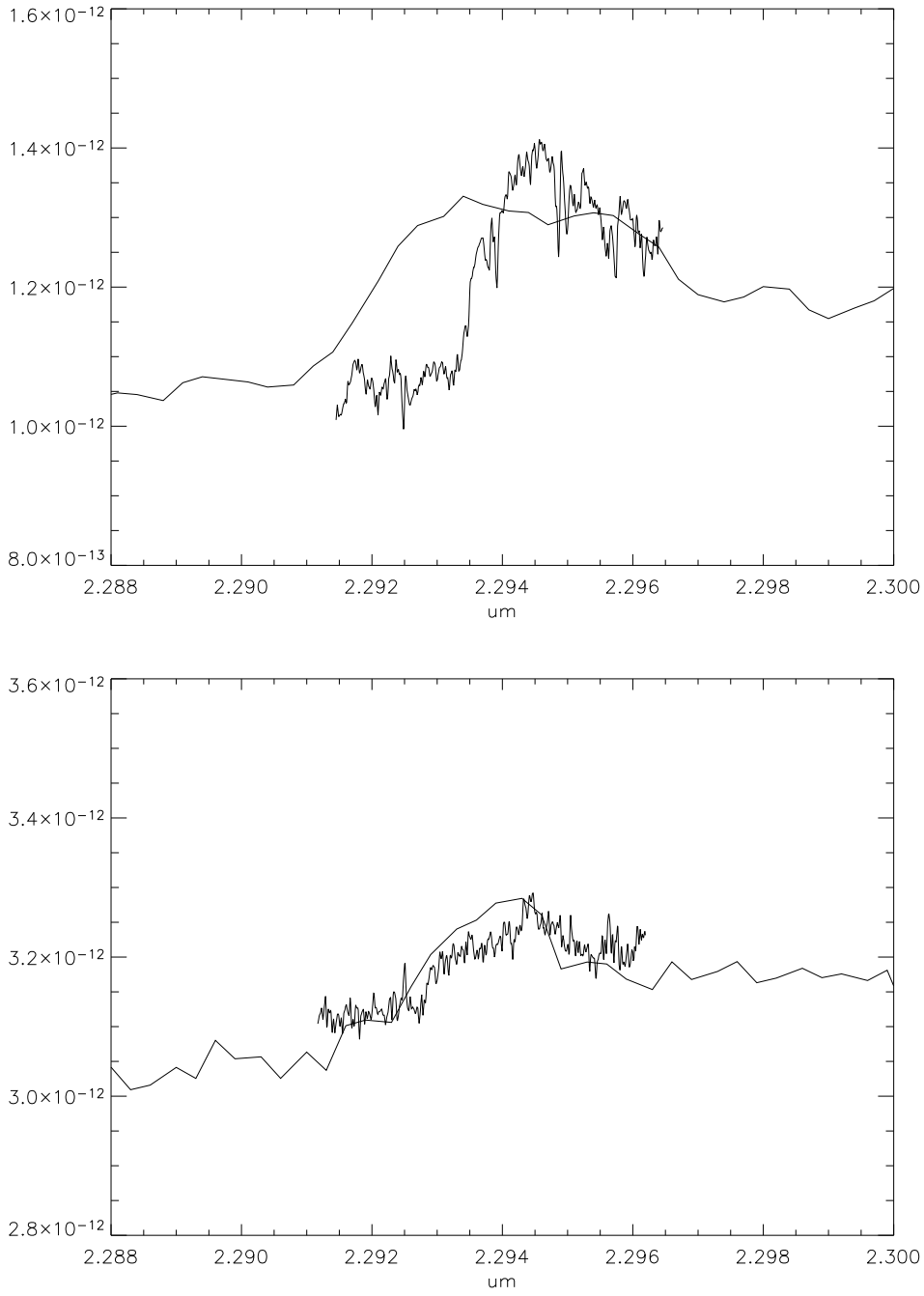

Figure 5.1: Low and high resolution spectra of HD36917 (top) and HD58647 (bottom). The flux units are in $W/m^2/\mu m$.

data.

To reduce the high resolution spectra we did not use the flats, as the pattern of the flats is not seen in our data and the variations in the flat are below the noise level. Hence I don't think the flats were taken under appropriate conditions and the effects cleaned by the flat are to some degree accounted for in the telluric correction. We calibrate the spectra by comparing matching the sky absorption lines to an artificial spectrum produced by ATRAN (Lord, 1992). As the dispersion changes along the slit we use a different calibration for each chop position. The wavelengths are determined by fitting a 2nd order polynomial to the sky absorption lines. The accuracy of the wavelength calibration is approximately $2 \times 10^{-5} \mu$m. The signal to noise is about 100 for the individual spectra. We obtained this value by measuring the standard deviation of the spectra from individual integrations. The reduced spectrum of HD36917 has a very steep slope that we attributed to the slope of the calibrator star. We corrected this by using the calibrator star for HD58647. However the cause of this large slope is unidentified. The spectra were flux calibrated by scaling the spectrum to the medium resolution spectrum. To obtain the spectrum of the CO emission only we subtracted a linear background. This background was obtained as a fit to the medium resolution spectrum shortward of 2.90μm. The reduced data is shown in figure 5.1.

5.3 Results

In our reduced spectra, shown in Figure 5.1, the CO overtone $\Delta v = 2 \rightarrow 0$ bandheads from the low- and high-resolution spectra are clearly visible. The bandhead of HD36917 is very strong relative to the background, about 40% of the background flux, the bandhead of HD58647 is weaker, about 5% of the background flux. The bandheads clearly differ in shape: for HD36917 the flat or convex curve between

the shoulder and the peak indicate a spherical cloud, infalling material or a wind. The convex area shortward of the peak in the HD58647 bandhead indicates a ring or disk geometry for the emitting gas (see chapter 2). Both bandheads are strong relative to the lines at lower J-values indicating the formation in gas with an excitation temperature above 1000K. The high- and low-resolution spectra differ in flux, especially for HD58647. Some of the differences can be explained by the lower quality of the low resolution data. It is also possible that the strength of the bandhead has changed in the observation interval (December 2003 to February 2005), especially for HD58647. The HD58647 spectra agree in wavelength, the small redshift of the high resolution spectrum can be explained by the earths revolution. The larger wavelength shift of the HD36917 spectra is harder to explain. It is possible that the wavelength calibration for the low-resolution data is inadequate. In the spectrum of HD58647 a narrow emission line is visible at 2.295μm (see also Figure 5.3). This water line emission is probably caused by hot vapor in in the atmosphere of the outer disk.

We fitted the models discussed in chapter 2 to the high resolution spectra. For both stars we fitted the optically thin and thick ring model. We also fitted the expanding shells and sphere model to the HD36917 spectra and the optically thin and thick disk model to the HD58647 spectra. From our calibration line measurements we set the Gaussian line width for the instrument profile to 7 km/s. All models (except the disk model) set all the emitting gas at a uniform excitation temperature. The fitted column density is only correct considering that assumption. For optically thin models we fixed the column density at $10^{14}\mathrm{cm}^{-2}$.

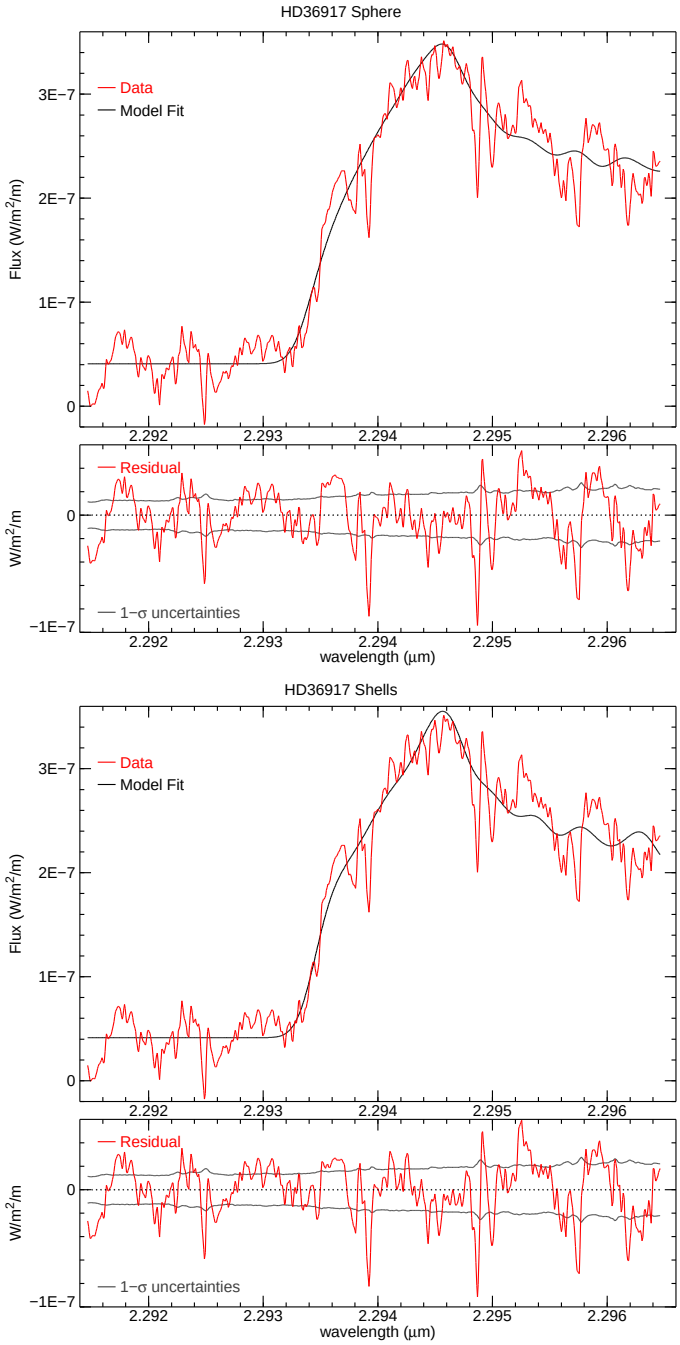

Figure 5.2: Continuum subtracted CSHELL spectra of HD36917 with model fits. The top plot shows the result of the expanding sphere fits, the bottom plots the fit with the expanding shells model. The wavelength is shown in μm and the intensity is in Watts/m^2/m. The residuals between the data and the fits are shown in the bottom plots, along with the statistical error.

5.3.1 HD36917

The model fits are shown in Figures 5.2 and 5.3. Table 5.1 lists the fitted parameters. The spectrum of HD36917 can not be fit by a ring or by a disk spectrum. In these fits the excitation temperature T_0 and emission line width $V_{G,emm}$ diverge towards nonphysical values ($T_0 > 10000$K). The spectrum is better fit by an expanding (or collapsing) sphere or bi-polar shells. The fit for the shells is slightly better. Both fits disagree with the measured spectrum in similar places, as can be seen in the difference plots. Both, the expanding sphere and double shell models fit the bandhead well, the shells model being a better fit to the straight part between the shoulder and the maximum. The amplitude of the residuals are uniform with wavelength indicating a relevant model, even if they don't look like random noise. Systematic errors, probably in the sky subtraction could be responsible for the differences. In both models the emission line width ($V_{G,emm}$) is large and similar to V_p, indicating significant movement of the gas not captured in the model. λ_{off} and $flux_{off}$ are similar for both models. The excitation temperature T_0 is realistic and the fitted values are similar. The cone opening angle θ is large but still indicates directed outflows instead of a spherical one.

5.3.2 HD58647

The fits for HD58647 are good for both ring and disk models. The bandhead shoulder as well as the maximum are well fit, so is the interference pattern longward of the bandhead. As the disk model fit converges towards a very narrow disk (small value of r_o/r_i) we only show the (better) ring fits. However, some parameters, such as the the radial distribution of excitation temperature and column density, have large uncertainties. The optically thin and thick ring models have very similar χ^2 values. Both V_p and T_0 are similar and realistic in both ring fits. The value of

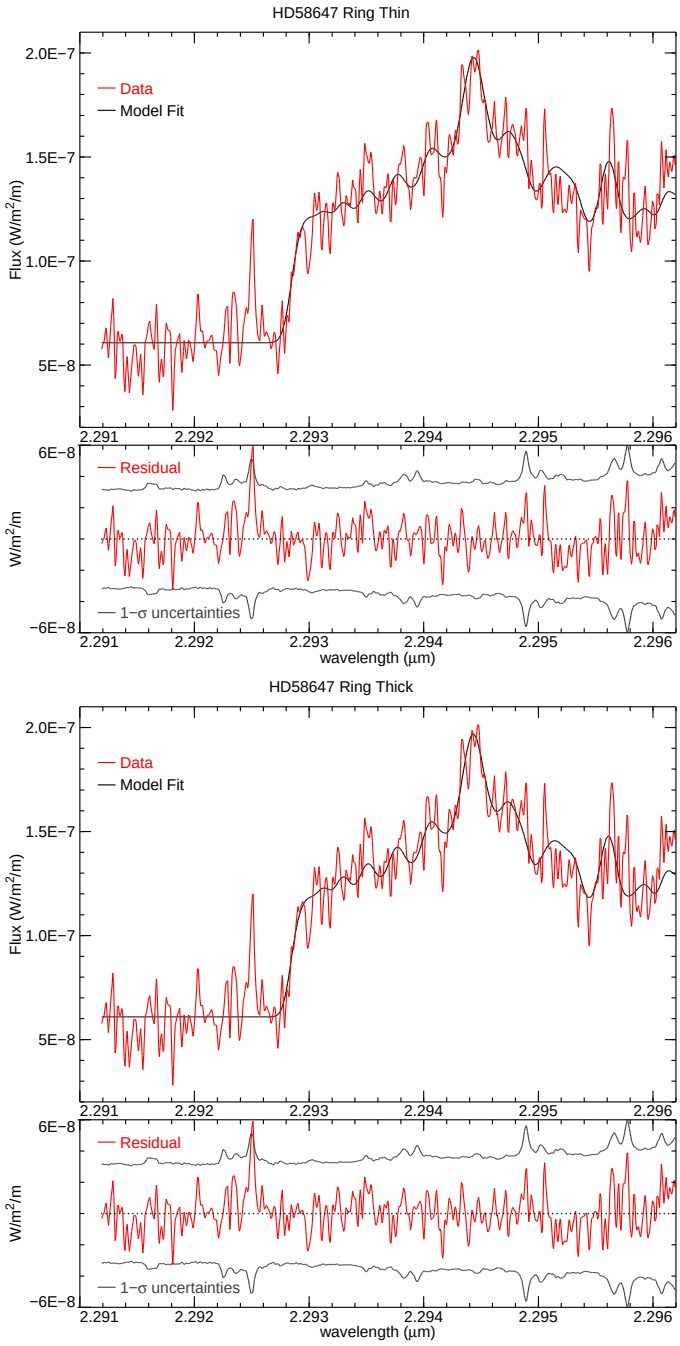

Figure 5.3: Continuum subtracted CSHELL spectra of HD58647 with model fits. The top plot shows the result of the optically thin ring fits, the bottom plots the fit with the optically thick ring model.

Table 5.1: Fitting results for different models. Given are the 1-σ uncertainties. Positive values of V_{off} represent a redshift

		HD36917	
		expanding sphere	conic shells
V_p	(km/s)	86.3±1.1	78.4±2.1
T_0	(K)	1740±30	1770±40
$V_{G,emm}$	(km/s)	21.2±2.7	22.3±2.6
Ω	($\times 10^{-16}$ sterrad)	$39 \pm 4 \times 10^4$	$35 \pm 4 \times 10^4$
N_{col}	($\times 10^{20} \frac{1}{cm^2}$)	10^{-6} (set)	10^{-6} (set)
M_{CO}	($\times 10^{-6} M_{Earth}$)	9.6	8.6
V_{off}	(km/s)	61.3±0.9	63.1±0.9
$flux_{off}$	$\times 10^{-14} \frac{W}{m^2 \mu m}$)	4.08±0.11	4.13±0.11
i	(°)		36.6±7
θ	(°)		72.0±9
χ^2		1.86366	1.81154

		HD58647	
		opt thin ring	opt thick ring
V_p	(km/s)	105.3±0.5	105.3±0.5
T_0	(K)	2180±60	2380±120
$V_{G,emm}$	(km/s)	9.1±1.0	7.7±1.0
Ω	($\times 10^{-16}$ sterrad)	$9.88 \pm 0.11 \times 10^4$	$5.0 \pm 1.5 \times 10^{-2}$
N_{col}	($\times 10^{20} \frac{1}{cm^2}$)	10^{-6} (set)	1.6±0.4
M_{CO}	($\times 10^{-6} M_{Earth}$)	9.1	7.3
V_{off}	(km/s)	17.0±0.5	17.1±0.5
$flux_{off}$	$\times 10^{-14} \frac{W}{m^2 \mu m}$)	6.07±0.06	6.08±0.06
χ^2		0.09492	0.09428

$V_{G,emm}$ is somewhat large for the optically thin disk. The flux and wavelength offsets are consistent between the ring models. The χ^2 values are quite small, which could indicate that we overestimated the uncertainties.

5.4 Discussion

5.4.1 HD36917

The high resolution CO overtone spectrum of HD36917 is most likely generated by gas flowing away from the star. The small amount of CO gas emitting the

radiation has an excitation temperature of about 1700K and an outflow velocity of about 80km/s. The emission line profiles for both, the sphere and shells solutions, are shown in Figure 5.4. The sphere profile is the convolution of the rectangle function from the shell with the emission line profile. The shells profile has two main maxima, similar but smaller than the ring or disk profile (see Chapter 2) and provides a closer fit to the data. It could also be caused by a disk or ring geometry not considered by our model: for example a disk with very high optical depth or a disk that's viewed nearly edge on such that $Z/R \sim \cos i$. Another possibility is the presence of a flared outer disk which would hide the ansae of the CO overtone emitting inner disk. One would not expect this last option, as the star has an infrared spectrum similar to the Group II objects (non flared disk) as defined by Meeus *et al.* (2001).

The excitation temperature of the emitting gas is in the lower part of the possible temperature range for it to emit CO overtone emission. It is possible that the observed molecules are formed in the colder regions of a wind which would explain the lower temperatures. If the system would be accreting or had a significant disk, we would expect to see warmer CO gas. This observation is consistent with other signs that HD36917 is not accreting and may not be a HAeBe star anymore (Manoj *et al.*, 2002). If the observed gas is indeed from a wind we can get a rough estimate of the mass loss rate: Assuming that the emission happens over a range of 0.2AU from the star, the gas (speeding out at 80km/s) spends about 1.8×10^6 seconds in this regions. This distance is probably an estimate on the long side, the real distance could be shorter. Having $8.6 \times 10^{-6} M_{Earth}$ of CO (or $5.9 \times 10^{-4} M_{Earth}$ of H) in this region implies that the star looses mass at a rate of $3 \times 10^{-8} M_{\odot}$/yr. This seems rather high for a young, but non-accreting A0V star. Another possibility is that the emission we observed originates in an

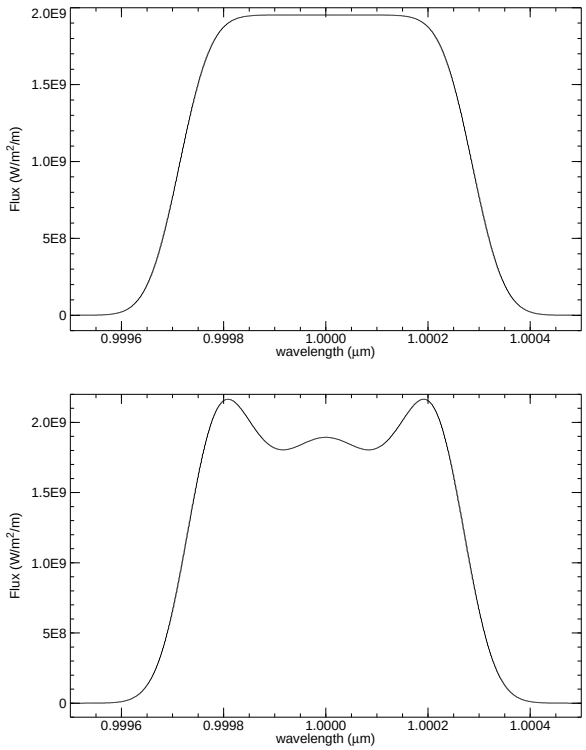

Figure 5.4: Emission line profiles for of a single line of the sphere (left) and shell (right) fit for the HD36917 spectrum. The spectrum is shown for a line at 1μm, the flux is in arbitrary units.

accretion flow. This hypothesis contradicts earlier observations by (Manoj *et al.*, 2002) and is inconsistent with the low excitation temperature we measure.

5.4.2 HD58647

The gas around HD58647 is definitely in a ring or a narrow disk. The emission line width is too wide to be pure thermal emission, which would be 1000m/s for CO at these temperatures. Turbulence in the gas and/or the effect of emission line broadening by looking through different disk layers (see Section 2.4) must contribute to the emission line width. The disk inclination is probably close to edge-on, as we measure a significant V_p. The excitation temperature in the gas corresponds to a blackbody temperature at 0.4AU from the star. Assuming an

inclination of 90° this implies a stellar mass of $5M_{\odot}$. As this is a lower limit the mass would be higher if the inclination were smaller. We expect a B9 star to be lighter than that value so the gas must be closer in than the 0.4AU mentioned above or the stellar type is inaccurate. This implies that the gas is neither optically thick nor in radiative equilibrium.

Comparing the CO overtone emission of HD58647 to the emission from 51 Oph shows that both have hot gas, but that there is less CO overtone emission from HD58647 but its IR excess is stronger. Possibly the two stars are at a different stage in their evolution or the geometry allows us to see more CO overtone emitting region from 51 Oph. We don't see any overtone emission from a colder companion suggested by Baines *et al.* (2006). The CO overtone spectrum is consistent with a single ring source.

5.5 Conclusions

HD36917 is the one of the few HAeBe stars with CO overtone emission in our survey. The discovery that emission is probably caused by material in a wind is supported by our modeling as the findings by other authors that the star is unlikely to have a dense gas disk. We estimate the upper limit for the mass loss rate at $3 \times 10^{-8} M_{\odot}/\mathrm{yr}$. This is rather high for an older HAeBe star especially if we consider that in Chapter 3 we measured circumstellar Brγ absorption, hence no accretion luminosity. Nevertheless, we cannot exclude the possibility that the spectrum is caused by gas in a disk viewed close to edge-on.

The CO overtone emission from HD58647 is very likely produced by gas in a narrow ring orbiting the star. The emission width is quite wide, indicating strong turbulence or a thick emission region. It is possible that this star is a classical Be star similar to 51 Oph but at a different evolutionary stage.

Combining the present observations with future high resolution spectra of other bandheads and hydrogen emission lines, as well as interferometric measurements to investigate the location of the emission region of the CO bandheads, will improve our picture of these stars.

BIBLIOGRAPHY

Acke, B., & van den Ancker, M. E. 2004. ISO spectroscopy of disks around Herbig Ae/Be stars. A&A, **426**(Oct.), 151–170.

Acke, B., van den Ancker, M. E., & Dullemond, C. P. 2005. [O I] 6300 Å emission in Herbig Ae/Be systems: Signature of Keplerian rotation. A&A, **436**(June), 209–230.

Baines, D., Oudmaijer, R. D., Porter, J. M., & Pozzo, M. 2006. On the binarity of Herbig Ae/Be stars. MNRAS, **367**(Apr.), 737–753.

Blake, G. A., & Boogert, A. C. A. 2004. High-Resolution 4.7 Micron Keck/NIRSPEC Spectroscopy of the CO Emission from the Disks Surrounding Herbig Ae Stars. ApJ, **606**(May), L73–L76.

Brittain, S. D., & Rettig, T. W. 2002. CO and H_3^+ in the protoplanetary disk around the star HD141569. Nature, **418**(July), 57–59.

Brittain, S. D., Rettig, T. W., Simon, T., Kulesa, C., DiSanti, M. A., & Dello Russo, N. 2003. CO Emission from Disks around AB Aurigae and HD 141569: Implications for Disk Structure and Planet Formation Timescales. ApJ, **588**(May), 535–544.

Brittain, S. D., Simon, T., Najita, J. R., & Rettig, T. W. 2007. Warm Gas in the Inner Disks around Young Intermediate-Mass Stars. ApJ, **659**(Apr.), 685–704.

Calvet, N., Muzerolle, J., Briceño, C., Hernández, J., Hartmann, L., Saucedo, J. L., & Gordon, K. D. 2004. The Mass Accretion Rates of Intermediate-Mass T Tauri Stars. AJ, **128**(Sept.), 1294–1318.

Cardelli, J. A., Clayton, G. C., & Mathis, J. S. 1989. The relationship between infrared, optical, and ultraviolet extinction. ApJ, **345**(Oct.), 245–256.

Carr, J. S., Tokunaga, A. T., Najita, J., Shu, F. H., & Glassgold, A. E. 1993. The inner-disk and stellar properties of the young stellar object WL 16. ApJ, **411**(July), L37–L40.

Carr, J. S., Tokunaga, A. T., & Najita, J. 2004. Hot H_2O Emission and Evidence for Turbulence in the Disk of a Young Star. ApJ, **603**(Mar.), 213–220.

Chandler, C. J., Carlstrom, J. E., & Scoville, N. Z. 1995. Infrared CO Emission from Young Stars: Accretion Disks and Neutral Winds. ApJ, **446**(June), 793–+.

Chandra, S., Maheshwari, V. U., & Sharma, A. K. 1996. Einstein A-coefficients for vib-rotational transitions in CO. A&AS, **117**(June), 557–559.

Cox, A. N. 2000. *Allen's astrophysical quantities*. Allen's astrophysical quantities, 4th ed. Publisher: New York: AIP Press; Springer, 2000. Editedy by Arthur N. Cox. ISBN: 0387987460.

Cushing, M. C., Vacca, W. D., & Rayner, J. T. 2004. Spextool: A Spectral Extraction Package for SpeX, a 0.8-5.5 Micron Cross-Dispersed Spectrograph. PASP, **116**(Apr.), 362–376.

Dent, W. R. F., Greaves, J. S., & Coulson, I. M. 2005. CO emission from discs around isolated HAeBe and Vega-excess stars. MNRAS, **359**(May), 663–676.

Dullemond, C. P., & Dominik, C. 2004. Flaring vs. self-shadowed disks: The SEDs of Herbig Ae/Be stars. A&A, **417**(Apr.), 159–168.

Dunham, J. L. 1932. The Energy Levels of a Rotating Vibrator. *Phys. Rev.*, **41**(Sept.), 721–731.

Dunkin, S. K., Barlow, M. J., & Ryan, S. G. 1997. High-resolution spectroscopy of Vega-like stars - II. Age indicators, activity and circumstellar gas. MNRAS, **290**(Sept.), 165–185.

Eisner, J. A., Lane, B. F., Hillenbrand, L. A., Akeson, R. L., & Sargent, A. I. 2004. Resolved Inner Disks around Herbig Ae/Be Stars. ApJ, **613**(Oct.), 1049–1071.

Evans, D. S. 1967. The Revision of the General Catalogue of Radial Velocities. *Pages 57–+ of:* Batten, A. H., & Heard, J. F. (eds), *Determination of Radial Velocities and their Applications*. IAU Symposium, vol. 30.

Farrenq, R., Guelachvili, G., Sauval, A. J., Grevesse, N., & Farmer, C. B. 1991. Improved Dunham coefficients for CO from infrared solar lines of high rotational excitation. *J. Mol. Spectrosc.*, **149**(Oct.), 375–390.

Garcia Lopez, R., Natta, A., Testi, L., & Habart, E. 2006. Accretion rates in Herbig Ae stars. A&A, **459**(Dec.), 837–842.

Grady, C. A., Woodgate, B. E., Bowers, C. W., Gull, T. R., Sitko, M. L., Carpenter, W. J., Lynch, D. K., Russell, R. W., Perry, R. B., Williger, G. M., Roberge, A., Bouret, J.-C., & Sahu, M. 2005. Coronagraphic Imaging of Pre-Main-Sequence Stars with the Hubble Space Telescope Space Telescope Imaging Spectrograph. I. The Herbig Ae Stars. ApJ, **630**(Sept.), 958–975.

Grady, C. A., Schneider, G., Hamaguchi, K., Sitko, M. L., Carpenter, W. J., Hines, D., Collins, K. A., Williger, G. M., Woodgate, B. E., Henning, T., Ménard, F., Wilner, D., Petre, R., Palunas, P., Quirrenbach, A., Nuth, III, J. A., Silverstone, M. D., & Kim, J. S. 2007. The Disk and Environment of a Young Vega Analog: HD 169142. ApJ, **665**(Aug.), 1391–1406.

Gray, R. O., & Corbally, C. J. 1998. The Incidence of lambda Boötis Stars via an Extension of the MK Spectral Classification System to Very Young A-Type Stars. AJ, **116**(Nov.), 2530–2535.

Greene, T. P., Tokunaga, A. T., Toomey, D. W., & Carr, J. B. 1993 (Oct.). CSHELL: a high spectral resolution 1-5 um cryogenic echelle spectrograph for the IRTF. *Pages 313–324 of:* Fowler, A. M. (ed), *Proc. SPIE Vol. 1946, p. 313-324, Infrared Detectors and Instrumentation, Albert M. Fowler; Ed.* Presented at the Society of Photo-Optical Instrumentation Engineers (SPIE) Conference, vol. 1946.

Hartmann, L. 2001. *Accretion Processes in Star Formation.* Accretion Processes in Star Formation, by Lee Hartmann, pp. 237. ISBN 0521785200. Cambridge, UK: Cambridge University Press, January 2001.

Hartmann, L., Hinkle, K., & Calvet, N. 2004. High-Resolution Near-Infrared Spectroscopy of FU Orionis Objects. ApJ, **609**(July), 906–916.

Hayward, T. L., Brandl, B., Pirger, B., Blacken, C., Gull, G. E., Schoenwald, J., & Houck, J. R. 2001. PHARO: A Near-Infrared Camera for the Palomar Adaptive Optics System. PASP, **113**(Jan.), 105–118.

Hempel, M., & Schmitt, J. H. M. M. 2003. High resolution spectroscopy of circumstellar material around A stars. A&A, **408**(Sept.), 971–979.

Herbig, G. H. 1960. The Spectra of Be- and Ae-TYPE Stars Associated with Nebulosity. ApJS, **4**(Mar.), 337–+.

Hernández, J., Calvet, N., Briceño, C., Hartmann, L., & Berlind, P. 2004. Spectral Analysis and Classification of Herbig Ae/Be Stars. AJ, **127**(Mar.), 1682–1701.

Herter, T., Lacasse, M. G., Wesemael, F., & Winget, D. E. 1979. Theoretical photometric and spectroscopic properties of stellar accretion disks with application to cataclysmic variables. ApJS, **39**(Apr.), 513–535.

Horne, K. 1986. An optimal extraction algorithm for CCD spectroscopy. PASP, **98**(June), 609–617.

Imhoff, C. L. 1994. MG II and clues to the evolutionary status of the Herbig Ae/Be stars. *Pages 107–+ of:* The, P. S., Perez, M. R., & van den Heuvel, E. P. J. (eds), *The Nature and Evolutionary Status of Herbig Ae/Be Stars*. Astronomical Society of the Pacific Conference Series, vol. 62.

Johns-Krull, C. M., Valenti, J. A., & Linsky, J. L. 2000. An IUE Atlas of Pre-Main-Sequence Stars. II. Far-Ultraviolet Accretion Diagnostics in T Tauri Stars. ApJ, **539**(Aug.), 815–833.

Keller, L. D., Sloan, G. C., Forest, W. J., DÁlesio, P., Ayala, S., Shah, S., Calvet, N., Hartmann, L., Najita, J., Sargent, B., Li, A., Watson, D. M., & Chen, C. H. 2007 (Oct.). *PAH emission from Herbig Ae/Be stars*. To be published in ApJ.

Kraus, M., Krügel, E., Thum, C., & Geballe, T. R. 2000. CO band emission from MWC 349. I. First overtone bands from a disk or from a wind? A&A, **362**(Oct.), 158–168.

Kurucz, R. L. 1992. Model Atmospheres for Population Synthesis. *Pages 225–+ of:* Barbuy, B., & Renzini, A. (eds), *IAU Symp. 149: The Stellar Populations of Galaxies*.

Lamers, H. J. G. L. M. 2006 (Dec.). Stars with the B[e] Phenomenon: Summary and Personal Conclusions. *Pages 371–+ of:* Kraus, M., & Miroshnichenko, A. S.

(eds), *Stars with the B[e] Phenomenon*. Astronomical Society of the Pacific Conference Series, vol. 355.

Leinert, C., van Boekel, R., Waters, L. B. F. M., Chesneau, O., Malbet, F., Köhler, R., Jaffe, W., Ratzka, T., Dutrey, A., Preibisch, T., Graser, U., Bakker, E., Chagnon, G., Cotton, W. D., Dominik, C., Dullemond, C. P., Glazenborg-Kluttig, A. W., Glindemann, A., Henning, T., Hofmann, K.-H., de Jong, J., Lenzen, R., Ligori, S., Lopez, B., Meisner, J., Morel, S., Paresce, F., Pel, J.-W., Percheron, I., Perrin, G., Przygodda, F., Richichi, A., Schöller, M., Schuller, P., Stecklum, B., van den Ancker, M. E., von der Lühe, O., & Weigelt, G. 2004. Mid-infrared sizes of circumstellar disks around Herbig Ae/Be stars measured with MIDI on the VLTI. A&A, **423**(Aug.), 537–548.

Lord, S. D. 1992 (December). *"A new software tool for computing Earth's atmospheric transmission of near- and far-infrared radiation"*. Tech. rept. NASA-TM-103957.

Malfait, K., Bogaert, E., & Waelkens, C. 1998. An ultraviolet, optical and infrared study of Herbig Ae/Be stars. A&A, **331**(Mar.), 211–223.

Manoj, P., Maheswar, G., & Bhatt, H. C. 2002. Non-emission-line young stars of intermediate mass. MNRAS, **334**(Aug.), 419–425.

Matsuo, T., Shibai, H., Ootsubo, T., & Tamura, M. 2007. Planetary Formation Scenarios Revisited: Core-Accretion versus Disk Instability. ApJ, **662**(June), 1282–1292.

McLean, I. S., Becklin, E. E., Bendiksen, O., Brims, G., Canfield, J., Figer, D. F., Graham, J. R., Hare, J., Lacayanga, F., Larkin, J. E., Larson, S. B., Levenson, N., Magnone, N., Teplitz, H., & Wong, W. 1998 (Aug.). Design and

development of NIRSPEC: a near-infrared echelle spectrograph for the Keck II telescope. *Pages 566–578 of:* Fowler, A. M. (ed), *Proc. SPIE Vol. 3354, p. 566-578, Infrared Astronomical Instrumentation, Albert M. Fowler; Ed.* Presented at the Society of Photo-Optical Instrumentation Engineers (SPIE) Conference, vol. 3354.

McLean, I. S., McGovern, M. R., Burgasser, A. J., Kirkpatrick, J. D., Prato, L., & Kim, S. S. 2003. The NIRSPEC Brown Dwarf Spectroscopic Survey. I. Low-Resolution Near-Infrared Spectra. ApJ, **596**(Oct.), 561–586.

Meeus, G., Waters, L. B. F. M., Bouwman, J., van den Ancker, M. E., Waelkens, C., & Malfait, K. 2001. ISO spectroscopy of circumstellar dust in 14 Herbig Ae/Be systems: Towards an understanding of dust processing. A&A, **365**(Jan.), 476–490.

Monnier, J. D., Millan-Gabet, R., Billmeier, R., Akeson, R. L., Wallace, D., Berger, J.-P., Calvet, N., D'Alessio, P., Danchi, W. C., Hartmann, L., Hillenbrand, L. A., Kuchner, M., Rajagopal, J., Traub, W. A., Tuthill, P. G., Boden, A., Booth, A., Colavita, M., Gathright, J., Hrynevych, M., Le Mignant, D., Ligon, R., Neyman, C., Swain, M., Thompson, R., Vasisht, G., Wizinowich, P., Beichman, C., Beletic, J., Creech-Eakman, M., Koresko, C., Sargent, A., Shao, M., & van Belle, G. 2005. The Near-Infrared Size-Luminosity Relations for Herbig Ae/Be Disks. ApJ, **624**(May), 832–840.

Mora, A., Merín, B., Solano, E., Montesinos, B., de Winter, D., Eiroa, C., Ferlet, R., Grady, C. A., Davies, J. K., Miranda, L. F., Oudmaijer, R. D., Palacios, J., Quirrenbach, A., Harris, A. W., Rauer, H., Cameron, A., Deeg, H. J., Garzón, F., Penny, A., Schneider, J., Tsapras, Y., & Wesselius, P. R. 2001. EXPORT:

Spectral classification and projected rotational velocities of Vega-type and pre-main sequence stars. A&A, **378**(Oct.), 116–131.

Muzerolle, J., Hartmann, L., & Calvet, N. 1998. A Brgamma Probe of Disk Accretion in T Tauri Stars and Embedded Young Stellar Objects. AJ, **116**(Dec.), 2965–2974.

Najita, J., Carr, J. S., & Tokunaga, A. T. 1996a. High-Resolution Spectroscopy of BR gamma Emission in Young Stellar Objects. ApJ, **456**(Jan.), 292–+.

Najita, J., Carr, J. S., Glassgold, A. E., Shu, F. H., & Tokunaga, A. T. 1996b. Kinematic Diagnostics of Disks around Young Stars: CO Overtone Emission from WL 16 and 1548C27. ApJ, **462**(May), 919–+.

Najita, J., Carr, J. S., & Mathieu, R. D. 2003. Gas in the Terrestrial Planet Region of Disks: CO Fundamental Emission from T Tauri Stars. ApJ, **589**(June), 931–952.

Najita, J. R., Edwards, S., Basri, G., & Carr, J. 2000. Spectroscopy of Inner Protoplanetary Disks and the Star-Disk Interface. *Protostars and Planets IV*, May, 457–+.

Najita, J. R., Carr, J. S., Glassgold, A. E., & Valenti, J. A. 2007. Gaseous Inner Disks. *Pages 507–522 of:* Reipurth, B., Jewitt, D., & Keil, K. (eds), *Protostars and Planets V*.

Olofsson, H. 1999. The AGB-star Phenomenon: Setting the Stage. *Pages 3–+ of:* Le Bertre, T., Lebre, A., & Waelkens, C. (eds), *Asymptotic Giant Branch Stars*. IAU Symposium, vol. 191.

Piétu, V., Dutrey, A., & Kahane, C. 2003. A Keplerian disk around the Herbig Ae star HD 34282. A&A, **398**(Feb.), 565–569.

Porter, J. M., & Rivinius, T. 2003. Classical Be Stars. PASP, **115**(Oct.), 1153–1170.

Rayner, J. T., Toomey, D. W., Onaka, P. M., Denault, A. J., Stahlberger, W. E., Vacca, W. D., Cushing, M. C., & Wang, S. 2003. SpeX: A Medium-Resolution 0.8-5.5 Micron Spectrograph and Imager for the NASA Infrared Telescope Facility. PASP, **115**(Mar.), 362–382.

Roberge, A., Feldman, P. D., Lecavelier des Etangs, A., Vidal-Madjar, A., Deleuil, M., Bouret, J.-C., Ferlet, R., & Moos, H. W. 2002. Far Ultraviolet Spectroscopic Explorer Observations of Possible Infalling Planetesimals in the 51 Ophiuchi Circumstellar Disk. ApJ, **568**(Mar.), 343–351.

Rodgers, B. M. 2001. *What's happening around Herbig Ae stars? Investigating circumstellar activity in young intermediate mass stars with optical and near infrared spectroscopy.* Ph.D. thesis, AA(UNIVERSITY OF WASHINGTON).

Scoville, N. Z., Krotkov, R., & Wang, D. 1980. Collisional and infrared radiative pumping of molecular vibrational states - The carbon monoxide infrared bands. ApJ, **240**(Sept.), 929–939.

Shu, F. H., Shang, H., Glassgold, A. E., & Lee, T. 1997. X-rays and fluctuating X-winds from protostars. *Science*, **277**, 1475–1479.

Skrutskie, M. F., Cutri, R. M., Stiening, R., Weinberg, M. D., Schneider, S., Carpenter, J. M., Beichman, C., Capps, R., Chester, T., Elias, J., Huchra, J., Liebert, J., Lonsdale, C., Monet, D. G., Price, S., Seitzer, P., Jarrett, T., Kirkpatrick, J. D., Gizis, J. E., Howard, E., Evans, T., Fowler, J., Fullmer, L., Hurt, R., Light, R., Kopan, E. L., Marsh, K. A., McCallon, H. L., Tam, R., Van

Dyk, S., & Wheelock, S. 2006. The Two Micron All Sky Survey (2MASS). AJ, **131**(Feb.), 1163–1183.

Thi, W.-F., van Dalen, B., Bik, A., & Waters, L. B. F. M. 2005. Evidence for a hot dust-free inner disk around 51 Oph. A&A, **430**(Jan.), L61–L64.

Vacca, W. D., Cushing, M. C., & Rayner, J. T. 2003. A Method of Correcting Near-Infrared Spectra for Telluric Absorption. PASP, **115**(Mar.), 389–409.

Valenti, J. A., Johns-Krull, C. M., & Linsky, J. L. 2000. An IUE Atlas of Pre-Main-Sequence Stars. I. Co-added Final Archive Spectra from the SWP Camera. ApJS, **129**(July), 399–420.

Valenti, J. A., Fallon, A. A., & Johns-Krull, C. M. 2003. An IUE Atlas of Pre-Main-Sequence Stars. III. Co-added Final Archive Spectra from the Long-Wavelength Cameras. ApJS, **147**(Aug.), 305–336.

van den Ancker, M. E., de Winter, D., & Tjin A Djie, H. R. E. 1998. HIPPARCOS photometry of Herbig Ae/Be stars. A&A, **330**(Feb.), 145–154.

van den Ancker, M. E., Meeus, G., Cami, J., Waters, L. B. F. M., & Waelkens, C. 2001. The composition of circumstellar gas and dust in 51 Oph. A&A, **369**(Apr.), L17–L21.

Vieira, S. L. A., Corradi, W. J. B., Alencar, S. H. P., Mendes, L. T. S., Torres, C. A. O., Quast, G. R., Guimarães, M. M., & da Silva, L. 2003. Investigation of 131 Herbig Ae/Be Candidate Stars. AJ, **126**(Dec.), 2971–2987.

Vinković, D., & Jurkić, T. 2007. Relation between the Luminosity of Young Stellar Objects and Their Circumstellar Environment. ApJ, **658**(Mar.), 462–479.

Wade, G. A., Bagnulo, S., Drouin, D., Landstreet, J. D., & Monin, D. 2007. A search for strong, ordered magnetic fields in Herbig Ae/Be stars. MNRAS, **376**(Apr.), 1145–1161.

Waelkens, C., Waters, L. B. F. M., de Graauw, M. S., Huygen, E., Malfait, K., Plets, H., Vandenbussche, B., Beintema, D. A., Boxhoorn, D. R., Habing, H. J., Heras, A. M., Kester, D. J. M., Lahuis, F., Morris, P. W., Roelfsema, P. R., Salama, A., Siebenmorgen, R., Trams, N. R., van der Bliek, N. R., Valentijn, E. A., & Wesselius, P. R. 1996. SWS observations of young main-sequence stars with dusty circumstellar disks. A&A, **315**(Nov.), L245–L248.

Wallace, L., & Hinkle, K. 1997. Medium-Resolution Spectra of Normal Stars in the K Band. ApJS, **111**(Aug.), 445–+.

Waters, L. B. F. M., & Waelkens, C. 1998. Herbig Ae/Be Stars. ARA&A, **36**, 233–266.

Waters, L. B. F. M., Cote, J., & Geballe, T. R. 1988. 51 Ophiuchi (B9.5 Ve) - A Be star in the class of Beta Pictoris stars? A&A, **203**(Sept.), 348–354.

Wolff, S. C., Strom, S. E., & Hillenbrand, L. A. 2004. The Angular Momentum Evolution of 0.1-10 M_{solar} Stars from the Birth Line to the Main Sequence. ApJ, **601**(Feb.), 979–999.